SBIR PHASE I PROJECT FINAL REPORT

Month/Year: December 1991

Title: Real-Time NDE Using Multi-Function
                       Robotic Sonoscope (MFRS)

Name & Address   Sonoscan, Inc.
of Contractor: 530 E. Green Street
                       Bensenville, IL 60106
                       Tele: (708) 766-7088

Contract No: N60921-91-C-0131

Dollar Amount: $48,895.00

                       (Competitively Awarded)

Sponsor: Al Bertram, Code R32
                       White Oak Laboratory
                       Naval Surface Warfare Center
                       10901 New Hampshire Avenue
                       Silver Spring, MD 20903-5000
                       Telephone No. (301) 394-2019

19980309 227

U 3689

Table of Contents

Accession Number: 3689

Publication Date: Dec 01, 1991

Title: SBIR Phase I Project Final Report: Real-Time NDE Multi-Function Robotic Sonoscope (MFRS)

Corporate Author Or Publisher: Sonoscan, Inc. 530 E. Green Street, Bensenville, IL 60106

Report Prepared for: White Oak Laboratory, Naval Surface Warfare Center, 10901 New Hampshire Avenue, Silver Spring, MD 20903-5000

Descriptors, Keywords: SBIR Phase I Real-Time NDE MFRS Metal Matrix Composite NDI Robotic Arm Laser C-Mode

Pages: 00096

Cataloged Date: Aug 14, 1992

Contract Number: N60921-91-C-0131

Document Type: HC

Number of Copies In Library: 000001

Record ID: 24539

1. DEGREE TO WHICH PHASE I OBJECTIVES HAVE BEEN MET

1.1 The Proposed Works in Phase I

Project Management

During the Phase I, project management has been set to establish a sound basis for scheduling, controlling and modifying the project. In this section we present a simplified Project WBS (Work Breakdown Structure) and a Gantt chart, showing the proposed and then completed activities and tasks in the Phase I. The project has been broken down to eight main activities, according to the Technical Objectives presented in the Phase I proposal.

The activities include:

> Samples Preparation
> Optical Module Design
> Spectral Analyzer Design
> Acoustic Microscopy Design
> Computer Programs Development
> Coordination of Function
> Robot, and
> Reports

A number of tasks are assigned for each activity (please see the attached Gantt Chart).

Reproduction of Phase I Work Statement

The Technical Approach, Technical Objectives, Statement of Work and the Performance Schedule described in the Phase I proposal are reproduced here as a guideline of the project.

Technical Approach (adapted from Phase I Proposal)

1. Optical Inspection -- Determine the critical size of surface flaws or anomalies and design sets of optics capable of detecting the smallest critical size, and meanwhile minimizing the background noise level. The defect recognition software will be evaluated.

2. Spectral Analysis -- Establish a library consisting of acoustic spectra for materials containing a variety of flaws and compare the spectra to that of an ideal material. Verify the probability of telling a defective material by the spectral analysis.

3. Acoustic Microscopy -- Although the detection of flaws by acoustic microscope has become routine, interpretation of the results is not straight. In the Phase I, we will establish a library consisting of acoustic micrographs for materials containing various flaws and correlate them with the results of conventional mechanical tests. A specific computer programs for automatic defect recognition will be developed. Optimal operating frequencies for various representative materials will be studied.

4. Coordination of Functions -- Coordination between Optical Inspection, Spectral Analysis, and Acoustic Microscopy functions is important. To make the system compact and reduce the cost, some elements are shared by different functions. Specific designs in both hardware and software are needed and will be investigated in the Phase I.

5. Robot -- Commercial robots may be available and the availability will be investigated in the Phase I. The modification may be studied, however, it would not be of major concern in the Phase I.

6. Computer Programs -- Specific computer programs are required for system controls (e.g. motion control, electronics control etc.), data acquisition and processing, and defect recognition. Among them only the data recognition algorithm will be developed in the Phase I. (The rest of the software will be done in Phase II project.)

7. Correlation of the NDE results -- The results from the above mentioned functions (Optical inspection, Spectral Analysis and Acoustic Microscopy) will be correlated by performing the conventional mechanical tests on the selected samples by our consultant, Professor Henrique Reis at University of Illinois-Urbana. The material defects will be identified and related to failure modes.

8. Material Samples Procurement -- Material samples from a representative defense manufacturing process will be procured from our consultant and our contracts in the related industry.

Phase I Technical Objectives (adapted from Phase I Proposal)

The objective of this Phase I project is to determine the feasibility of the proposed MFRS system and the associated evaluation techniques, namely optical inspection, spectral analysis and acoustic microscopy. We also want to correlate the results of these techniques to the results of conventional approaches in order to determine the feasibility.

A series of specific technical objectives will be carried out in order to achieve the overall objective of Phase I. These objectives are:

1. Optical Inspection -- Determine the critical size of surface flaws in structural materials and design a scanning laser and optics module capable of detecting the smallest critical size.

2. Spectral Analysis -- Verify the probability of detecting defects in materials, produced by a representative defense manufacturing process, using spectral analysis and establish a data base.

3. Acoustic Microscopy -- Optimize ultrasonic frequency for the selected structural materials, establish a library consisting of acoustic micrographs for defects-containing material samples and relate the results to the failure modes in conventional mechanical tests.

4. Coordination of Functions -- Clearly define hardware and software requirements for each individual function and identify elements which would be shared. Evaluate time-division circuitry and control program. Investigate coordination between functions.

5. Computer Programs -- Design computer algorithms of automatic defect recognition for the data obtained from optical inspection, spectral analysis and acoustic microscopy, respectively.

6. Robot -- Study the availability of commercial robots and the necessary modifications to implement the proposed functions in it.

7. Report and Phase II Proposal -- To report the results of the above mentioned works, and develop a Phase II project to design and implement the proposed MFRS system.

Phase I Statement Of Work (adapted from Phase I Proposal)

Sonoscan, Inc., will provide the personnel and facilities necessary to investigate and develop a practical Multi-Function Robotic Sonoscope capable of automatic on-line inspection during manufacturing process of materials.

Scope of Work

This project consists of the following tasks:

1. Determine the critical size of surface flaws and design scanning laser module capable of detecting the smallest critical size.

2. Optimize ultrasonic frequency, establish a data base consisting of spectral analysis results for materials containing a variety of defects, compared to that of an ideal material.

3. Optimize ultrasonic frequency for selected materials, obtain acoustic images of the samples containing different damage modes and correlate the images with results from conventional approaches and establish a library.

4. Clearly define hardware and software requirements for each individual function and identify elements which would be shared. Study the requirements to coordinate between Optical Inspection, Spectral Analysis, and Acoustic Microscopy functions.

5. Design computer algorithms for automatic defect recognition which could be used for results of optical inspection, spectral analysis and acoustic microscopy, respectively.

6. Study the availability of commercial robots and the necessary modifications to implement the proposed functions in the robot.

7. Report and Phase II Proposal -- To report the results of about mentioned works, and develop a Phase II project to design and implement the proposed MFRS system.

Performance Schedule

(Estimated times needed to complete the task after startup)

Task 1 .... 2 months,   Task 2 .... 3 months,   Task 3 .... 4 months
Task 4 .... 5 months,   Task 5 .... 5 months,   Task 6 .... 5 months
Task 7 .... 6 months,

The Project Plan

```
/-\                    /-\
|X|  Activity          | |  Task
\-/                    \-/
```

Project Number	Project Title	Start/End Date
7121	Real-Time NDE Using MFRS	6/20/91 to 12/20/91

Assign Task #	Description	Duration (weeks)	Est. Compl. Date	Revision Number
1.0	Samples Preparation	2	8/16/91	
2.0	Optical Module Design	4	8/16/91	
3.0	Spectral Analyzer Design	4	9/13/91	
4.0	Acoustic Microscopy Design	4	10/11/91	
5.0	Computer Programs Development	2	11/15/91	
6.0	Coordination of Functions	2	11/15/91	
7.0	Robot	2	11/29/91	
8.0	Monthly & Final Reports	4	12/20/91	
9.0				
10.0				

Work Authorization   Total | 26 |

Director Signature

Page ----- of -----

5

Title: Real-Time NDE Using MFRS

```
                         June -| --------- July ----------| ----  August -

                         24    1     8     15    22    29    5     12
#      Task              |_____|_____|_____|_____|_____|_____|_____|_____


1.0    Sample Preparation |---- ----- ----- ----- ----- ----- ----- ----|
1.1    Samples Design     |---| ..... ..... ..... ..... ..... ..... ....|
1.2    Fabrication (MSU)  ..... |---- ----- ----| ..... ..... ..... ....|
1.3    Pre-Screen         ..... ..... ..... ..... |---| ..... ..... ....|
1.4    Impact/Fatigue (MSU) ..... ..... ..... ..... ..... |---- ----- ----|

2.0    Optical Module     ..... |---- ----- ----- ----- ----- ----- ----|
2.1    Literature Survey  ..... |---| ..... ..... ..... ..... ..... ....|
2.2    Samples Procurement ..... |---- ----- ----- ----| ..... ..... ....|
2.3    Diode Laser Source ..... ..... |---| ..... ..... ..... ..... ....|
2.4    Optics Design      ..... ..... ..... |---- ----| ..... ..... ....|
2.5    Experiments        ..... ..... ..... ..... ..... |---- ----- ----|

3.0    Spectral Analyzer  ..... ..... ..... |---- ----- ----- ----- -----
3.1    Literature Survey  ..... ..... ..... |---| ..... ..... ..... .....
3.2    Pre-Screen Samples ..... ..... ..... ..... |---| ..... ..... .....
3.3    Theoretical Model  ..... ..... ..... ..... |---- ----- ----- -----
3.4    Post-Damage NDE    ..... ..... ..... ..... ..... ..... ..... .....
3.5    Data Correlation   ..... ..... ..... ..... ..... ..... ..... .....
3.6    Circuit Design     ..... ..... ..... ..... ..... ..... ..... .....

4.0    Acoustic Microscopy ..... ..... ..... |---- ----- ----- ----- -----
4.1    Diode Laser Source ..... ..... ..... |---| ..... ..... ..... .....
4.2    Pre-Screen Samples ..... ..... ..... ..... |---| ..... ..... .....
4.3    System Evaluation  ..... ..... ..... ..... ..... |---- ----- ----|
4.4    Post-Damage NDE    ..... ..... ..... ..... ..... ..... ..... .....
4.5    Damage Pattern Analysis ..... ..... ..... ..... ..... ..... ..... .....
4.6    Data Correlation   ..... ..... ..... ..... ..... ..... ..... .....

5.0    Computer Programs  ..... ..... ..... ..... ..... ..... ..... .....
5.1    System Control     ..... ..... ..... ..... ..... ..... ..... .....
5.2    Defect/Damage Detection ..... ..... ..... ..... ..... ..... ..... .....

6.0    Coordination       ..... ..... ..... ..... ..... ..... ..... .....

7.0    Robot              ..... ..... ..... ..... ..... ..... ..... .....

8.0    Report             ..... ..... ..... ..... |---| ..... ..... .....
```

```
     ----------|  ------- September ------|  -------- October ------| ------------

19      26      2       9       16      23      30      7       14      21      28      4       11
|_____|_____|_____|_____|_____|_____|_____|_____|_____|_____|_____|_____|_____


1.....  .....  .....  .....  .....  .....  .....  .....  .....  .....  .....  .....  .....
.....  .....  .....  .....  .....  .....  .....  .....  .....  .....  .....  .....  .....
.....  .....  .....  .....  .....  .....  .....  .....  .....  .....  .....  .....  .....
.....  .....  .....  .....  .....  .....  .....  .....  .....  .....  .....  .....  .....
.....  .....  .....  .....  .....  .....  .....  .....  .....  .....  .....  .....  .....

2.....  .....  .....  .....  .....  .....  .....  .....  .....  .....  .....  .....  .....
.....  .....  .....  .....  .....  .....  .....  .....  .....  .....  .....  .....  .....
.....  .....  .....  .....  .....  .....  .....  .....  .....  .....  .....  .....  .....
.....  .....  .....  .....  .....  .....  .....  .....  .....  .....  .....  .....  .....
.....  .....  .....  .....  .....  .....  .....  .....  .....  .....  .....  .....  .....
.....  .....  .....  .....  .....  .....  .....  .....  .....  .....  .....  .....  .....

3-----  -----  -----  -----  -----  ----|  .....  .....  .....  .....  .....  .....  .....
.....  .....  .....  .....  .....  ....|  .....  .....  .....  .....  .....  .....  .....
.....  .....  .....  .....  .....  ....|  .....  .....  .....  .....  .....  .....  .....
-----  ----|  .....  .....  .....  ....|  .....  .....  .....  .....  .....  .....  .....
|----  ----|  .....  .....  .....  ....|  .....  .....  .....  .....  .....  .....  .....
.....  .....  |----  ----|  .....  ...|  .....  .....  .....  .....  .....  .....  .....
.....  .....  .....  .....  |----  ----|  .....  .....  .....  .....  .....  .....  .....

4-----  -----  -----  -----  -----  -----  -----  ---|  .....  .....  .....  .....  .....
.....  .....  .....  .....  .....  .....  .....  ....|  .....  .....  .....  .....  .....
.....  .....  .....  .....  .....  .....  .....  ....|  .....  .....  .....  .....  .....
.....  .....  .....  .....  .....  .....  .....  ....|  .....  .....  .....  .....  .....
|----  ----|  .....  .....  .....  .....  .....  ....|  .....  .....  .....  .....  .....
.....  .....  |----  ----|  .....  .....  .....  ....|  .....  .....  .....  .....  .....
.....  .....  .....  .....  |----  -----  -----  ----|  .....  .....  .....  .....  .....

5.....  .....  .....  .....  .....  .....  .....  .....  |----  -----  -----  ---|  .....
.....  .....  .....  .....  .....  .....  .....  .....  |---  ----|  ....  ....|  .....
.....  .....  .....  .....  .....  .....  .....  .....  .....  .....  |----  ---|  .....

6.....  .....  .....  .....  .....  .....  .....  .....  |---  -----  -----  ---|  .....

7.....  .....  .....  .....  .....  .....  .....  .....  .....  .....  .....  .....  |----

8|---|  .....  .....  .....  .....  |---|  .....  .....  .....  .....  |---|  .....  .....
```

```
November --|  --------  December -----|

18     25     2      9      16     23     30
|_____|_____|_____|_____|_____|_____|_____|
```

1.0	**Sample Preparation**
1.1	Samples Design
1.2	Fabrication (MSU)
1.3	Pre-Screen
1.4	Impact/Fatigue (MSU)
2.0	**Optical Module**
2.1	Literature Survey
2.2	Samples Procurement
2.3	Diode Laser Source
2.4	Optics Design
2.5	Experiments
3.0	**Spectral Analyzer**
3.1	Literature Survey
3.2	Pre-Screen Samples
3.3	Theoretical Model
3.4	Post-Damage NDE
3.5	Data Correlation
3.6	Circuit Design
4.0	**Acoustic Microscopy**
4.1	Diode Laser Source
4.2	Pre-Screen Samples
4.3	System Evaluation
4.4	Post-Damage NDE
4.5	Damage Pattern Analysis
4.6	Data Correlation
5.0	**Computer Programs**
5.1	System Control
5.2	Defect/Damage Detection
6.0	**Coordination**
7.0	**Robot**
8.0	**Report**

1.2 Research Carried Out

We initiated the project on June 24, 1991, starting with planning, identifying activities/tasks and laying up milestones. Project management has been set to establish a sound basis for scheduling, controlling and modifying the project. we designed a simplified Project WBS (Work Breakdown Structure) and a Gantt chart, showing the proposed activities and tasks.

The project has been broken down to eight main activities, according to the Technical Objectives presented in the Phase I proposal. The activities include: Samples Preparation, Optical Module Design, Spectral Analyzer Design, Acoustic Microscopy Design, Computer Programs Development, Coordination of Function, Robot, and Reports. A number of tasks are assigned for each activity (please refer to the attached Gantt Chart).

We have followed the schedule very well through the Phase I project, although the samples fabricated by MSU came in to Sonoscan a little behind the schedule and the follow-ons, Impact/Fatigue tests on these specimens at MSU and Post-Damage NDE, were delayed.

The work which has been carried out in the Phase I includes the following:

Sample Preparation

We have discussed the project about sample design and fabrication with Professor Henrique Reis of University of Illinois-Champaign and Professor Bong Ho, Michigan State University-E. Lansing, Michigan. I visited Professor Ho at MSU and we decided to fabricate 16 glass/epoxy composite specimens with various lay-ups. These specimens would be conditioned by impact and fatigue, respectively. The NDE would be performed before and after impact or fatigue, to monitor the damage development.

Other composite samples, graphite/epoxy laminates were provided by Professor F. K. Chang, Department of Aeronautics and Astronautics, Stanford University (Stanford, California). These samples had different fiber orientations and thickness. They have been impacted with different degrees of energy.

In addition, numerous specimens (materials and components) have been submitted to Sonoscan for inspection by major materials manufacturers and suppliers in aerospace materials science industry. The materials have covered a wide spectrum, including metal matrix composites, metals, ceramics, polymers and other structural materials.

Optical Module Design

The optical system which would be modulized to be incorporated into MFRS for both Optical Inspection Function (SLM) and Acoustic Microscopy Function (LPAV) was comprehensively reviewed. A flexible, compact optical system incorporating diode laser, optical fiber and optics is required and the modular design of such an optical system that can be used for both functions is not trivial.

The optical system currently implemented in a commercial scanning laser acoustic microscope (SLAM) has been studied and the optics which affect the beam spot size, field of view and working distance between the objective and test sample investigated.

A diode Laser System was employed to replace the HeNe lasers, at a substantially reduced cost and size. This stand alone system uses GaAlAs laser with output power level 15 mw and wavelength 780 nm. The size is only 50 x 50 x 107 mm which meets the requirement for compact size. The laser beam is horizontally deflected by an acousto-optic deflector and vertically scanned by a Galvo mirror. Several optical systems were designed for various requirements in resolution and field-of-view.

In experiments, an Air Force 1951 resolution test target was used to verify the resolution limit for various optical systems. The results follow the analytical prediction. The near-infrared diode laser system demonstrated that the focused spot waist is proportional to the wavelength.

Literature was surveyed to identify critical damage/defect size for various materials. Several silicon nitrides with various size (10 um, 25 um, 50 um and 100 um) laser drilled holes were inspected using SLM function to verify the calculation of beam spot waist and therefore the optical resolution of the SLM.

Spectral Analysis

Several technical reports on theories and analytical models regarding to this subject were reviewed. An analytical model of spectral analysis developed by Professor Chi Hau Chen, Electrical and Computer Engineering Department, University of Massachusetts at Dartmouth was evaluated and selected to be modified and included in the Phase II work.

An electronic kit to build the plug-in circuit board to IBM PC computer was assembled and tested.

A number of materials were tested to gain knowledge in optimizing ultrasound frequencies to be used in Spectral Analysis function. The impacted graphite/epoxy specimens provided by Professor Chang of Stanford University were also inspected by spectral analysis method. The variation in frequency response due to various impact damage were documented. The glass/epoxy composite samples fabricated at MSU have been pre-screened. The results form the spectral analysis were used to form a database, showing the frequency response to various laminates lay-ups.

Acoustic microscopy

The optical system currently implemented in a commercially available SLAM, including laser source, optics, beam deflector and the associated knife-edge Detection technique is comprehensively reviewed and a guideline for design of optics has been established. Acoustic resolution limit as a function of ultrasound frequency was experimentally verified.

Several specimens were inspected by an in-house SLAM to study the available frequencies for various composite materials, optimizing with respect to resolution and penetration of the ultrasound. The potential problem associated with knife-edge detection when incorporated into MFRS was cleared up and alternatives of superheterodyne optical schemes were investigated, which may be implemented in the Phase II.

The impacted glass/epoxy composite samples fabricated at MSU was inspected by SLAM and the results were recorded by a VCR. A C-SAM was also used to produce layer-by-layer images, showing 3-D distribution of delaminations as a result of low-velocity impact. The results were quantitatively analyzed and compared to the analytical prediction of Chang's model. These results have demonstrated the feasibility of incorporating Chang's analytical model into SLAM for real-time NDE of impact damage.

Image Processing Software

A public domain program, Image 1.35, for doing digital image processing and analysis was selected and installed in a Macintosh Computer to analyze the impact damage patterns. It is designed for doing digital image processing and analysis on a Macintosh computer. It can acquire, display, edit, enhance, analyze, print and animate images. It supports many standard image processing functions, including histogram equalization, contrast enhancement, density profiling, smoothing, sharpening, edge detection, median filtering, and spatial convolution with user defined kernels up to 63 x 63. This software demonstrated very useful in digital image analysis. A sophisticated damage pattern recognition algorithm will be developed in Phase II.

Robot Design

Numerous commercially available robot systems were studied. The selection of robot is strongly application-oriented. There are three possible ways to implement the MFRS, depending on the sizes and shapes of the materials or components under test. We have finalized the MFRS design which would be built in the Phase II. However, as discussed earlier, the MFRS is designed to be a flexible, general purpose NDE tool and can be easily customized in accordance with the applications.

Application Survey

Survey of MFRS applications were done by talking to scientists and engineers in the related field, including the industry and government agents, and also by reviewing Sonoscan's commitments to the industry in the past and during the Phase I period.

Several interesting projects were suggested by the industry, including results have been achieved during the Phase I period, including measuring the elastic constants of graphite fibers; assessing damage and stress in glass matrix composites; inspecting machining cracks due to grinding of the materials, evaluating the bonding between ferrite and stainless steel, inspecting the joining in cylinder-in-cylinder, quantifying low-velocity impact damage in composite laminates, monitoring fatigue damage development in structural composite materials, providing statistical process control in the manufacture of metal matrix components, and many others.

After survey, we believe that the proposed MFRS will be well accepted as an on-line inspection and failure analysis tool in the industries of aerospace, material science and microelectronics.

Analytical Models and Computer Algorithms

According to the survey results, we have customized the design of MFRS for specific applications, without loss of generality. Three computer algorithms, namely 3DIMPACT, RTSTRESS and CYLJOIN have been reviewed and designed to apply the MFRS to quantifying the impact damage in composite laminates, assessing stress state of composite materials, and evaluating the bond quality in the joining of a cylinder-in-cylinder structure, respectively, which otherwise have no effective means to do so. Analytical models have been studied and computer algorithms outlined. Of course, most of the above mentioned applications (e.g. NDE of metal matrix composites, and so on) are standard for the MFRS and require little additional effort. Several related experiments have been conducted in the Phase I to demonstrate the applicability.

Experiments

Several experiments have been performed to demonstrate the feasibility of MFRS and the usefulness of the proposed functions, including optical inspection, spectral analysis and acoustic microscopy (CSAM and LPAV). The results agreed very well with expectation. Particularly the results on acoustic microscopic inspection of impacted composite laminates are unique and original. The proposed technique is very promising. The inspection is nondestructive so that the results can be directly used to study the post-damage strength, which otherwise would be impossible using the existing techniques. Representative experimental results will be presented in next chapter.

1.3 Resources Utilized

Consultant/Collaboration

The motivation of developing MFRS and the associated NDE methods was inspired by the conversation with scientists and researchers in the related fields. We have discussed the project about samples design and fabrication with Professor Henrique Reis of University of Illinois-Champaign, Professor Bong Ho of Michigan State University-E. Lansing, Michigan, and Professor F. K. Chang of Stanford University, who served as primary consultants during the course of the Phase I project. They were indeed invaluable resources of background, samples, interpretation and encouragement.

We have established relationships with the major companies in the aerospace materials industry. They were very helpful to us in supplying data and samples for test. We inspected samples from a variety of different materials and processes. Through our good relationship with and our dedication to ultrasonic NDE services to these manufacturers, we got strong support and cooperation. In the Phase II project we will continue the good relationship with universities and industries in order to make the NDE method developed in Phase II more productive and valuable to the aerospace materials users and suppliers.

Several interesting works have been collaborated with universities and the related industries. During the Phase I, the collaborations include:

1). Stanford University - Department of Aeronautics and Astronautics
   Stanford, California

   Quantitatively measuring impact damage in various graphite/epoxy composite laminates.

2). Michigan State University - East Lansing, Michigan
   Composite Materials and Structures Center

   NDE of impact and fatigue damage in glass/epoxy composite laminates.

3). Purdue University - School Aeronautics and Astronautics
   West Lafayette, Indiana.

   Inspecting low-velocity impact in composite laminates.

4). NASA - Lewis Research Center, Cleveland, Ohio

   Measuring the elastic constants of graphite fibers using SLAM, operating in a interferogram mode. Also measuring the stress in a Nicalon (SiC) fiber reinforced LAS (lithium-alumino-silicate) matrix composite, using spatial spectral analysis technique.

5). Lockheed Missiles & Space Co., Inc., Sunnyvale, California. Materials Engineering

Assessing damage and monitoring damage development in S-Glass/epoxy batten materials.

Other collaborators or suppliers of samples such as G.E., Gruman, Boeing Cherry Textron and Cornell University asked us not to reveal any specific information about the proprietary data and processes of materials. Therefore, a large part of the experimental results achieved in Phase I remain confidential and would not be presented here. Only selected results will be reported in next chapter.

SLAM (scanning laser acoustic microscope)

An in-house SLAM was employed to serve as a start of the project in understanding the necessary structures of SLM and LPAV. The SLAM was modified to resemble the proposed LPAV version and was used to inspect the incoming samples through the course of the Phase I.

C-SAM and Rotation Fixture

An in-house C-scanning mode instrument was used to produce layer-by-layer images of defects in test samples. The imaging capability of C-SAM was used during the research, to display an unwrapped, 2-D distribution map of disbonds in the cylindrical structures. However, modification on C-SAM was required to perform cylindrical scanning. The modification included the design and construction of a rotation fixture which rotated the sample during scanning. Eventually, the CSAM on MFRS will be able to follow the contour of sample surface, keeping the transducer normal to the surface.

A-Scan and Spectral Analyzer

Two A-Scan systems were used in the Phase I research. A 10 MHz system was assembled from separate components. The other A-Scan which resided in our C-SAM system was operated at frequencies from 10 up to 50 MHz. A spectrum analyzer was used to display the spectral components of the echoes. Various transducers were evaluated with respect to the operating frequency and F-number. The frequencies investigated were ranging from 15 MHz up to 100 MHz, with F numbers from 1.5 up to 5. A IBM PC plug-in electric circuit board for spectral analysis was assembled and tested. The circuit board worked well to demonstrate the aspects, although the frequency resolution was poor. A more sophisticated circuit for spectral analysis a would be required in the Phase II.

DPA and Optical Microscope

To provide supporting evidence, the tested samples were subject to DPA (destructive physical analysis) and optical inspection. We routinely cross-sectioned the sample in which defects had been found by LPAV and CSAM, and polished it adequately so that they can be viewed by an optical microscope. Excellent agreement has been found between the acoustic images and the DPA results.

Computers

Computer programs were developed on the basis of IBM PC/AT or XT, and their compatible versions. The system control was programmed in the "BASIC" computer language, whereas the computation was in "C" language.

Digital Image Analysis Software

Image 1.35 ia a public domain program developed by National Institute of Health (NIH). It is designed for doing digital image processing and analysis on a Macintosh computer. It can acquire, display, edit, enhance, analyze, print and animate images. It supports many standard image processing functions, including histogram equalization, contrast enhancement, density profiling, smoothing, sharpening, edge detection, median filtering, and spatial convolution with user defined kernels up to 63 x 63. Image 1.35 can be used to measure the area, average density, center of gravity, and angle of orientation of a user defined region of interest. It can be used to measure path lengths and angles. Results can be calibrated to provide real world values. It provides MacPaint-like editing color and gray scale images, including the ability to draw lines, rectangles, ovals and text. It can flip, rotate, invert and scale selections. It supports multiple windows and 8 levels of magnification. All editing, filtering, and measurement functions operate at any level of magnification and are undoable.

A Macintosh IIsi system was installed with the following features:

* Motorola 32-Bit 68030 Processor @ 20 MHz
* 68882 Math Co-processor
* 5 MB RAM/ 80 MB Hard Drive
* Apple 3.5" 1.44 MB SuperDrive
* 512 KB ROM includes support for 32-Bit Addressing, 32-Bit QuickDraw.
* MultiFinder Operating System
* ADB Mouse and Microphone
* AppleColor Hi-Res RGB 13" Monitor

It supports the Data Translation QuickCapture card for digitizing images using a TV camera or from output of either LPAV or C-SAM. Data Translation's QuickCapture is a frame grabber board and software for capturing, processing, and displaying live video images on the Macintosh.

15

2. RESEARCH FINDINGS AND RESULTS IN PHASE I

The research carried out in Phase I has demonstrated the technical feasibility of the concepts underlying the construction of MFRS and the implementation of the proposed NDE methods. Several key questions relevant to MFRS hardware design have been cleared out, including the basic structure of robotic arm, the optical systems to be incorporated into MFRS for both SLM and LPAV functions, and the alternatives for the knife-edge detection technique which is employed in the LPAV function.

Several interesting topics were suggested by the industry and have been completed or partially carried out during Phase I, including measuring the elastic constants of graphite fibers; assessing damage and stress in glass matrix composites; inspecting machining cracks due to grinding of the materials, evaluating the bonding between ferrite and stainless steel, inspecting the joining in cylinder-in-cylinder, quantifying low-velocity impact damage in composite laminates, monitoring fatigue damage development in structural composite materials, providing statistical process control in the manufacture of metal matrix components, and many others.

In experiments, individual functions of MFRS have been demonstrated very effectively in detecting flaws and damage in a variety of materials of interest. A good number of specimens (materials and components) have been submitted to Sonoscan for inspection by major materials manufacturers and suppliers in aerospace materials industry. The materials span a wide range, e.g. metal matrix composites, metals, ceramics, polymers and other structural materials. Some representative results are selected to be presented in this chapter, although a substantial parts of the works in Phase I were remained confidential, due to materials suppliers' request.

In this chapter a summary of specific accomplishes of the Phase I is listed, including the MFRS design, quantification of impact damage, stress assessment in glass matrix composites, bonding evaluation, NDE of metal matrix materials and demonstration of SPC of structural materials. The details of each accomplishment are given in the following sections.

2.1 Summary of Specific Accomplishments

MFRS Design

The modular designs for SLM, LPAV, CSAM and SAPS have clearly been defined and conceptually demonstrated in Phase I. After surveying the potential applications of MFRS, we have determined the format in which the MFRS will be constructed. We also decide the associated NDE methods which will be developed in the Phase II to demonstrate the capabilities of MFRS.

Quantification of Impact Damage

The quantification of delaminations in laminated composites as a result of low velocity impact have been successfully demonstrated, based on the combining information from the damage patterns detected by LPAV or CSAM and the analytical predictions from Chang's model. In experiments, a number of materials having various plies thickness and lay-ups were impacted with different velocities. The results obtained by using the proposed NDE method agreed with those from conventional destructive means. The results are original. These data will be used to correlate with CAI strengths of the impacted specimens in Phase II.

Stress Assessment

Real-time monitoring of stress while applying strain to the test samples has been demonstrated. Several Nicolan fibers reinforced LAS composites were used in the studies. A four-point bending fixture applying a known strain to the sample was placed in the LPAV. The shift in ultrasonic interference fringes was calculated and related to the stress through the effect of acoustoelascity. The results are very encouraging.

Evaluation of Bonding

Samples with different bonding techniques were inspected. LPAV has demonstrated very effective in evaluating the boding quality, including detection of delaminations and voids. CSAM has also proved to be very useful in this application.

NDE of Metal Matrix Composites

Metal matrix composite in different shapes have been inspected. LPAV and CSAM can nondestructively detect delaminations in the samples.

SPC of Structural Materials

The LPAV and CSAM were used to inspect some structural materials, including delaminations associated the fastener holes on composite panels and the fasteners of various materials and processes.

2.2 Quantitative NDE of Impact Damage

An investigation was performed in Phase I to study the damage in Graphite/Epoxy and Glass/Epoxy laminated composites resulting from transversely low-velocity impact. Matrix cracking and interlaminar delaminations were the primary concern of the study.

During the investigation in Phase I, we found that the damage patterns detected by the LPAV, regardless of the overlapping, agreed very well with the prediction given by Professor Chang of Stanford University, Stanford, California. The encouraging finding motivates us to include the development of a nondestructive 3-D Impact Damage analyzer in the proposed MFRS' Acoustic Microscopy Function.

In order to verify the applicability of Chang's model as described in previous chapter, numerical predictions from the model were compared with the data generated by the impact tests, for controlled conditions, performed during the investigation in Phase I.

The impact specimens prepared by MSU, together with Chang's samples, were used to evaluate Chang's analytical model as described in previous report. They have been inspected by both SLAM and C-SAM. The results were quantitatively analyzed by an image analysis software, Image 1.35.

A public domain program, Image 1.35, for doing digital image processing and analysis was selected and installed in a Macintosh Computer to analyze the impact damage patterns.

The results from SLAM images, C-SAM images and X-Radiographs of Chang's samples were quantitatively compared. The correlation between data from SLAM, C-SAM and X-Radiograph is excellent.

2.2.1 Samples from Stanford University

A C-Scan mode acoustic microscope (CSAM) and a through-transmission laser probing acoustic vision (LPAV) were used to nondestructively and quantitatively measure the damage areas in graphite/epoxy composite plates which had been subjected to low-velocity impact. LPAV provides an overview of the impact damage instantly, while C-SAM delineates delamination profile at each interface in the laminated composite. An analytical model, Chang's Model, was employed to synthesize the damage pattern at each interface, based on the delamination profiles visualized by SLAM and C-SAM. The delamination area was quantitatively measured for each interface.

Impact Conditions

An investigation was performed to study the damage in Graphite/Epoxy composite laminates resulting from transverse low-velocity impact. Matrix cracking and interlaminar delaminations were the primary concern of the study. The testing facility is described in reference [21]. A spherical-nosed impactor was used for the study. The radius of the spherical nose head made of steel was 0.635 cm. The specimens were firmly clamped along two parallel edges. T300/976 composite laminates with ply orientation $[0_3/90_3/0_3/90_3/0_3]$ were selected for the study. The dimensions of each specimen were 10 cm long and 6.6 cm wide. Each specimen was impacted at a selected impact velocity. Specimens were then inspected by LPAV, C-SAM and X-ray, for comparison.

LPAV Inspection

A 10 MHz LPAV image is shown in Fig. 1, displaying an overview of impact damage in a T300/976 composite laminate with a ply orientation $[0_3/90_3/0_3/90_3/0_3]$. The damage was caused by a impactor with 0.16 Kg mass at a velocity of 6.70 m/s. The field of view is 45 mm by 26 mm. In LPAV image, the black region represents the delaminations which block the transmission of ultrasound, while the white region represents damage-free area. The damage pattern shown in LPAV image is a projected view of delaminations occurred at all laminated interfaces throughout the specimen thickness. The LPAV image was produced at a video rate, or 1/30 second.

C-SAM Inspection

A 10 MHz C-SAM system was used to inspect the delaminations layer by layer within the impacted specimen. The transducer has a 0.25" element and 0.5" focal length and The scan size is 52.0 mm by 48.8 mm. During inspection the transducer was physically lowered in order to focus the

ultrasound beam at a specified depth (or interface). An electronic gate was activated at corresponding time to extract the return echoes at the specific level. The delaminations as a result of low velocity impact were expected to take place at the interfaces where the fiber orientation of the top layer was different from that of the bottom layer. Four C-SAM images are shown in Fig. 2, displaying delamination patterns at the first, second, third and forth interface, respectively.

In these C-SAM images, the gray color bar on the left of each image indicates the amplitudes of return echoes. The white at the center of the bar represents zero, or low reflection which usually indicates a good bonding condition at the interface. The gray colors, changing from white toward dark, represent gradually increasing amplitudes of return echoes. Therefore, the delamination areas are displayed in dark colors. It is clear that each delamination oriented itself along the fiber direction of the bottom ply of the laminated interface. Please note that part of the delamination pattern was shadowed by prior layers.

Analytical Prediction

To overcome the overlapping limitations, the predicted delamination for the above mentioned impact condition is presented in Fig.3. The prediction was made by employing the analytical model described in literature [21]. Accordingly, the shadowed part of each delamination shown in C-SAM images could be synthesized by the computed shapes at the corresponding laminated interface. The delamination area was then calculated by the Image 1.35.

The delamination profiles at consecutive laminated interfaces as shown in Figure 2 were reconstructed and calculated to be, 43, 172, 184 and 326 mm^2, respectively, and the total delamination area in the impacted specimen is added up to be 725 mm^2, which is tabulated in Table 1. These data can later be used to correlate with the CAI (compression-after-impact) strength.

Data Correlation

To verify the accuracy of the measurement, the specimen was X-rayed using enhanced dye-penetrant. A small hole was drilled at the impacted location and dye-penetrant was applied through the hole. An X-Radiograph was then taken and is shown in Fig. 4. The delamination areas on the X-radiograph were calculated, for each delaminated interface, to be 35, 171, 180 and 338 mm^2, respectively. The total delamination area was 724 mm^2. It agrees very well with the calculation results from C-SAM images.

2.2.2 Samples from Michigan State University

The glass/epoxy composite specimens fabricated by MSU have different lay-ups as follows:

Specimen As: $[0_5/90_5/0_5]_{15}$

Specimen Bs: $[0_3/90_3/0_3/90_3/0_3]_{15}$

Specimen Cs: $[0_2/90_2/0_2/90_2/0_2/90_2/0_2]_{14}$

Specimen Ds: $[0/90/0/90/\ldots\ldots 0/90/0]_{15}$

Two specimens in each group have been selected to be impacted at different speeds to study the damage development in various lay-up structure composites as a result of low-velocity impact. The impact conditions (impact strength, velocity and energy as a function of time) for Specimens B3, B4, C3 and C4, respectively, are shown in Fig. 5.

LPAV Inspection

The 10 MHz LPAV images for Specimens B3, B4, C3 and C4, respectively, are shown in Fig. 6, displaying an overview of the impact damage. The damage was caused by a impactor with a condition described in Fig. 5, respectively. The composite view is composed of several individual images whose field of view is 35 mm by 26 mm. In SLAM image, the black region represents the delaminations which block the transmission of ultrasound, while the white region represents damage-free area. The damage pattern shown in SLAM image is a projection of delaminations occurred at all laminated interfaces throughout the thickness of the specimen. The individual delaminations at each interface can be delineated by using the 3DIMPACT model as described in previous chapter.

CSAM Inspection

A 10 MHz C-SAM system was used to inspect the delaminations layer by layer within the impacted specimen. The transducer has a 0.25" element and 0.5" focal length and The scan size is 52.0 mm by 48.8 mm. During inspection the transducer was physically lowered in order to focus the ultrasound beam at a specified depth (or interface). An electronic gate was activated at corresponding time to extract the return echoes at the specific level. The delaminations as a result of low velocity impact were expected to take place at the interfaces where the fiber orientation of the top layer was different from that of the bottom layer.

Four CSAM images are shown in Fig. 7, displaying delamination patterns at each interface for Specimens B3, B4, C3 and C4, respectively. There are four separate C-SAM images for Specimens B3, and B4, representing delamination the first, second, third and forth interface, respectively. However, for Specimens C3 and C4, the 3rd, 4th, 5th, 7th and 8th C-SAM images in the 3 x 3 images array are representing the first, second, third, forth and fifth interfaces within the samples, respectively.

The delamination areas are displayed in dark colors. It is clear that each delamination oriented itself along the fiber direction of the bottom ply of the laminated interface. Please note that part of the delamination pattern was shadowed by prior layers.

Calculation of Delamination Areas

The delamination profiles at consecutive laminated interfaces as shown in Fig. 7 were reconstructed by Chang's model and were calculated by using the Image 1.35. The results are listed in Table 2 and Table 3, respectively, for each specimens. It is found that the total delamination area is increasing proportionally to the increase of impact energy.

The percentage distribution of delaminations at each interface within each sample are tabulated in Tables 4 and 5. It is clear that most of the damage are located at the lowest interfaces.

2.2.3 Impact Damage Analysis

The data for those impacted specimens from MSU have been further analyzed and the quantitative data are presented here. It is our intention to analyze the data quantitatively and draw the delamination profile at each interface so that one can easily "see" what has happened within the laminated composites during impact, as a function of impact energy as well as fiber orientations. These data can then be used to correlate with the CAI Strength. Although the CAI testing was aborted due to buckling of the plates during testing, we think the proposed technique has the potential to predict the post-damage strength based on the information gathered by LPAV. The correlation will be done in Phase II.

As described in previous section, the delamination profiles at consecutive laminated interfaces as shown in Fig. 7 were reconstructed by the method described in previous chapter and are listed in Tables 2 and 3, respectively, for the Specimens B3, B4, C3 and C4. It is found that the total delamination area is increasing proportionally to the increase of impact energy, despite of fiber orientation. For example, the total delamination area in B4 increases by 1.47 times when the total impact energy increases by 1.58 times, compared to the case of B3. In the case for Specimens C3 and C4, the total delaminations increases by 1.53 when the energy increases by 1.54. Reviewing the data one can find that most of the increase in delamination area comes from the last two interfaces, the 3rd and 4th in B3 and B4 and the 5th and 6th in C3 and C4.

Delamination vs. Impact Energy

As described above, it is found that the total delamination area is increasing proportionally to the increase of impact energy, despite of fiber orientation. For example, the total delamination area in Specimen B4 increases by 1.47 times when the total impact energy increases by 1.58 times, compared to the Specimen B3.

In the case for Specimens C3 and C4, the total delaminations increases by 1.53 when the energy increases by 1.54. Reviewing the data one can find that most of the increase in delamination area comes from the last two interfaces, the 3rd and 4th in B3 and B4 and the 5th and 6th in C3 and C4. Remember that Specimens B3 and B4 have four interfaces in a fiber lay-up of $[0_3/90_3/0_3/90_3/0_3]_{15}$, while Specimens C3 and C4 have six interfaces in a lay-up of $[0_2/90_2/0_2/90_2/0_2/90_2/0_2]_{14}$.

We intend to quantify the impact damage and draw the delamination profile at each interface so that one can easily "see" what has happened within the laminated composites during impact, as a function of impact energy.

Fig. 9 shows the delaminations for laminated interfaces in Specimens B3 and B4. The delaminations as a result of low velocity impact were expected to take place at the interfaces where the fiber orientation of the top layer was different from that of the bottom layer. Therefore the delaminations occurred at a depth of 3, 6, 9 and 12 layer thickness, respectively where the fiber orientation changes, despite of the impact energy. The increase in impact energy only results in a proportional increase in total delamination area, as shown in Fig. 9.

Fig. 10 shows the delaminations for laminated interfaces in Specimens C3 and C4, having a fiber lay-up of $[0_2/90_2/0_2/90_2/0_2/90_2/0_2]_{14}$. The delaminations were expected to take place at a depth of 2, 4, 6, 8, 10, and 12 layer thickness, respectively where the fiber orientation changes, despite of the impact energy. Again, the increase in impact energy only results in a proportional increase in total delamination area.

Delamination vs. Fiber Orientation

To investigate the effect of fiber orientation on the impact delaminations, the quantitative measured results for Specimens B4 and C4 are plotted in Fig. 11 for comparison. Remember that Specimen B4 has four interfaces in $[0_3/90_3/0_3/90_3/0_3]_{15}$, while C4 has six interfaces in a $[0_2/90_2/0_2/90_2/0_2/90_2/0_2]_{14}$ lay-up. The delaminations at each interface were drew for Specimens B4 and C4 so that one can easily "see" what has happened within the laminated composites during impact, as a function of fiber orientation.

In Fig. 11 the delaminations in Specimen B4 occurred at a depth of 3, 6, 9 and 12 layer thickness, respectively, while the delaminations took place at a depth of 2, 4, 6, 8, 10, and 12 layer thickness. Both specimens were subjected to nearly the same impact energy. The Specimen B4 was impacted with an energy 13.25 ft-lb. The impact energy for Specimen C4 was 13.58 ft-lb.

The Specimen C4 experienced more laminated interfaces than Specimen B4. The Specimen C4 has 6 laminated interfaces while Specimen B4 has only 4. However the total delamination area in C4 is less than that in B4. The total delamination area in C4 is 13.94 cm^2, compared to 15.22 cm^2 in B4. Of course, we have to bear in mind that B4 is thicker than C4 by one layer. B4 has 15 layers in total and C4 has 14 layers. This may account for the decrease in delamination area as a result of decreasing thickness.

One of the critical factors in design of composite laminates is impact tolerance. The total delamination becomes a meaningful precursor only when it can be related to post-damage strength, or the CAI strength. The purpose of this study is to find a technique which will predict the CAI strength based on a quantity that can be derived from the real-time image produced by LPAV.

2.2.4 Compression-After-Impact Testing

There are a variety of toughness tests from which to choose to assess the improved damage tolerance composites under development. One of the tests most favored by the aerospace industries and materials suppliers, however, is compression-after-impact (CAI) strength.

CAI testing is a two-step process. Impacting of a panel is followed by determination of the residual compressive strength and strain. Each of these steps represents a different mechanism. The impact step is mostly a Mode II type high-shear-rate propagation, whereas the compression test is more of a stability test of the damaged test specimen. In the latter case, the crack-opening Mode I is dominant under compressive loading (Figure 12).

The CAI testing at Michigan State University was aborted due to the buckling of the plates during testing (see attached letter). Although the CAI testing was forced to be aborted, we strongly believe that the proposed technique has the potential to predict the post-damage strength based on the information gathered by SLAM. The correlation will be done in Phase II. In order to properly perform the CAI testing, a CAI fixture following NASA or SACMA method is a must. We think it is justified to postpone the testing and to be included in the Phase II.

2.2.5 Conclusion

Several laminated composites with various ply orientations were selected for the study. The specimens were impacted at different velocities. Specimens were then inspected by LPAV, C-SAM and X-ray. LPAV displays a projected view of all delaminations in real time, while C-SAM provides detail information about the delamination area at each laminated interface. The sizes and shapes of the delaminations shown on SLAM and C-SAM images were compared to the predicted delamination sizes by an analytical model. The shadowed part of the damage patterns shown in the C-SAM images, because of overlapping, were synthesized and reconstructed by following the analytical prediction. The total delamination area detected by C-SAM was then reconstructed by Chang's model and calculated by the Image 1.35 software. The agreement between the data from C-SAM and that from X-Radiograph is excellent. This technique provides us a tool to quantitatively characterize the impact damage which is critically important in the design of impact-resistant structural materials. The results on quantitative measurements of delaminations will be correlated with CAI Strength of the impacted specimens, which will be the task of the Phase II.

Fig. 1 10 MHz SLAM image, showing projection of all delaminations in a T300/976 composite with ply orientation $[0_3/90_3/0_3/90_3/0_3]$. The damage was caused by a 0.16 Kg impactor at a speed of 6.7 m/s. The field of view is 45 mm x 26 mm.
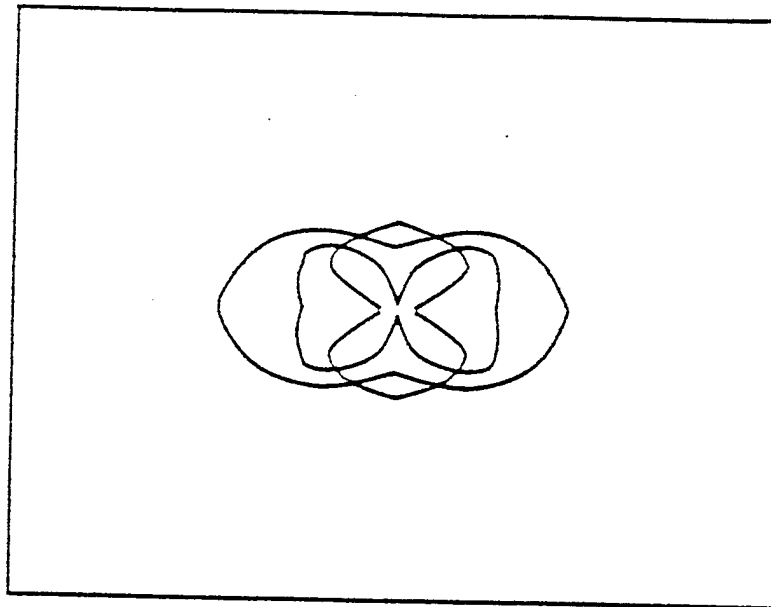
Mass = 0.16 Kg   Velocity = 6.70 m/sec

Fig. 3 The predicted delamination sizes of $[0_3/90_3/0_3/90_3/0_3]$ composites corresponding to the impact condition given in Figure 1.
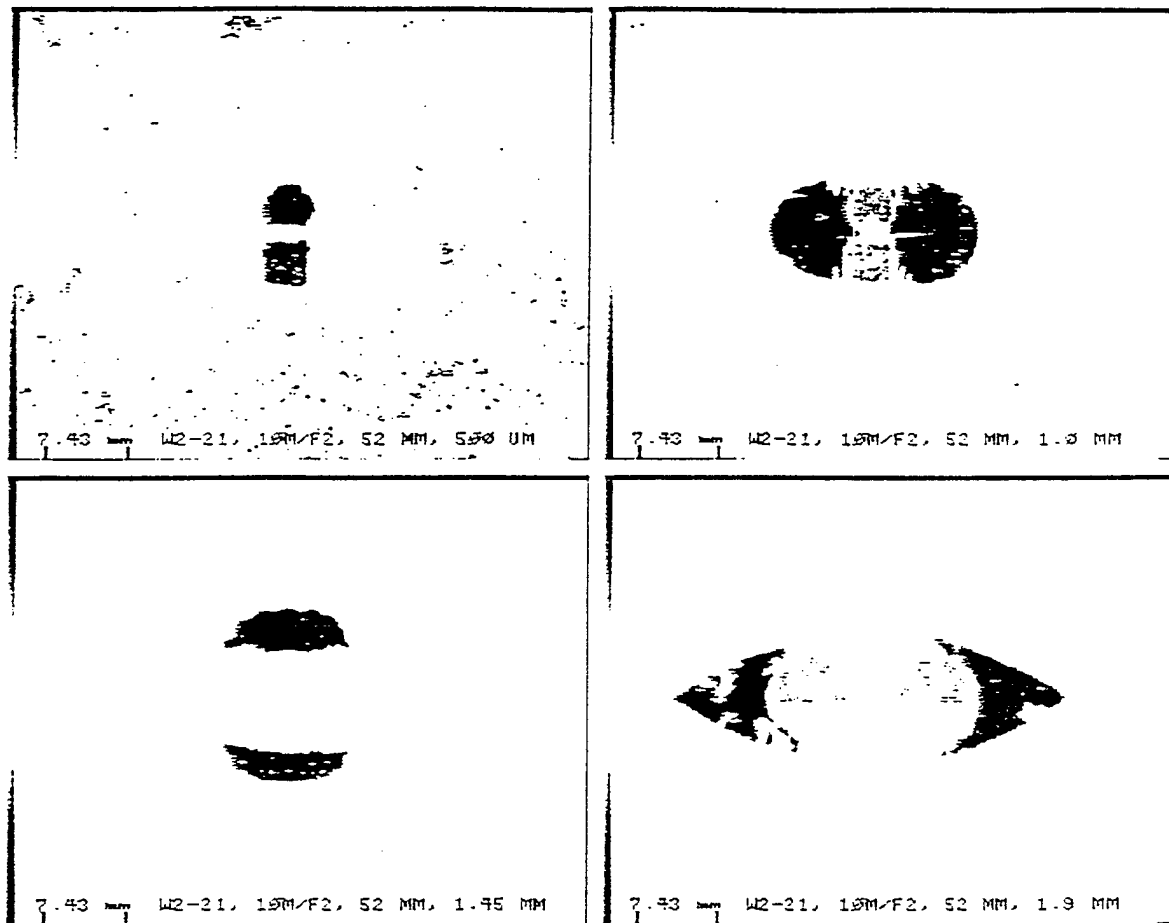
Fig. 2 Four 10 MHz C-SAM images for delaminations at each laminated interface: (a) first interface at 0.45 mm below the surface, (b) second interface at 0.9 mm, (c) third interface at 1.35 mm, and (d) forth interface at 1.8 mm. The scan size is 50 mm x 48.8 mm.
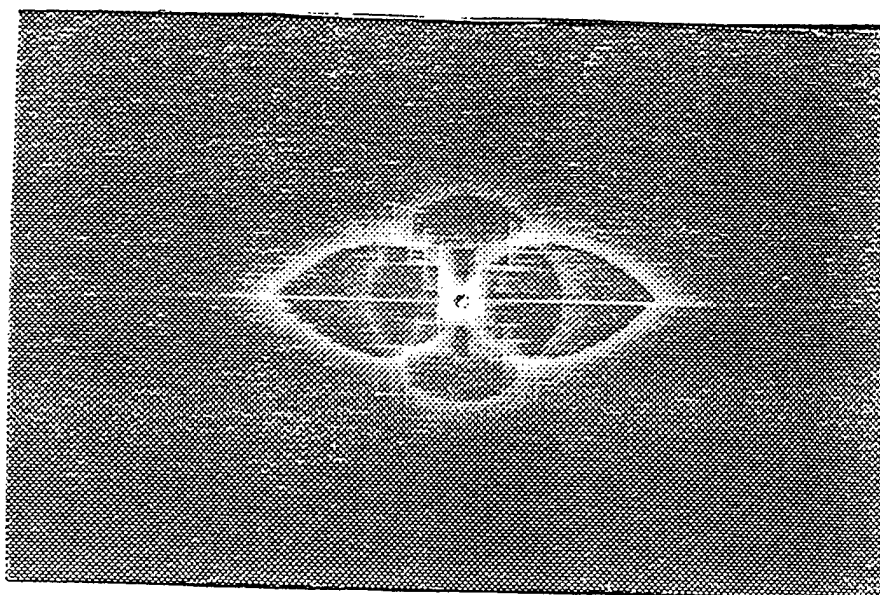
Fig. 4 X-Radiograph of the same impacted $[0_3/90_3/0_3/90_3/0_3]$ composites as shown in Figure 1.

TABLE 1 Comparison of results on delamination sizes measured from C-SAM images which have been modified based on analytical prediction and from X-Radiograph, respectively.

Method \ Delamination	C-SAM (mm2)	(%)	X-Radiograph (mm2)	(%)
1st Interface	43	5.9	35	4.8
2nd Interface	172	23.7	171	23.5
3rd Interface	184	25.4	182	25.1
4th Interface	326	45.0	338	46.6
total	725	100.0	726	100.0

TABLE 2 Quantitative measurements of delaminations at each interface within Specimens B3 and B4, with a lay-up of $[0_3/90_3/0_3/90_3/0_3]_{15}$

Specimen ID Interface	B3 (cm2)	B4 (cm2)	B4/B3 ratio
1st	0.68	0.61	0.90
2nd	2.15	2.89	1.35
3rd	2.70	4.21	1.56
4th	4.83	7.51	1.55
Total Delam.	10.36	15.22	1.47
Impact Energy	8.36	13.25	1.58

TABLE 3 Quantitative measurements of delaminations at each interface within Specimens C3 and C4 with a lay-up of $[0_2/90_2/0_2/90_2/0_2/90_2/0_2]_{14}$.

Specimen ID Interface	C3 (cm2)	C4 (cm2)	C4/C3 ratio
1st	0.16	0.20	1.26
2nd	1.38	1.77	1.28
3rd	1.39	1.92	1.39
4th	1.45	1.87	1.29
5th	1.77	2.89	1.64
6th	2.95	5.29	1.79
Total Delam.	9.10	13.94	1.53
Impact Energy	8.81	13.58	1.54

TABLE 4 Percentage distribution of delaminations at each interface within Specimens B3 and B4, with a structural lay-up of $[0_3/90_3/0_3/90_3/0_3]_{15}$.

Specimen ID Interface	B3 (%)	B4 (%)	B4/B3 change
1st	6.6	4.0	- 2.6
2nd	20.8	19.0	- 1.8
3rd	26.0	27.7	+ 1.7
4th	46.6	49.3	+ 2.7
Total Delam.	10.36 cm2	15.22 cm2	1.47
Impact Energy	8.36	13.25	1.58

TABLE 5 Percentage distribution of delaminations at each interface within Specimens C3 and C4, with a structural lay-up of $[0_2/90_2/0_2/90_2/0_2/90_2/0_2]_{14}$.

Specimen ID Interface	C3 (%)	C4 (%)	C4/C3 Change
1st	1.8	1.4	- 0.4
2nd	15.2	12.7	- 2.5
3rd	15.3	13.8	- 1.5
4th	15.8	13.5	- 2.3
5th	19.5	20.7	+ 1.2
6th	32.4	37.9	+ 5.5
Total Delam.	9.10	13.94	1.53
Impact Energy	8.81	13.58	1.54
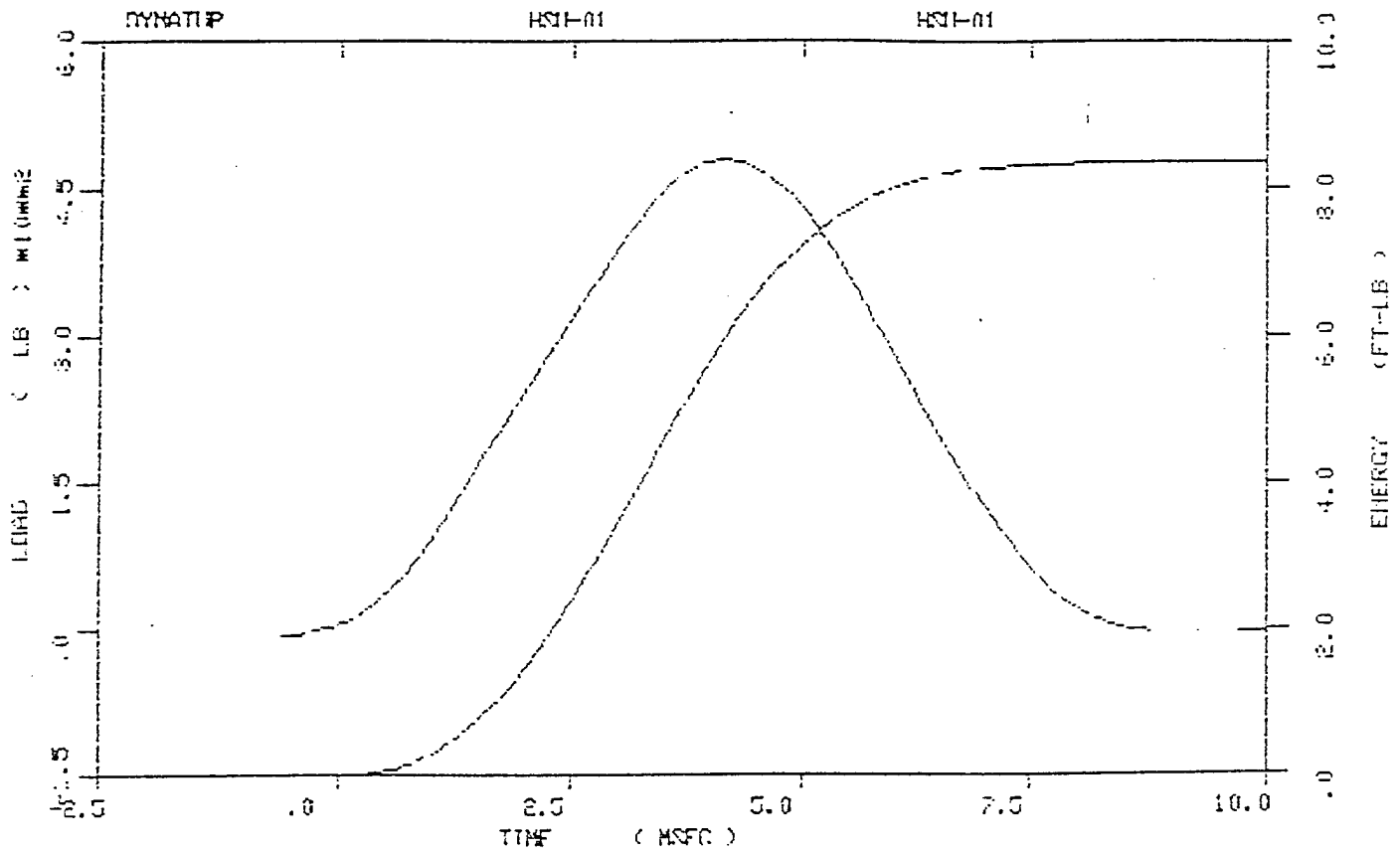
Fig. 5 (a)   Impact condition for Specimen B3.

B4
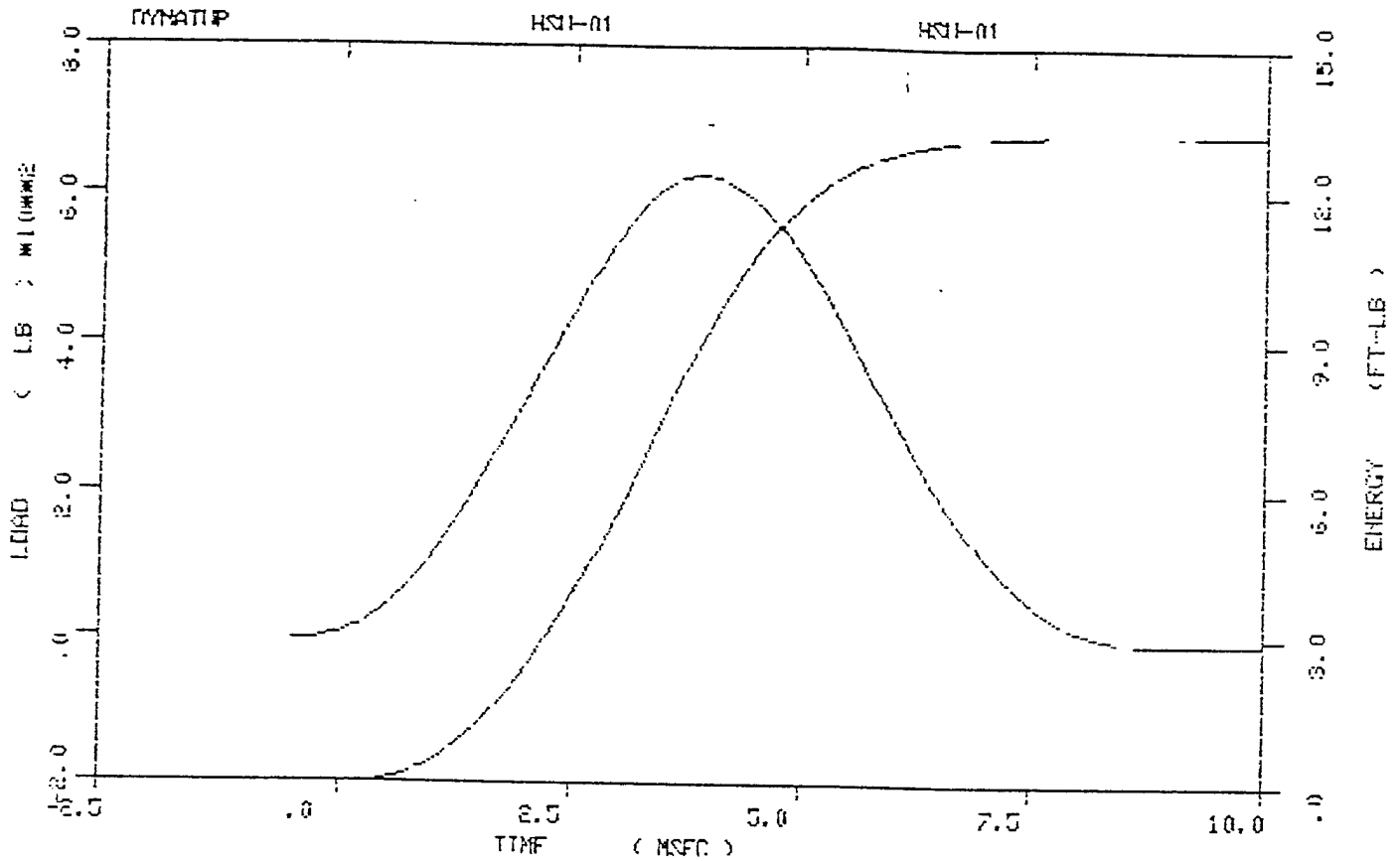
□	Impact Velocity (ft/sec)	Impact Energy (ft-lb)	Time to Max. Ld (msec)	Total Time (msec)	Maximum Load (lb)	Energy to Max.Ld (ft-lb)	Total Energy (ft-lb)
	9.16	13.84	3.85	8.40	626.17	8.88	13.25

Dynatup

Fig. 5 (b)   Impact condition for Specimen B4.

C4
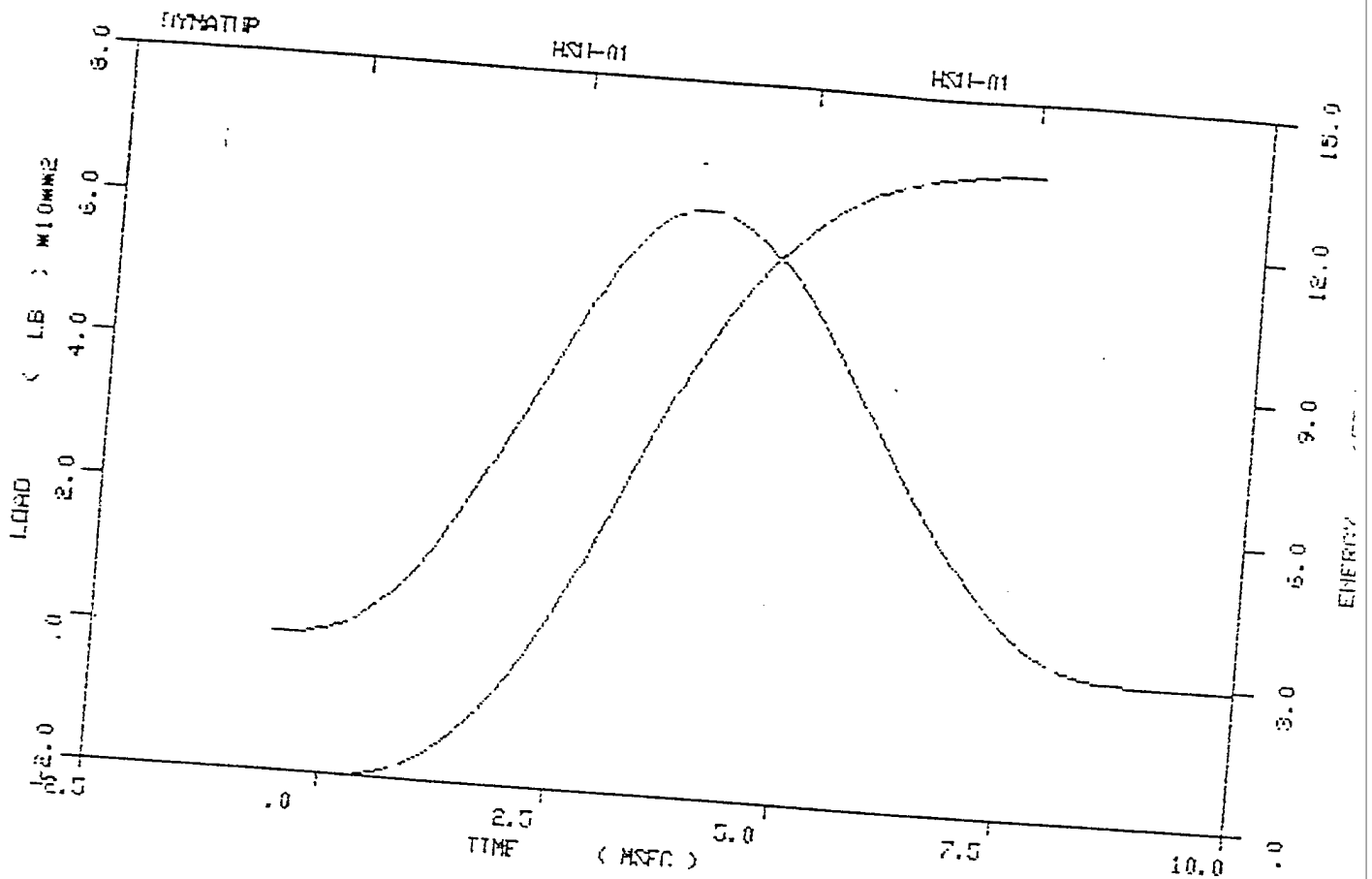
Sp#	Impact Velocity (ft/sec)	Impact Energy (ft-lb)	Time to Max. Ld (msec)	Total Time (msec)	Maximum Load (lb)	Energy to Max.Ld (ft-lb)	Total Energy (ft-lb)
7	9.27	13.35	3.99	8.75	624.65	9.14	13.58

Fig. 5(c)   Impact condition for Specimen C4.

C3
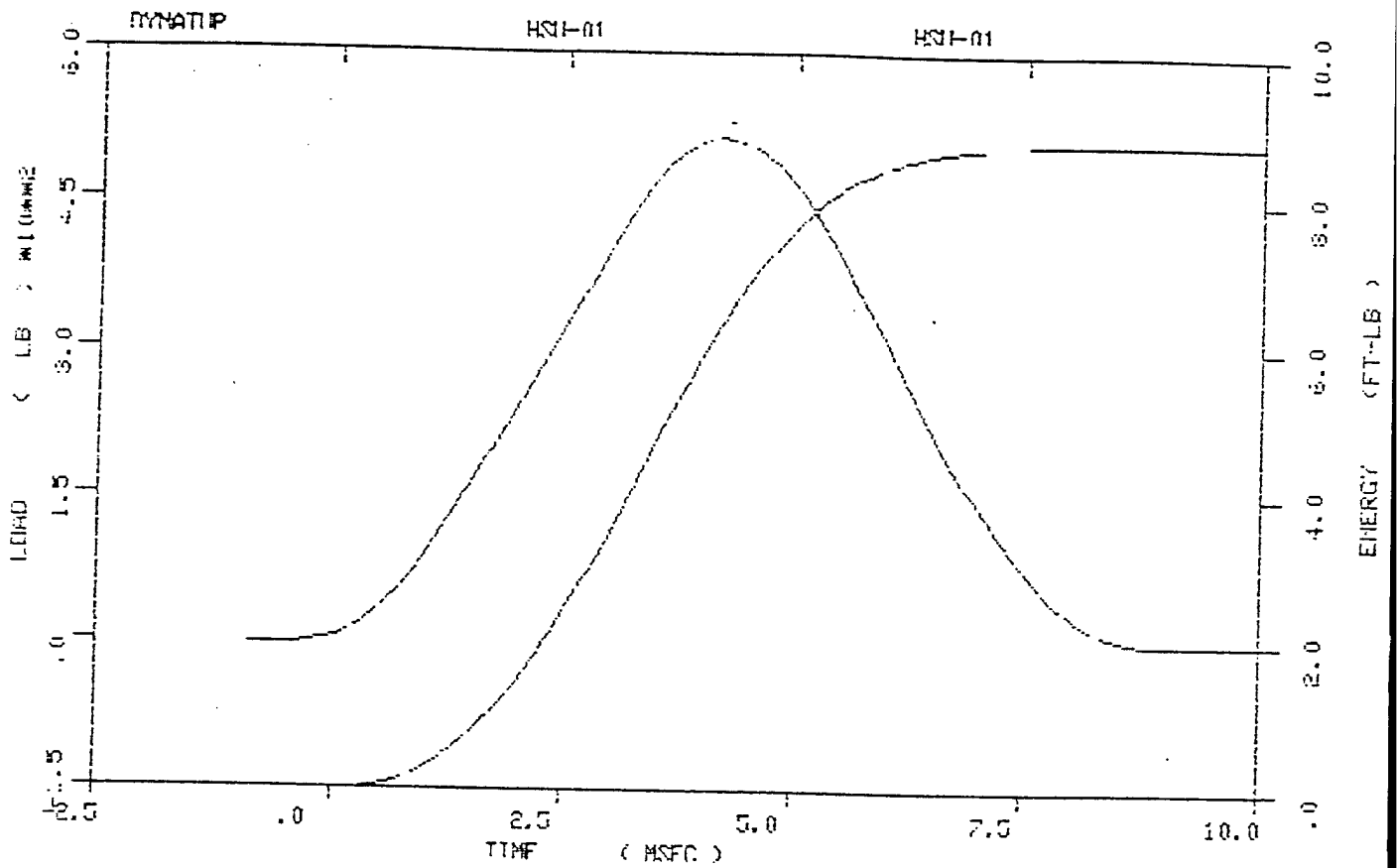
Impact Velocity (ft/sec)	Impact Energy (ft-lb)	Time to Max. Ld (msec)	Total Time (msec)	Maximum Load (lb)	Energy to Max.Ld (ft-lb)	Total Energy (ft-lb)
7.48	8.52	4.28	9.95	514.95	6.32	8.81

Fig. 5(d)   Impact condition for Specimen C3.

Fig. 6 (a) SLAM image of Specimen B3.
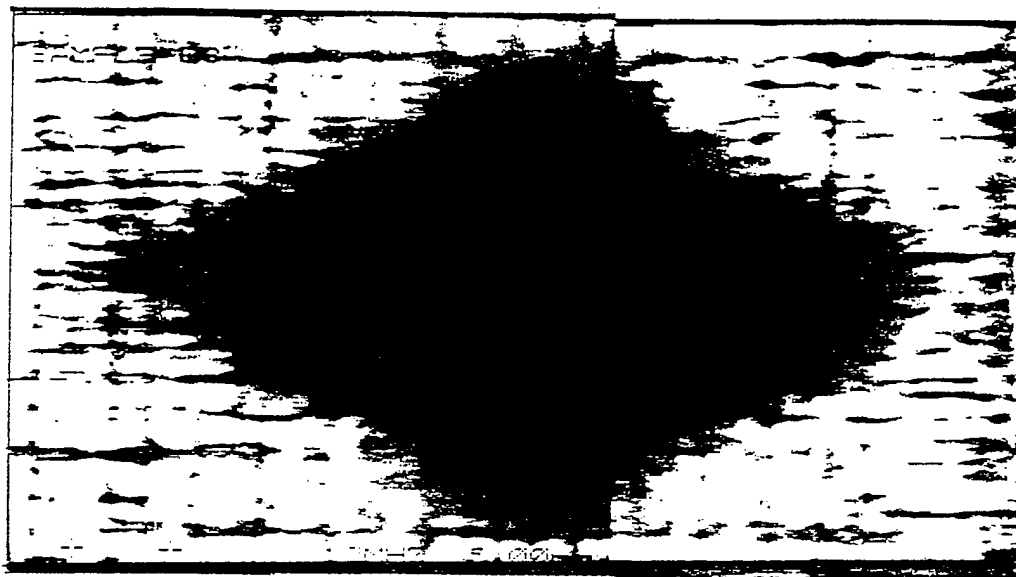
Fig. 6 (b) SLAM image of Specimen B4.
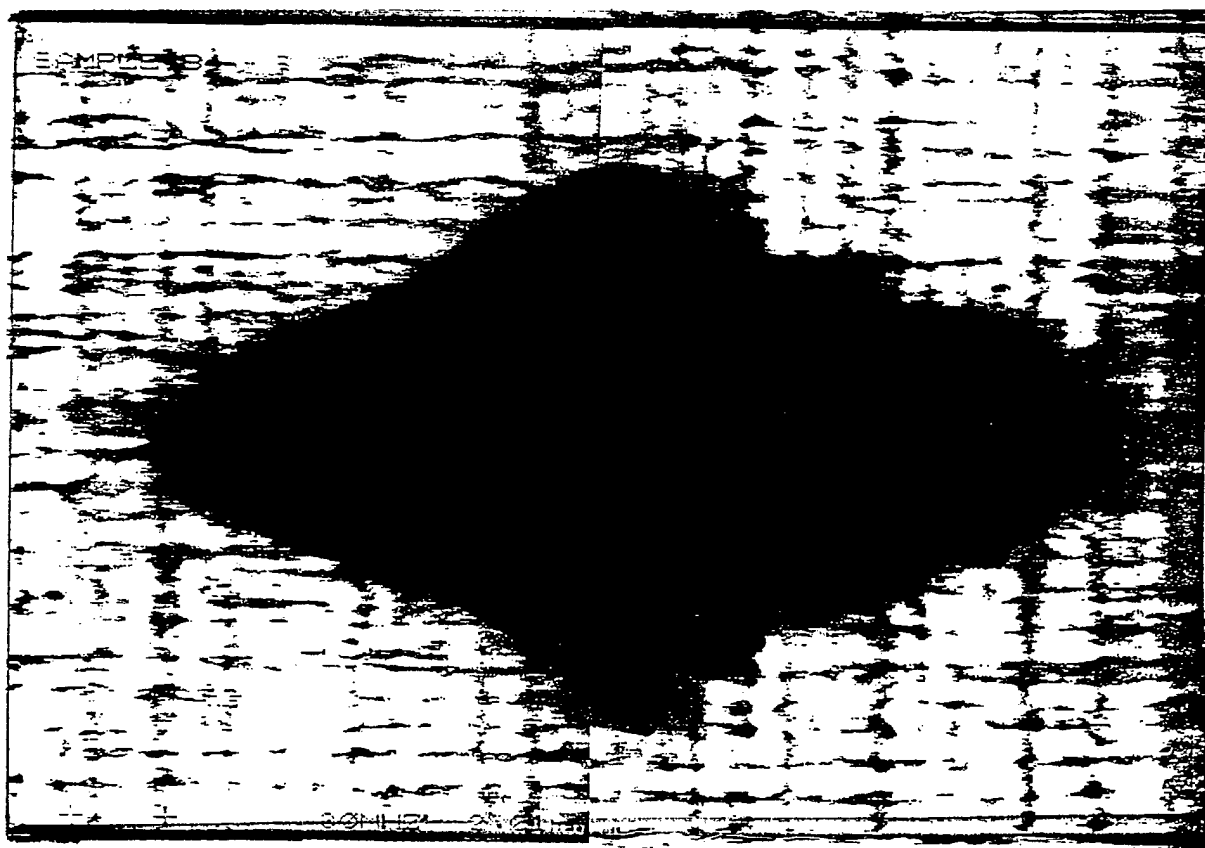
Fig. 6 (c)   SLAM image of Specimen C3.
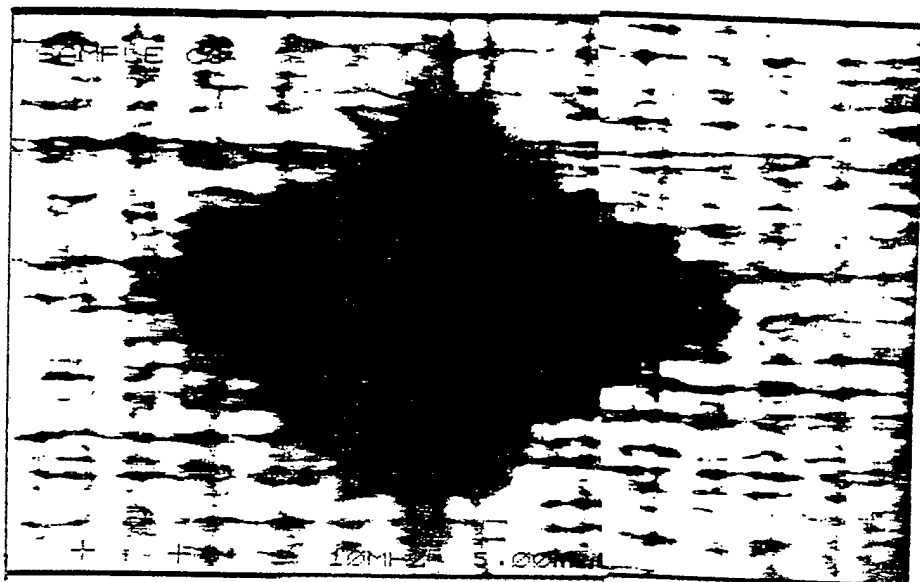
Fig. 6 (d)   SLAM image of Specimen C4.
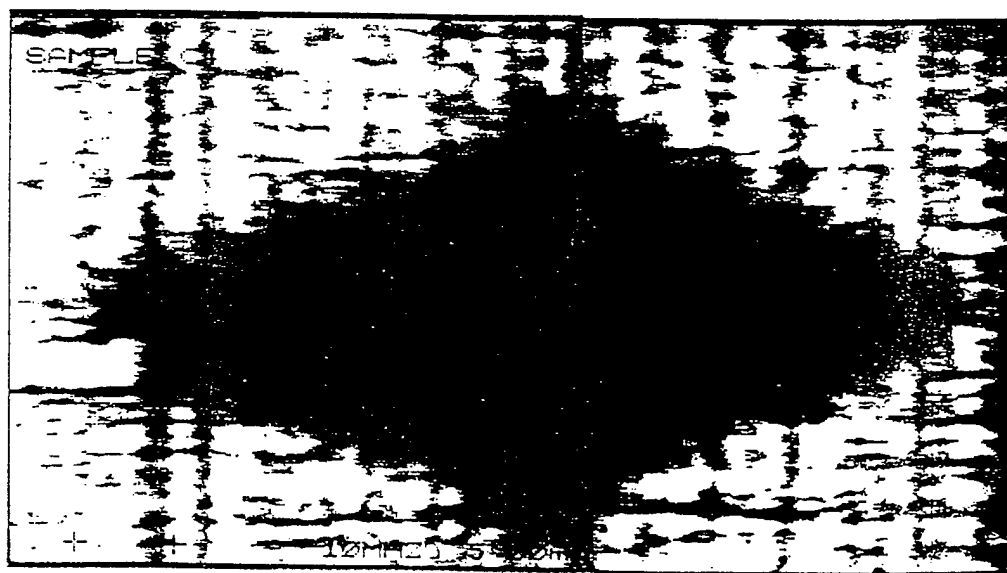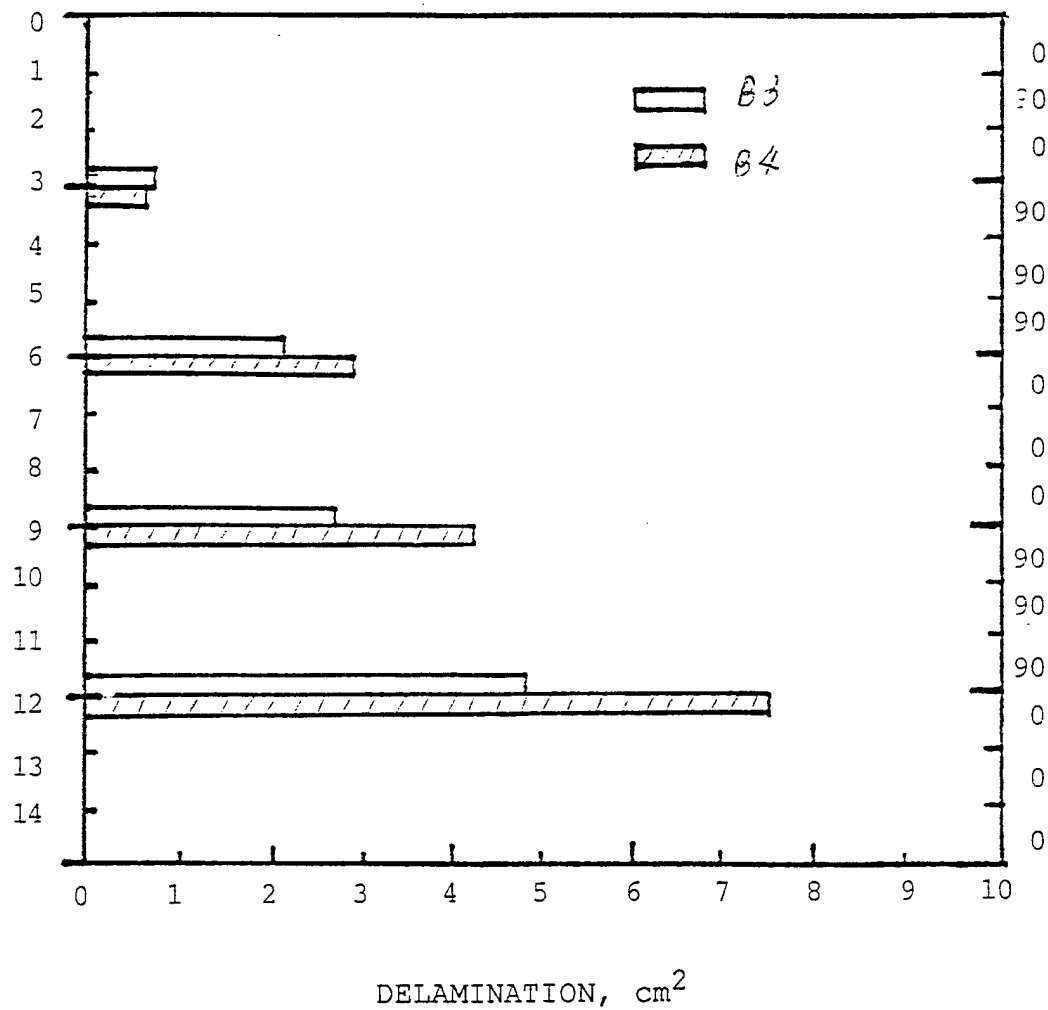
Fig. 9 Measured delaminations at laminated interfaces for Specimen B3 impacted with an energy of 8.36 ft-lb, and Specimen B4 impacted with an energy of 13.25 ft-lb. The total delamination areas for Specimen B3 and B4 are 10.36 and 15.22 cm^2, respectively.

37
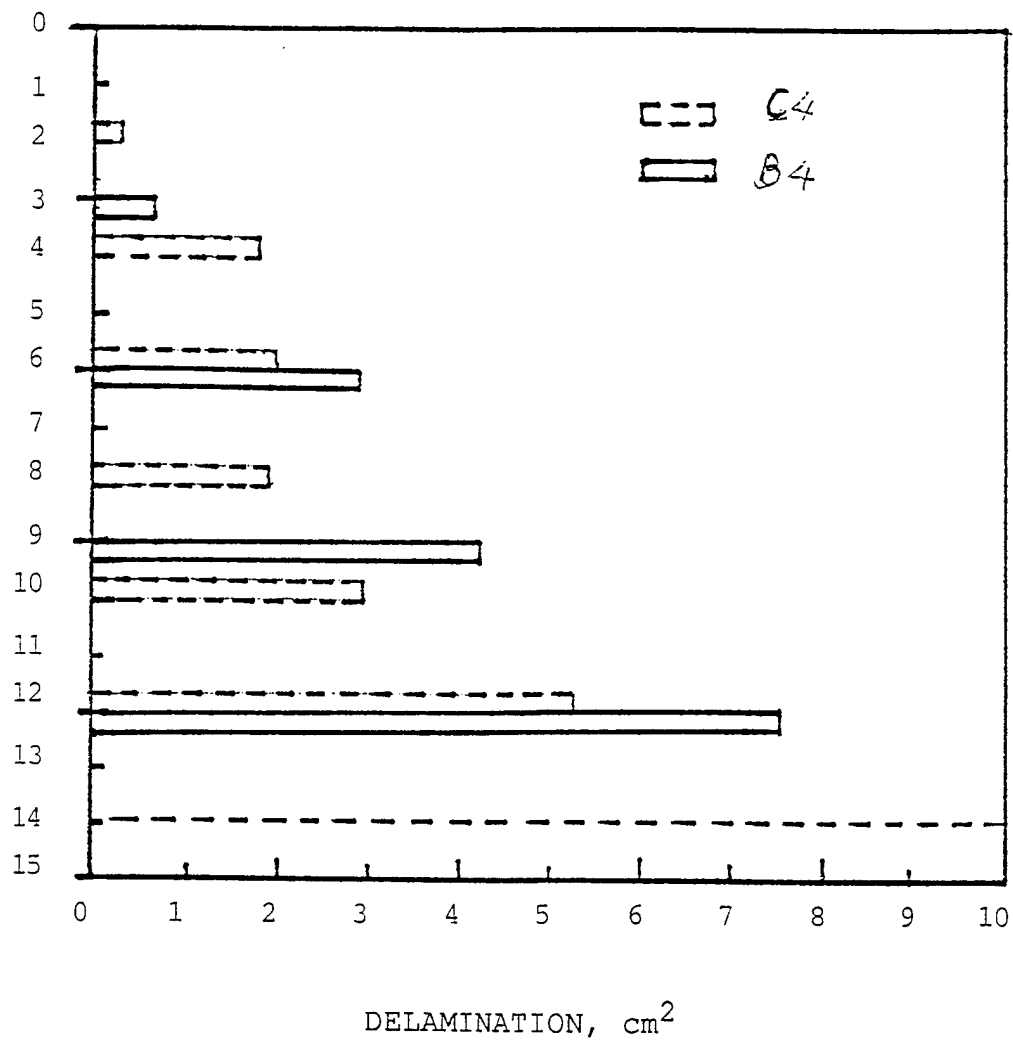
Fig. 10 Measured delaminations at laminated interfaces for Specimen B4 impacted with an energy of 13.25 ft-lb, and Specimen C4 impacted with an energy of 13.58 ft-lb. The total delamination areas for Specimen B4 and C4 are 15.22 and 13.94 cm^2, respectively.
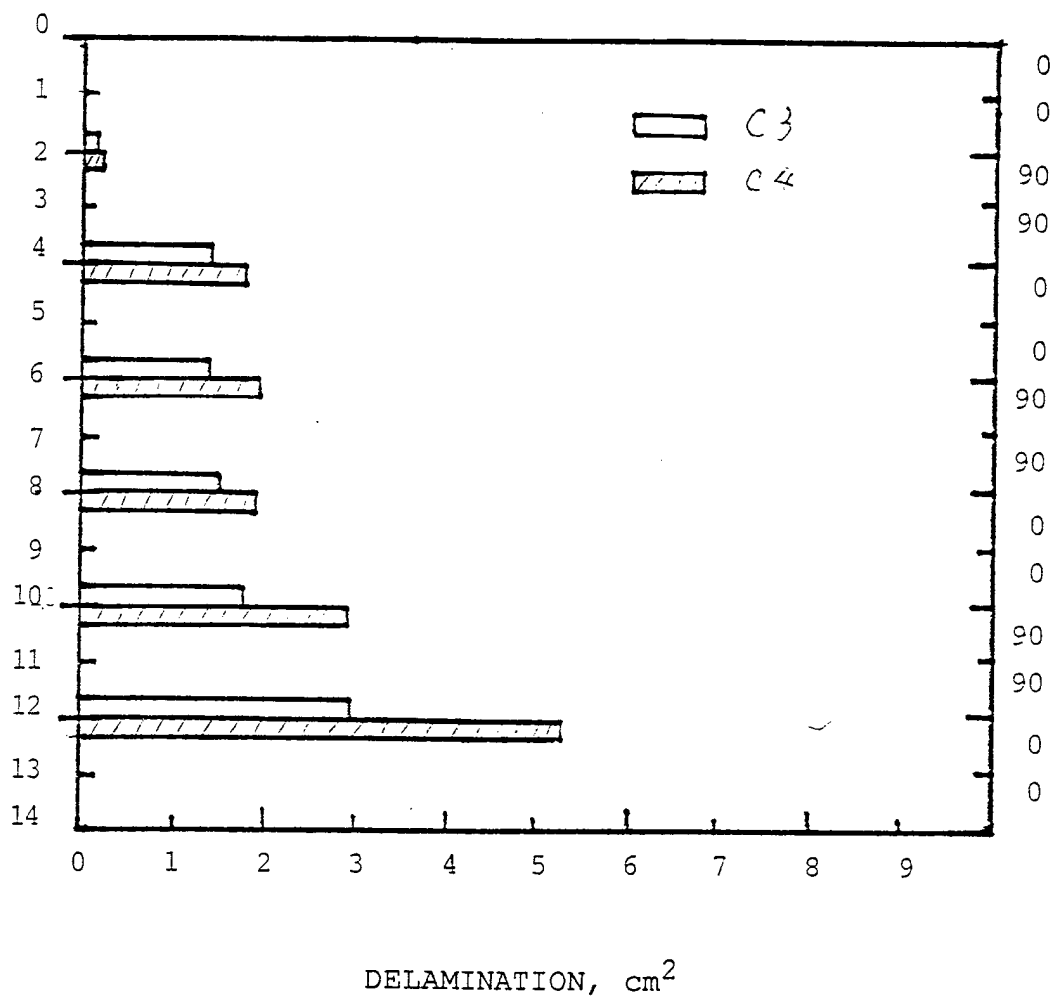
Fig. 11 Measured delaminations at laminated interfaces for Specimen C3 impacted with an energy of 8.81 ft-lb, and Specimen C4 impacted with an energy of 13.58 ft-lb. The total delamination areas for Specimen C3 and C4 are 9.10 cm^2 and 13.94 cm^2, respectively.
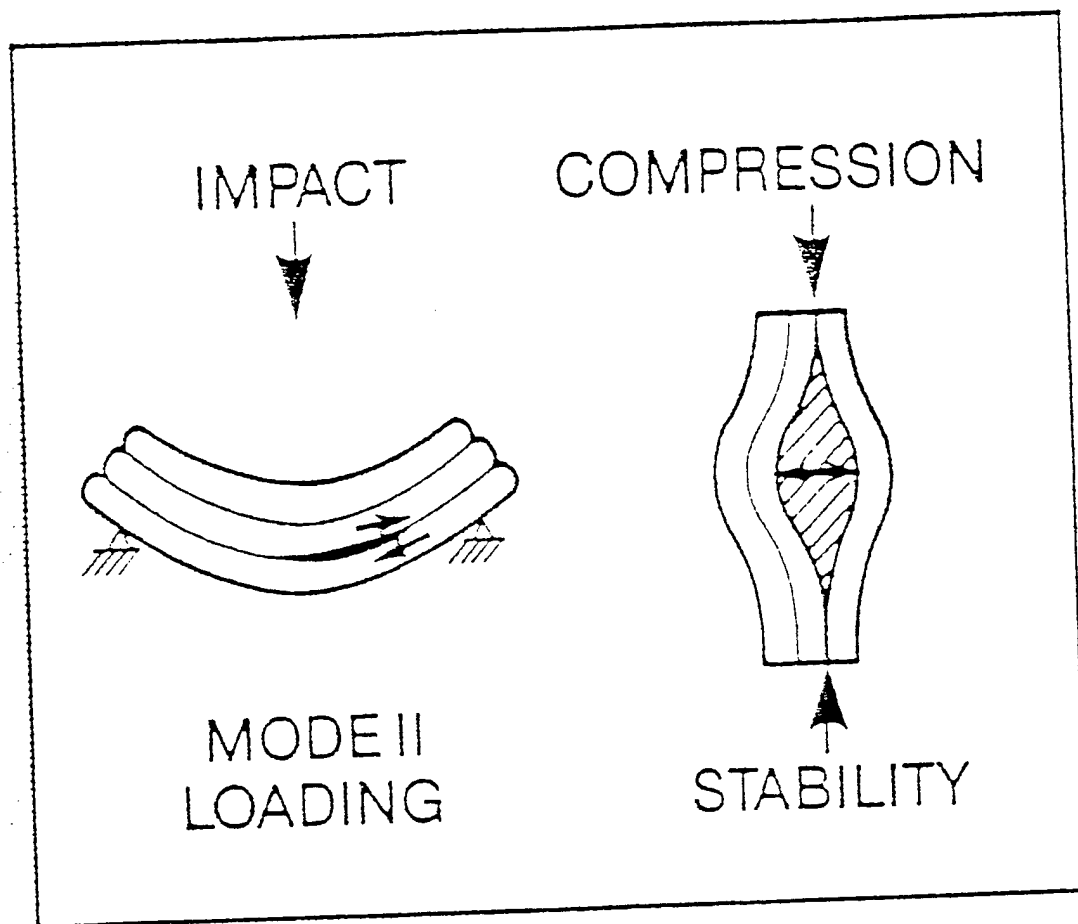
Fig. 12 Configuration of Compress-after-Impact strength test.

2.3 Stress Assessment in Glass Matrix Composites

Collaboration with NASA Lewis Research Center

A project collaborating with NASA-Lewis Research Center has been established to assess the stress states in Niclon fiber reinforced LAS matrix composites, for incrementing strain. Please note that since there is an agreement of confidentiality signed between Sonoscan and NASA, only the concept underlying the experiments and a brief results will be reported here. A more detailed description will be given upon the permission of Sonoscan and NASA, Lewis Research Center, Cleveland, Ohio.

The theories underlying the experiments have been described in previous chapter and the experimental procedure is described as following:

1. Place the specimen in the four point bending fixture as shown in Fig. 13.

2. Place the load cell (or strain gauge) in the fixture as indicated in Fig. 13 and connect the load cell wires to strain indicator.

3. Place the fixture with the specimen in a 30 MHz LPAV, operating in the interference mode, as shown in Fig. 14.

4. Optimize LPAV image so that the interference fringes clearly shown on the LPAV monitor.

5. Connect the oscilloscope to the video output of the LPAV and optimize the trace of the fringes inside the specimen on the scope.

6. Load the specimen by turning the loading screw clockwise until the strain indicator reads 5 microstrain.

7. Record the fringe shift that occurs due to the specimen loading.

8. Repeat steps 6 and 7 for an increment of 5 microstrain until a reading of 30 microstrain.

9. Unload the specimen and measure the fringe shift that occurs between this state and the original unloaded state.

Typical results are shown in Figure 15, displaying a series of pictures indicating the fringes shifts while the strain were increased from 0 (no load) to 30 microstrains, for a increment of 5. The stress can be calculated through the effect of acoustoelasticity, as described in previous chapter, and will be remain confidential here. In Phase II, a phase unwrapping algorithm included in RTSTRESS will be developed to calculate the stress.

Real-Time Imaging of Stress in Gruman's Aluminum Plate

A 0.5" thick Aluminum plate was received from Gruman Aerospace for the inspection of residual stresses resulting from different processes. The plate has two holes on it which have been drilled and reamed. One hole has been cold expanded prior to final reaming and is expected to contain compressive residual stresses around the hole, approximately one radius from the edge of the hole.

It was placed in a 10 MHz LPAV and the results were shown immediately as those displayed in Fig. 16. The image shown in Fig. 16 (a) is a hole resulting from normal process, while that shown in Fig. 16 (b) is a drilled hole which had been cold expanded prior to final reaming. As suggested by Gruman, the residual stresses around the hole of case (b) will be approximately one radius from the edge of hole. Reviewing the image of Fig. (b), one can easily find the shaded donut ring around the hole indicating the existence of compressive residual stresses which has attenuated the transmission of ultrasound.

Damage and Stress Assessment of Lockheed's Samples

Two pieces of S-Glass/Epoxy batten materials have been received from Lockheed Missile & Space Company, which would be used for Lockheed's Space Station solar array components. One was pultruded (as will be the final hardware) and the other compression molded from prepreg. Both have unidirectional fiber orientation.

Damage assessment of these samples were routine for LPAV and meaningful results have been achieved. However, the stress assessment will be a little more complicated and will be subject of the Phase II project. In the Phase II, we would like to assess the damage and stresses in the following states:

     (1) in the virgin state

     (2) at 1.5% buckling strain and
         some increments between zero and 1.5%

     (3) at 1.5% after intervals of time,
         e.g. 1 day, 7 days and 21 days.

The NDE method described in Section 4.2 with a hardware setup illustrated in Figure 19 of the same section will be used to perform the proposed experiments.
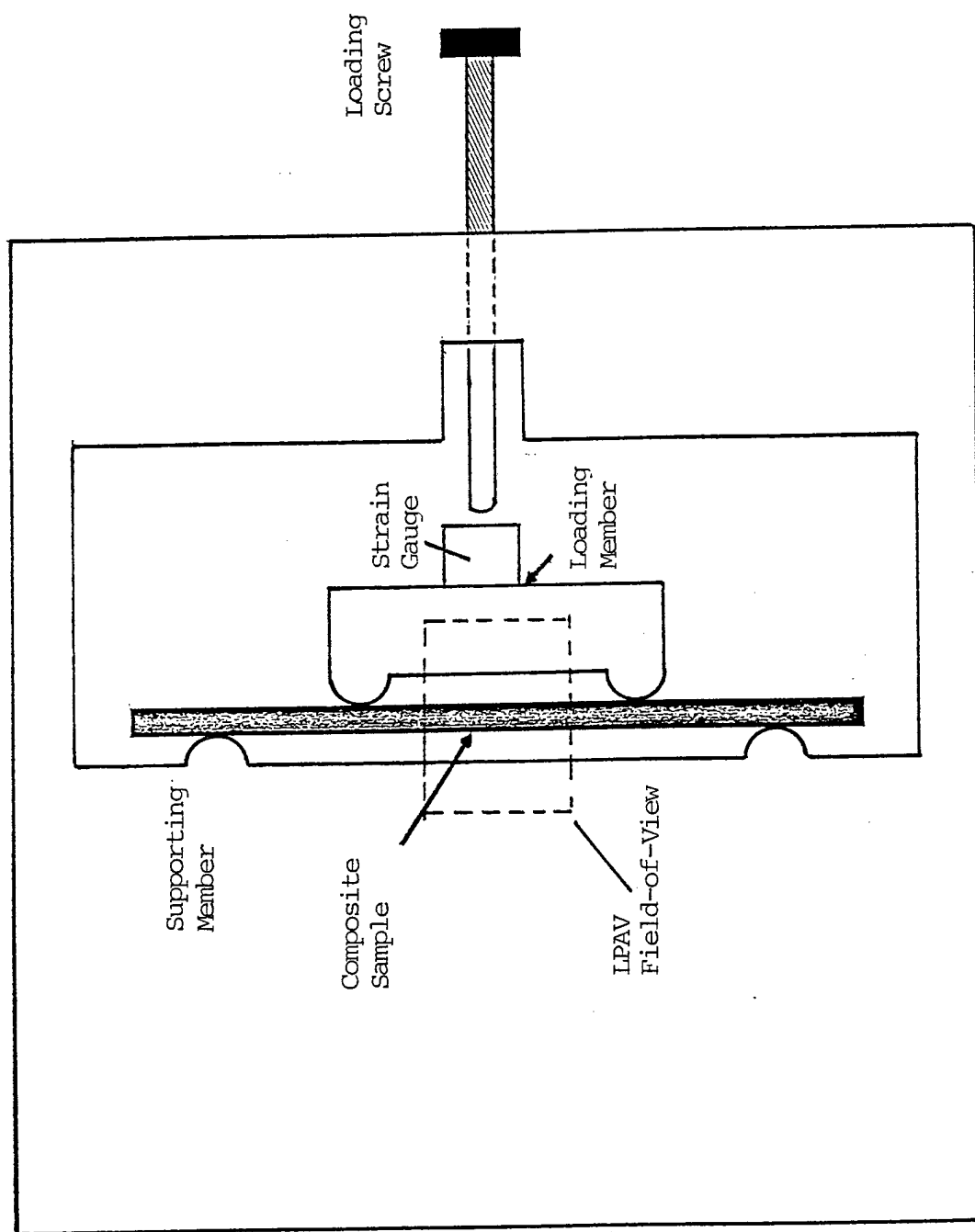
Figure 13. A four-point bend fixture used to apply strain to the sample, when monitored the stress by the LPAV operating in intererence mode.

Figure 14. Experimental set-up for stress monitoring, with a four-point
bend fixture in the LPAV, operating in interference mode.
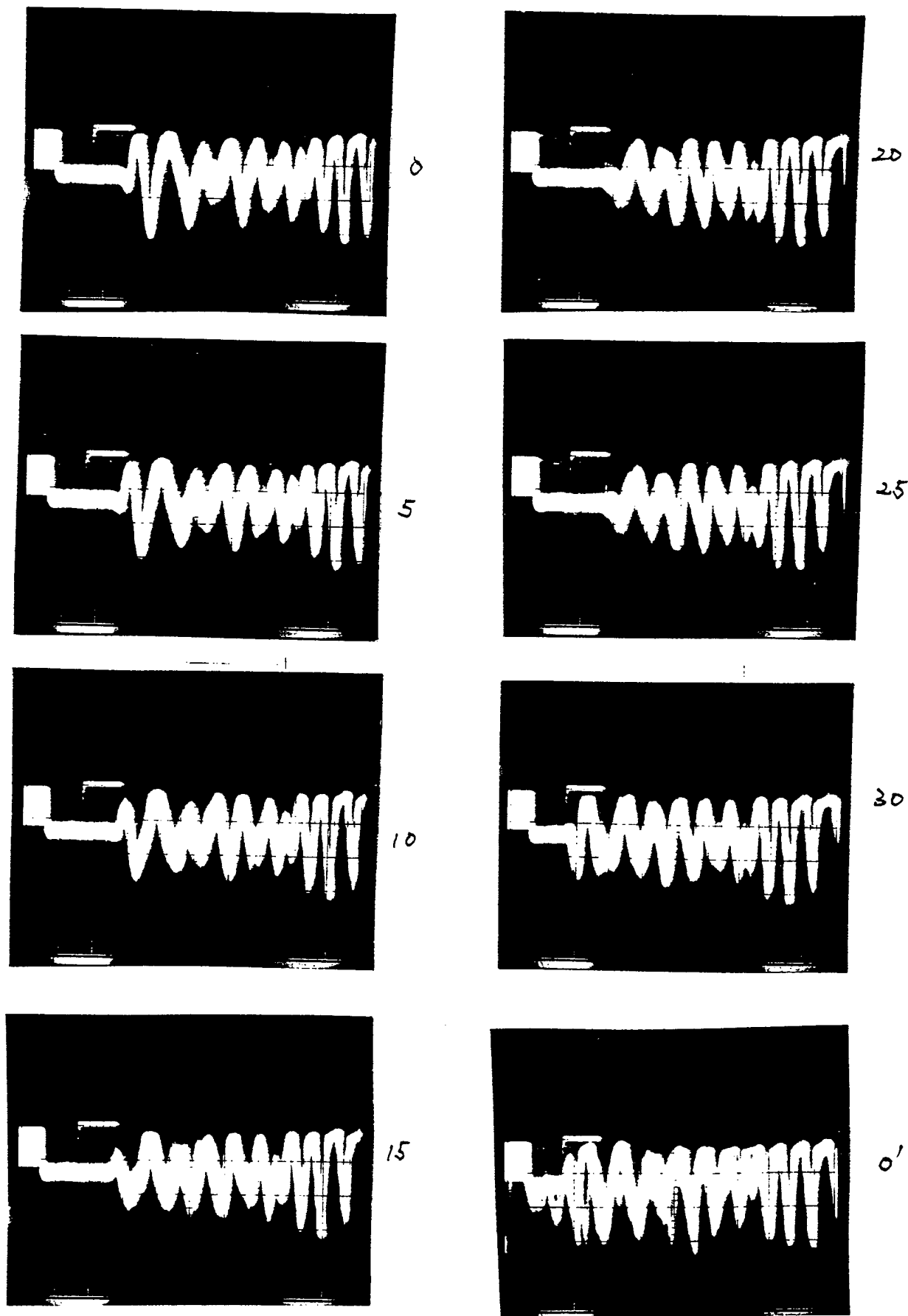
Figure 15. The interference fringes shown on the oscilloscope.
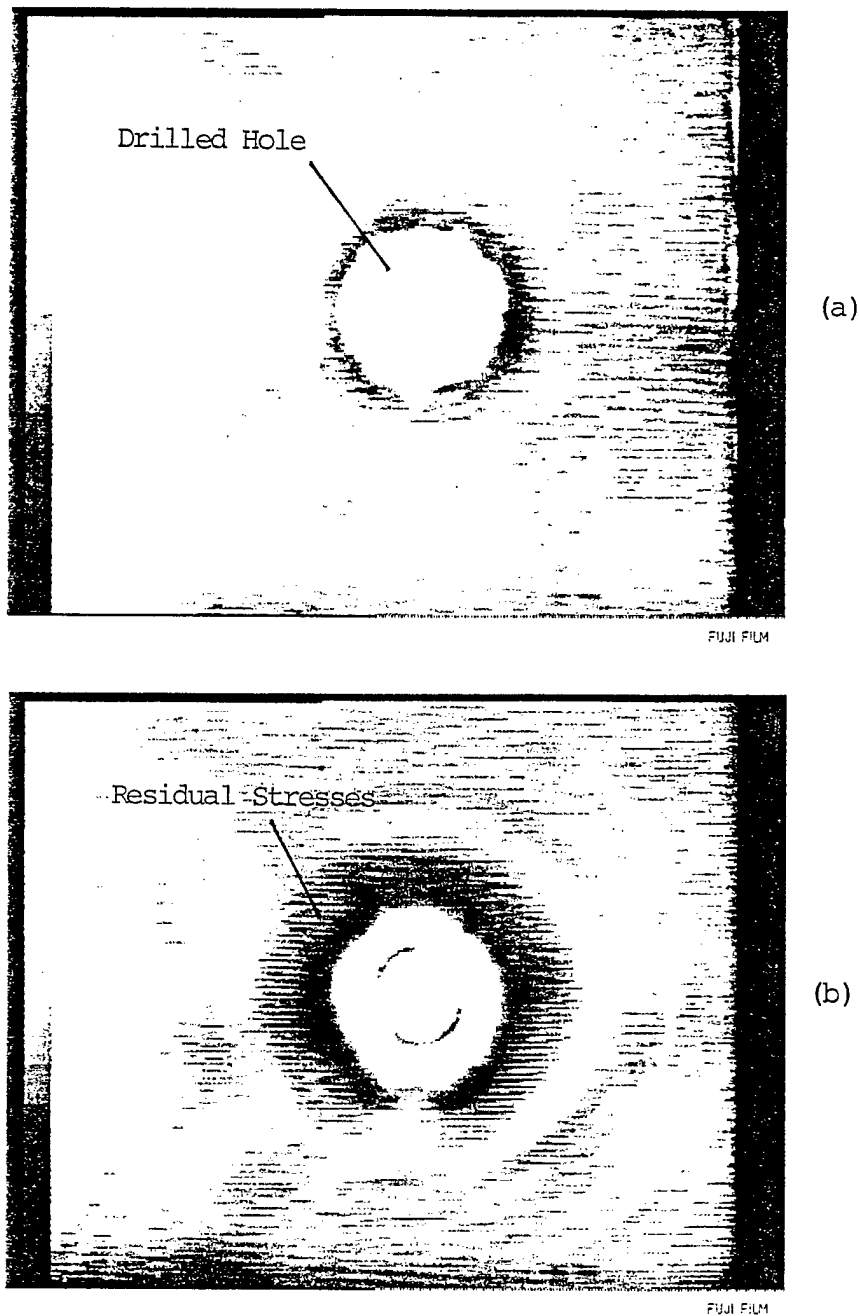
Figure 16. 10 MHz LPAV images showing (a) normal process, and (b) cold expanded prior to final reaming. Compressive stresses attenuates ultrasound transmission and can be found in the case 0f (b). The field-of-view is 35 mm by 26 mm.

2.4 Imaging of Disbonds

CSAM Imaging of Disbonds in Superconductor Rods

At the developmental stage in Phase I, a lab-use version of cylindrical CSAM system which had been developed in a completed SBIR contract sponsored by DOE (DE AC02-87-ER80453) was modified to perform 100 % area inspection of a sectioned NbTi alloy superconducting rod. We have demonstrated the capability of the proposed CSAM in MFRS in detecting and mapping out disbonds at the interface of a cylinder-in-cylinder, in this case the interface between a Cu clad cylinder and a NbTi core cylinder.

A HIPped billet of Cu clad-NbTi superconductor right after extrusion was employed here to demonstrating the detection of disbonds in the joining of cylinder-in-cylinder. The sample diameter was 0.800" (or about 2 cm). The sample was composed of a Cu clad cylinder with a 0.8" O.D. (outer diameter) and 0.72" I.D. (inner diameter) embracing a 0.72" NbTi core.

A 30 MHz transducer with a 0.25" aperture and 1.25" focal length was used in order to physically focus the ultrasound beam onto the interface between Cu clad and NbTi core which was about 0.09" below the rod surface. The beam waist of the focused ultrasound at the Cu-NbTi interface was calculated to be approximately 300 um.

Fig. 17 displays a cylindrical CSAM image of a scan of 3" long and 360° circumference, in which a horizontal white stripe (or red in the original color print) approximately at the center of the image represents a disbonded area in the test rod. Fig. 18 illustrates a 3X magnified view of the disbonded area, providing a field of view 1" long and 120° circumference.

To provide supporting evidence, the sample was later sectioned, polished adequately and view under an optical microscope. The result from optical inspection agrees very well with that from CSAM imaging. The circumferential width of the disbonds was measured to be around 2 mm both optically or ultrasonically.

LPAV Evaluation of Disbonds (Cornell University Project)

Several samples were received from Cornell University, (Ithaca, New York) to evaluate the bonding agents and processes to bond a 2-111R ferrite to a stainless steel tube (410SS). The bonding agent was a silver-loaded ceramic glue (proprietary). Agreement of Confidentiality was signed and most of the evaluation results remain confidential. The experimental set up is illustrated in Fig. 19, and typical results are shown in Fig. 20.

Fig. 20 (a) display a 10 MHz LPAV image, showing porosity and residual stress in the boding agent which have resulted from a experimental bonding process. In contrast, Fig. 20 (b) indicates a good bond.
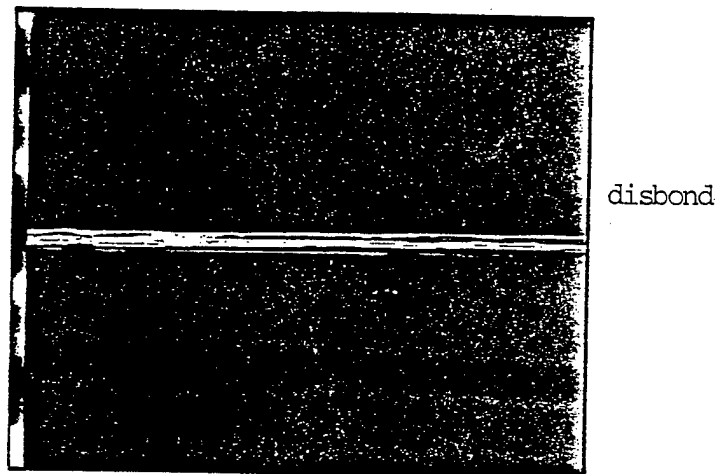
disbond

Fig. 17. A C-SAM image showing disbonds at Cu/NbTi
interface. A 30 MHz transducer (F number 5) was
used. The scan size is 1" along the length by 360°
rotation of rod. The dark background indicates
areas of good bond interface, while the colored
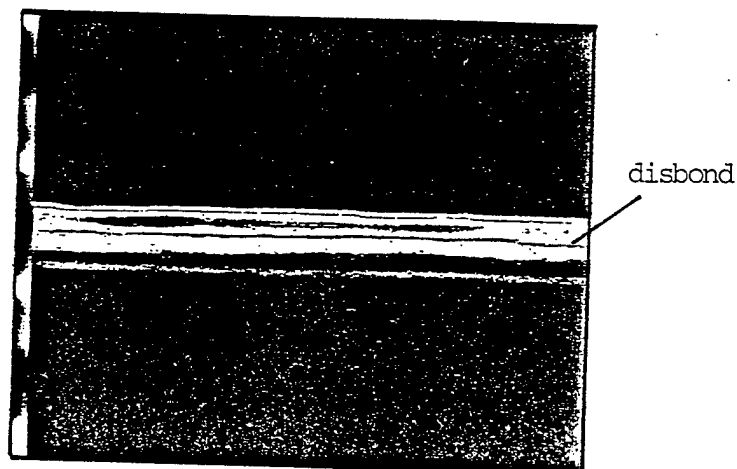areas show disbonded interface.

disbond

Fig. 18 A 4 x magnified view of above image. The
scan size here is 0.25" by 90°. It clearly shows
two seperate strips of disbonded area. The total
length of the disbond is estimated to be 2 mm.

(reroxed from a color print)
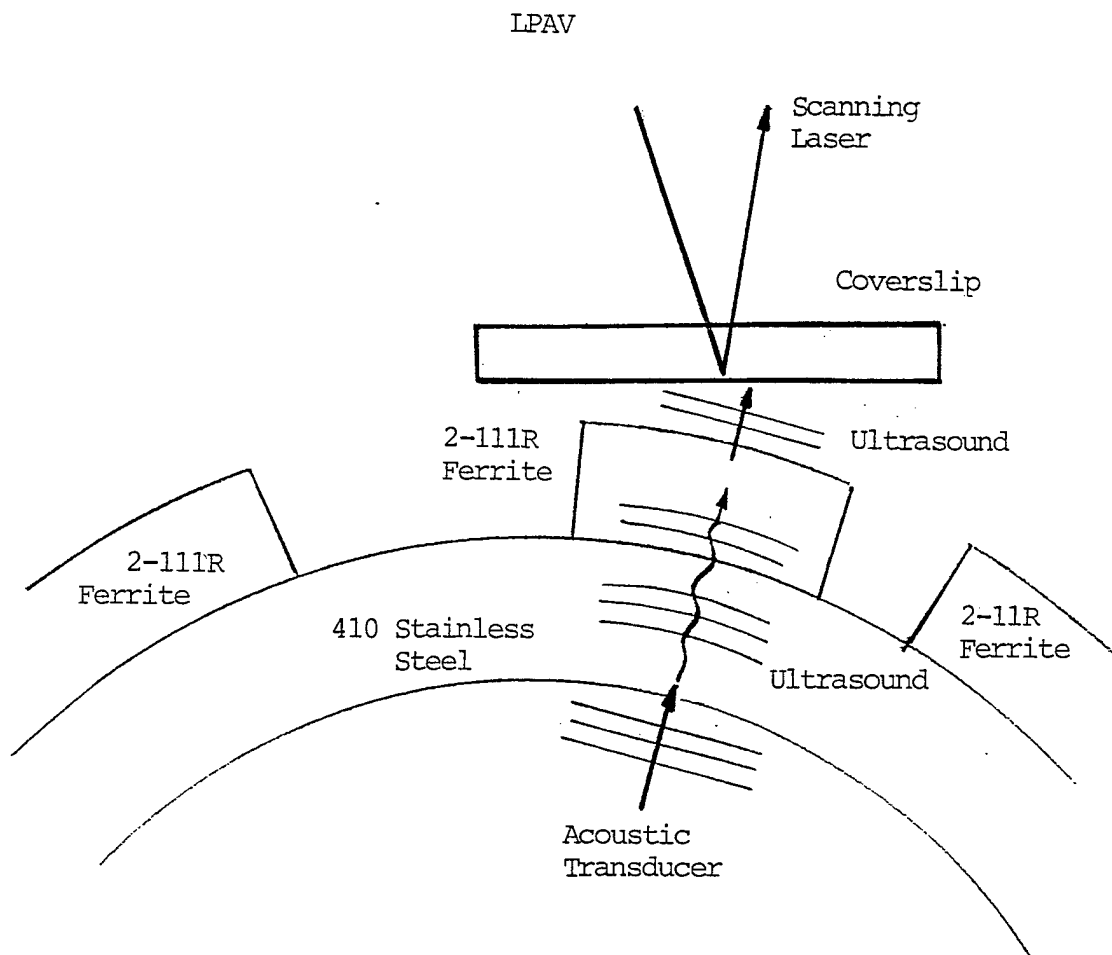
LPAV

Figure 19.   Evaluation of bonding between the ferrite and
             stainless steel tube.

Residual
Stress

Disbond

SAMPLE 5

FUJI FILM
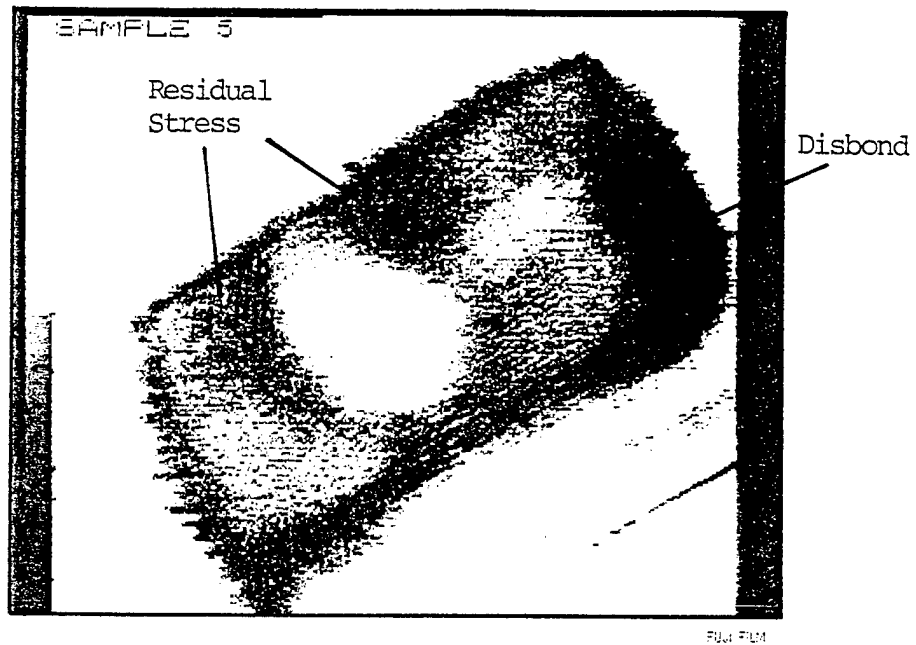
(a) Disbond and residual stress resulted from
     a experimental bonding process.

SAMPLE 3

FUJI FILM
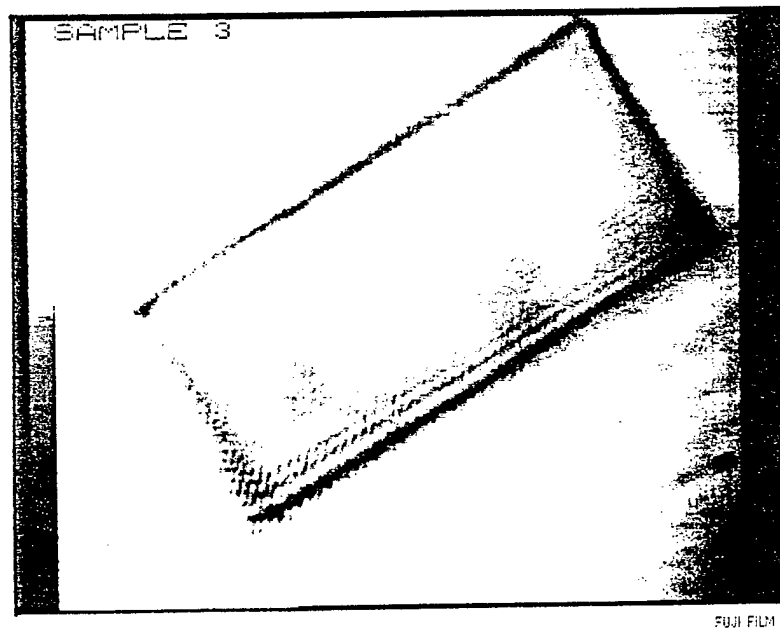
(b) Good bonding quality.

Fig. 20. LPAV images showing (a) residual stresses in bonding agent
          resulted from an experimental process, while (b) a good
          boning between ferrite and stainless steel.

CSAM Inspection of Disbonds in Honeycomb Laminates

Several honeycomb laminate panels have been received from Boing - Kent Space Center (Kent, Washington) for inspection the bonding between the laminate layers, and between the laminates and the honeycomb. The samples had woven glass/phenolic skins and aluminum core.

A CSAM with a 15 MHz transducer having 0.5" diameter and 0.75" focal length was used to inspect the honeycomb laminate samples. The ultrasound was focused to the interface between the laminate and the honeycomb, which was 1.6 mm, or the thickness of the laminate skin, below the surface.

The color bar at the leftmost of the image represents the amplitudes of return echoes. The dark color center of the bar indicating zero in amplitude means there is no return echo detected in the area well bonded. A representative well bonded honeycomb is highlighted with solid line hexagon, while a partially bonded honeycomb is dashed.

CSAM provides an effective way in evaluating the bond quality and an NDE method predicting the strength of such honeycomb laminates can be derived on the basis of CSAM in MFRS.

15 MHz CSAM Image of Honeycomb Laminate Panel
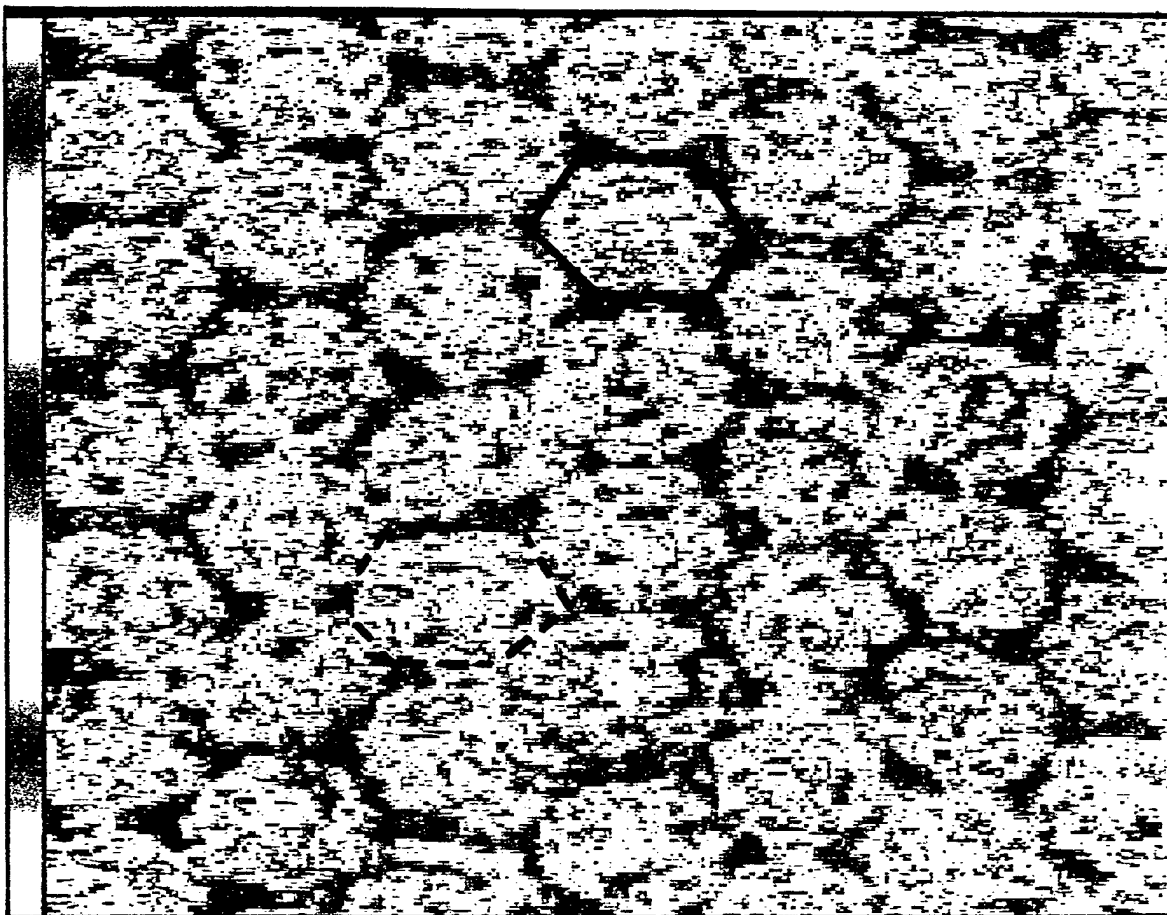
Fig. 21.   A CSAM image, made by a 15 MHz transducer with 0.5" dia. and
           0.75" focal length, showing the bonding of a honeycomb laminate
           panel. This image was produced at a specific level, 1.6 mm
           below the surface. The scan size was 28.6 mm by 26.8 mm. The
           solid hexagon indicates a good bond while the dashed hexagon a
           partially bonded.

(copied from a color print)

2.5 NDE of Metal Matrix Composites

Samples from Naval Surface Warfare Center

Two batches of Gr/Al MMC (metal matrix composite) samples were received from NSWC (Silver Spring, Maryland) fro inspection. The first set contained two small plates cut from a retired panel. One was suspected delaminated. They were inspected by LPAV and the difference between the two samples were shown immediately (Fig. 22). A 10 MHz LPAV image of the sample considered to be normal is shown in Fig. 22 (a), displaying some fiber debonding from the matrix. The LPAV image of the sample suspected to be delaminated, shown in Fig. 22 (b), displays a partially delaminated area to the left of the sample. The results fall in expectation.

The other set of samples contained three dome-like Gr/Al MMC disks. A 10 MHz LPAV was used to map the delamination areas in the samples. Typical results are shown in Fig. 23 for the sample numbered 3492. The samples were fully inspected by the LPAV and the results were recorded by a VCR. Four of the LPAV images are shown in Fig. 23. At the center of the figure, a map showing the locations and areas where the LPAV images were taken. In each LPAV images the dark areas indicate the existence of delaminations. Most area of the sample is found delaminated, as shown shaded in the map.

Sample from University of Illinois at Chicago

A Gr/Al MMC plate was submitted by Professor Bosis, Department of Material Science, University of Illinois at Chicago, for NDE. The sample had a notch on it to guide the damage development while applying stress through a four point bending. The experimental set up is schematically illustrated in Fig. 24, along with a 10 MHz LPAV image showing the damage around the notch. The field-of-view for 10 MHz LPAV is 35 mm by 26 mm. In the LPAV image, the dark area around the tip of the notch displays delamination resulting from bending stress. LPAV will be a suitable candidate for real-time monitoring the development of damage in MMC while applying stress to the sample.
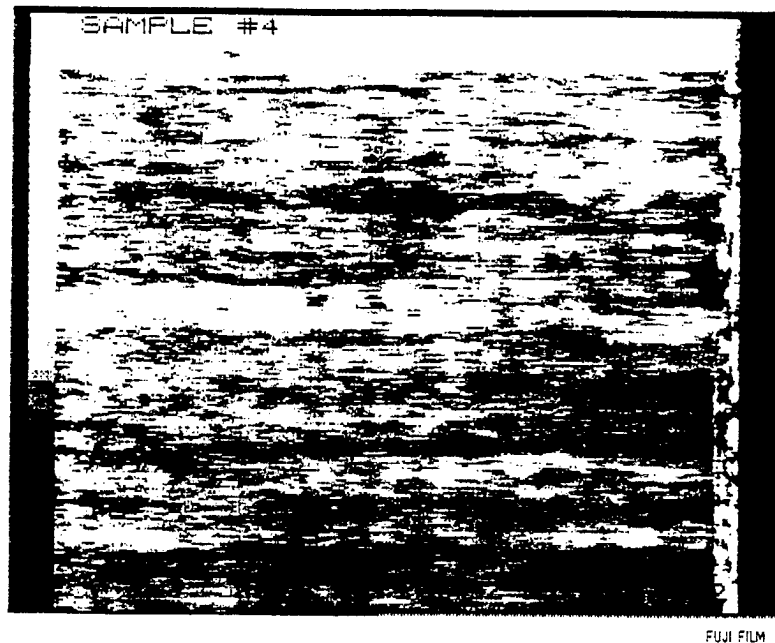
(a)   MMC sample with fiber debonding from the matrix.
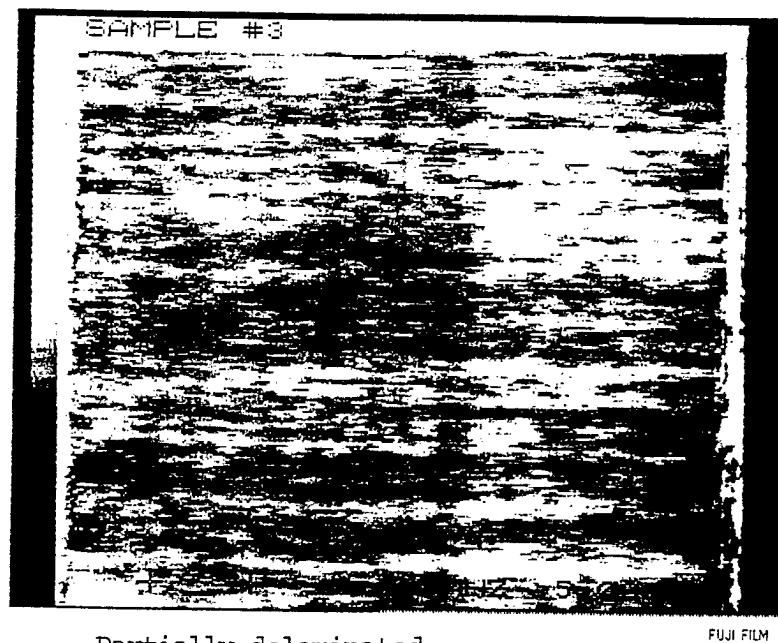
Partially delaminated

(b) MMC sample showing partially delaminated at the
     left half of the sample.

Fig. 22.   10 MHz LPAV images demonstrating real-time evaluation of
           Gr/Al MMC samples, (a) showing fiber debonding from the
           matrix and (b) showing a partially delaminated area.   The
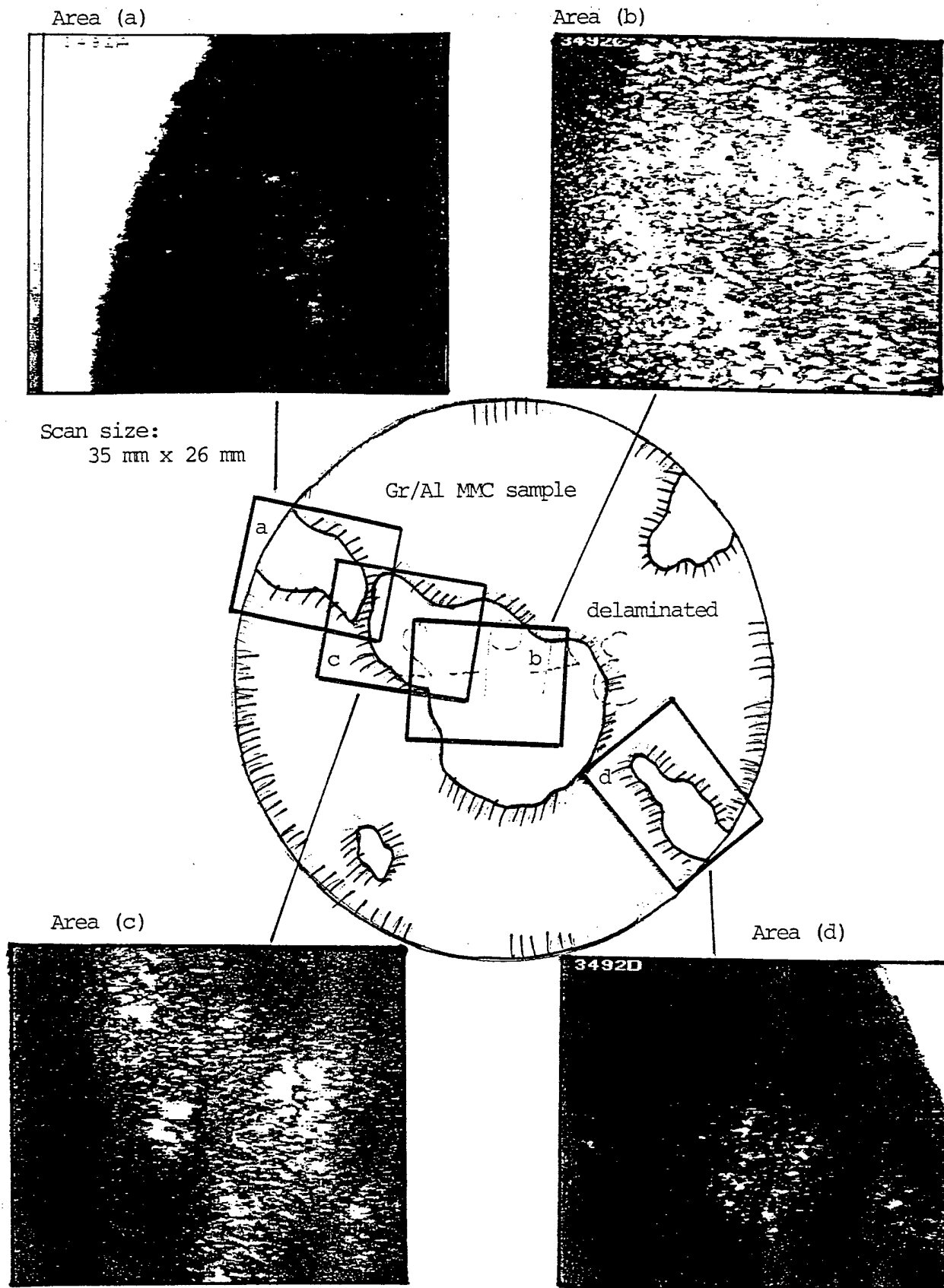   field-of-view is 35 mm x 26 mm.

Area (a)

Area (b)

Scan size:
35 mm x 26 mm

Gr/Al MMC sample

delaminated

Area (c)

Area (d)

Fig. 23. 10 MHz LPAV images mapping out the delaminated areas in a Gr/Al
MMC disc. The scan size is 35 mm by 26 mm.
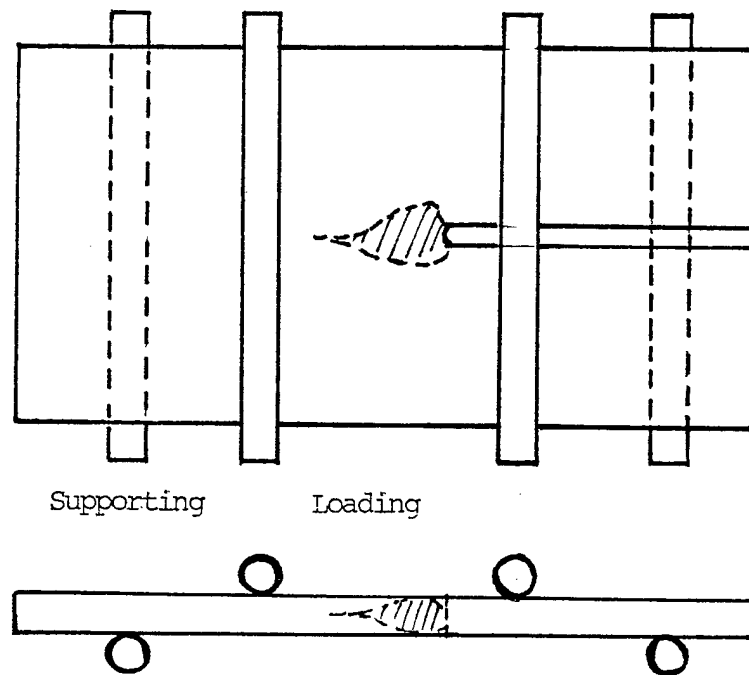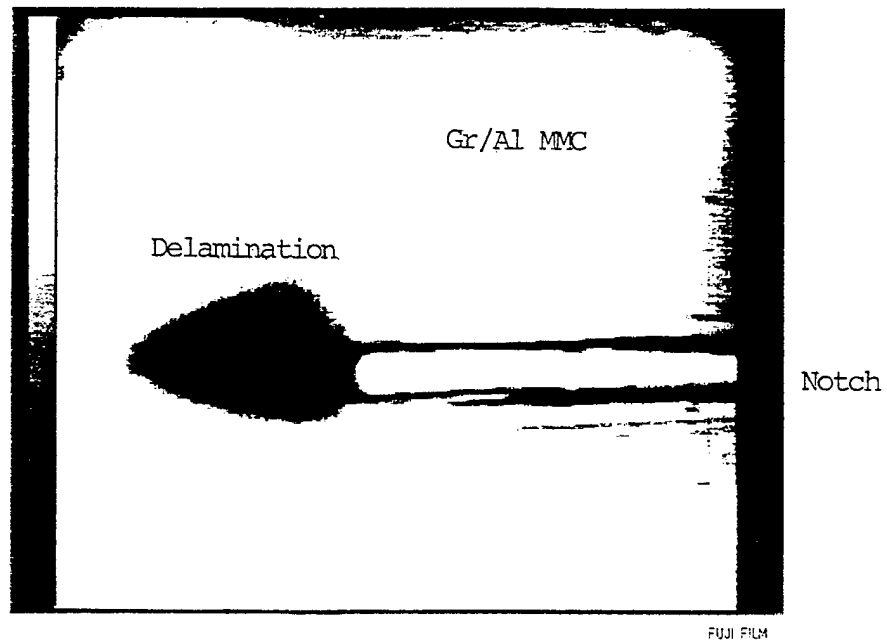
Fig. 24. 10 MHz LPAV image showing delamination developing in a Gr/Al MMC sample around the notch, which has been subjected to four-point bending as shown in the figure.

2.6 NDI of Composite Components

NDI of Undocted Fan Blade

An undocted fan blade developed by NASA was inspected using the proposed LPAV. The conceptual drawing of the inspection set up is illustrated in Fig. 25. The LPAV can rapidly and effectively find defects such as voids, inclusions and delaminations in the composite parts. A 10 MHz LPAV was used to inspect a miniatured fan blade provided by G.E.. The results are presented in Fig. 26. Some fiber debonding from the matrix could be found. several inclusions were detected. In general the bonding of the blade to the metal shaft was good.

Aspects of On-Line Inspection

A number of composite materials and components were received from Cherry Textron Aerospace Fastening Systems, (Santa Ana, California). Since a confidentiality agreement was singed and little information could be presented here. The results underlying the aspects of using LPAV for on-line inspection is displayed in Fig. 27. Samples A's were suspected by the manufacturer to have delamination and they did show on the LPAV image, Fig. 27 (a). In contrast, Samples B's displayed partial delamination and were acceptable. The Sample D was suggested by Cherry Textron to be acceptable, while Sample I might be porous. The results shown in Fig. 27 (b) agrees with manufacturer's expectation.

NDE of Delaminations Around Fastener Hole

Several commercial available composite coupons with fastener holes were acquired for inspection. Fig. 28. displays typical LPAV images, clearly showing the delaminations associated with the fastener holes. The LPAV provides a mean to determine the edge distance requirements for installation of fastener holes in newly manufactured and repaired advance composites panels. A series of 10 MHz LPAV images composing a complete acoustic image of an as-manufactured composite coupon are presented in Fig. 29, demonstrating the concepts of using LPAV as a QC tool in manufacture of advance composites panels.

NDI of Fusion Welds

Several PHMR-end to sheath resistance welded zinc alloy samples were submitted by Bhabha Atomic Research Center (Trombay, Bombay, India), for inspection of the weld quality. The results are displayed in Fig. 30 and 31 for good and bad welds, respectively. Confidentiality agreement was signed and little information could be revealed here.

Evaluate bonding quality
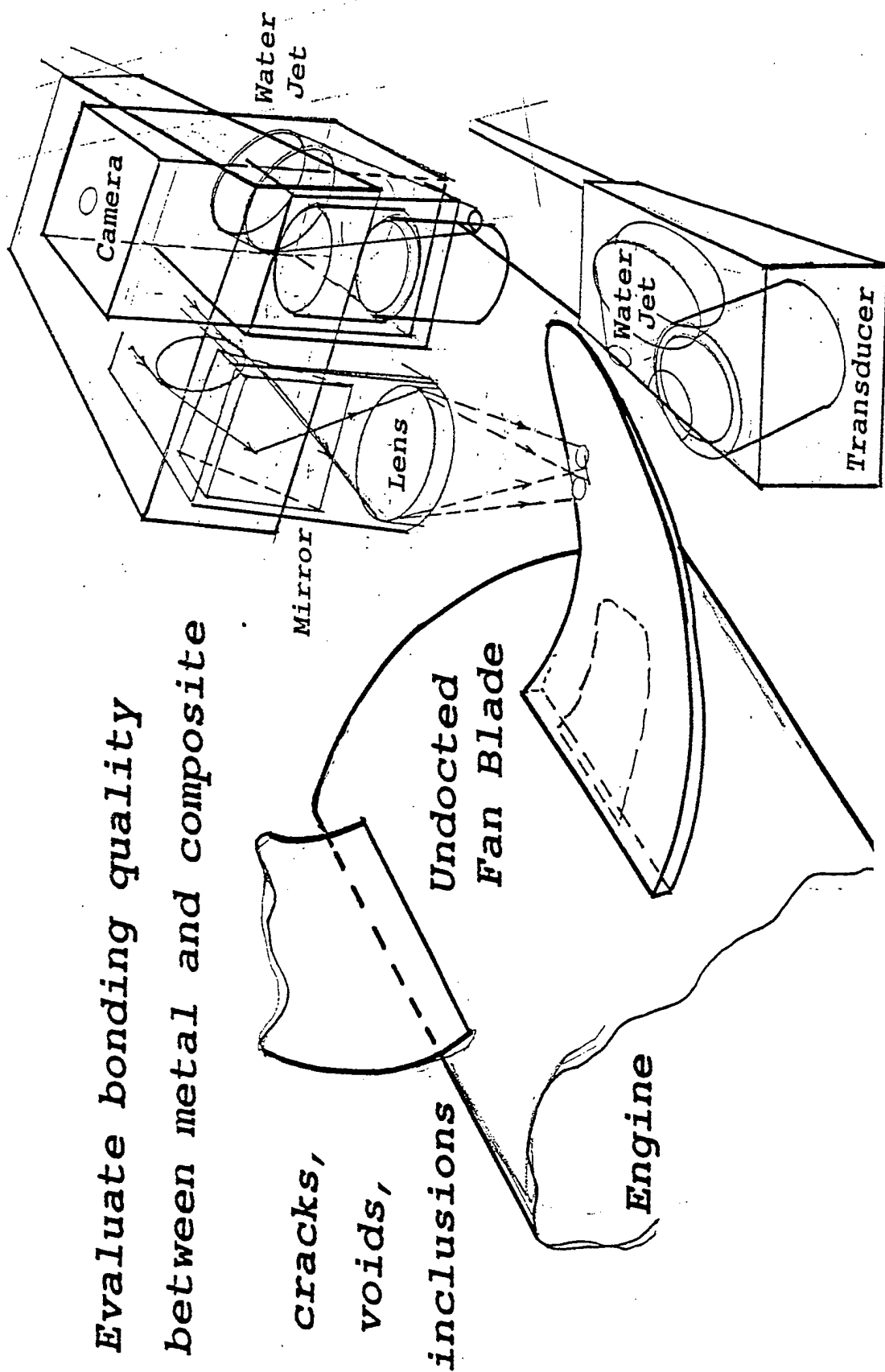between metal and composite

cracks,
voids,
inclusions

Camera

Water
Jet

Mirror

Lens

Water
Jet

Transducer

Undocted
Fan Blade

Engine

Fig. 25.   Conceptual drawing of experimental set up using the LPAV of MFRS to inspect an undocted fan blade in jet engine. (project with G.E.)
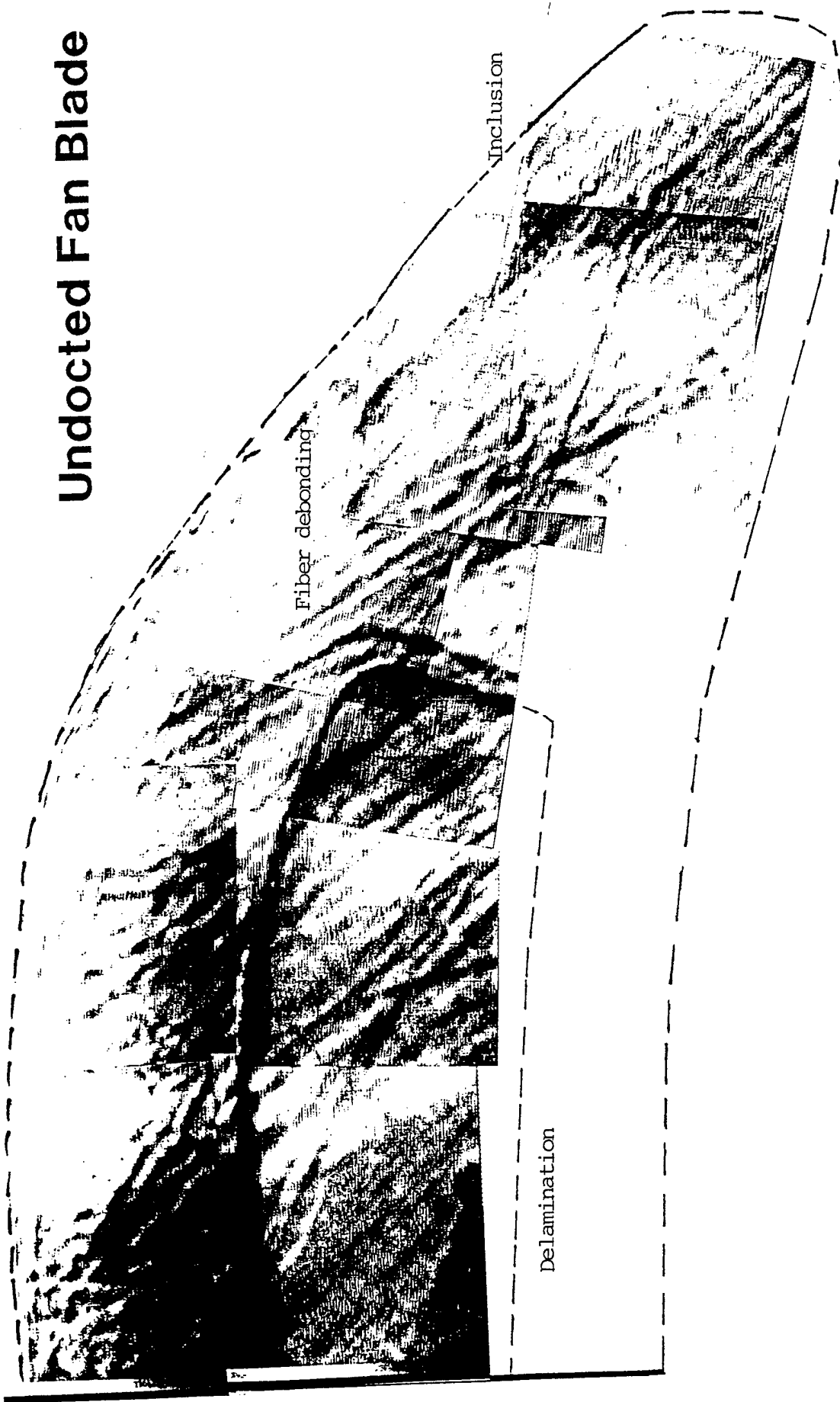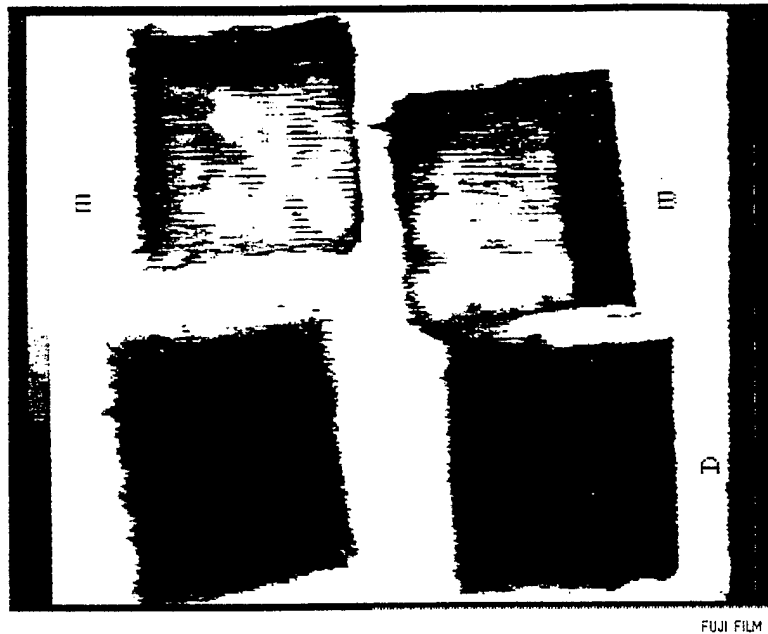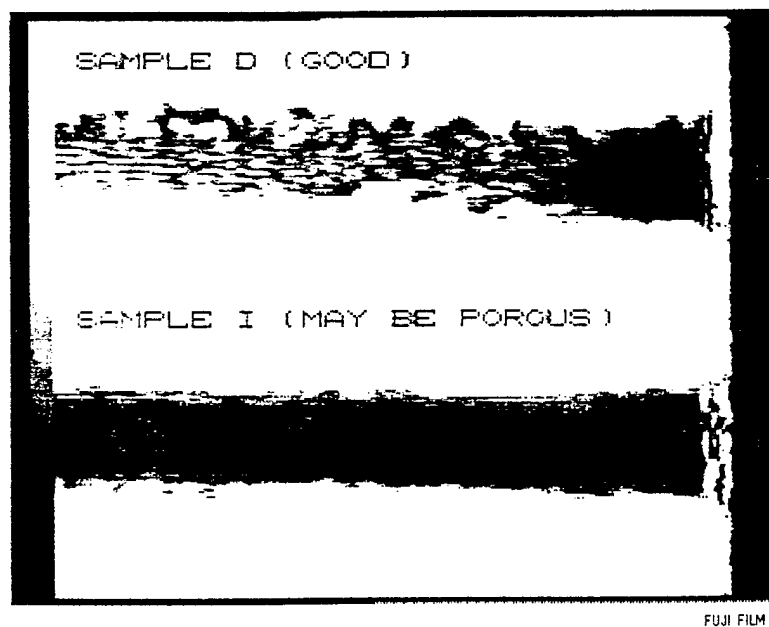
Undocted Fan Blade

Fig. 26. 10 MHz LPAV images showing the inspection results of the undocted fan blade. Some fiber debonding from the matrix can be seen.
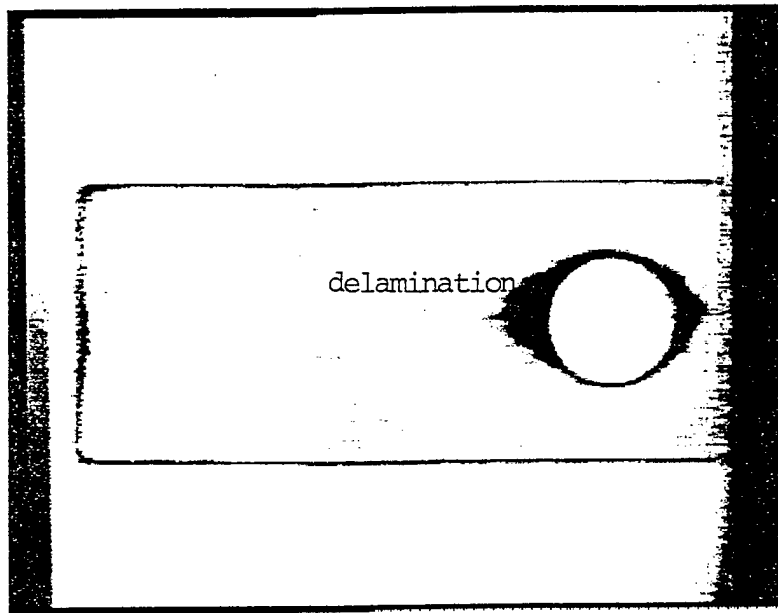
(a) PMR15 carbon fiber reinforced panel cupons.
Samples A's are completely delaminated, while
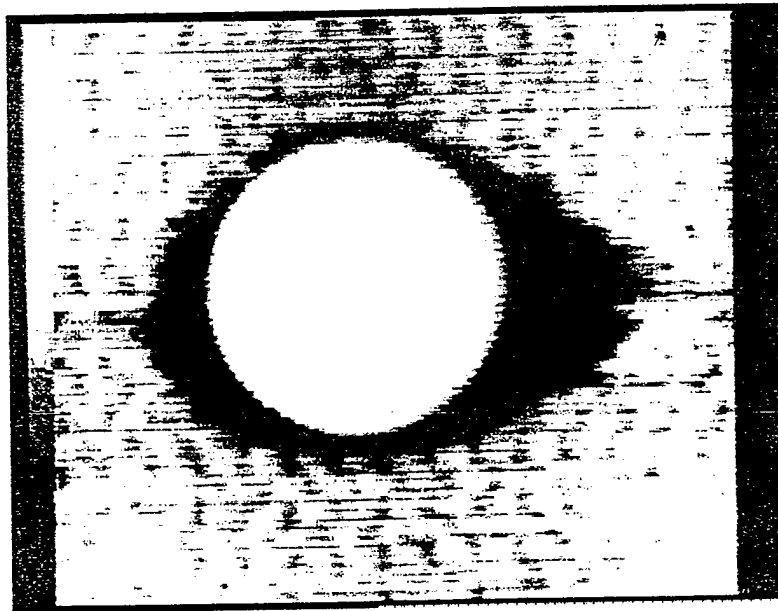Samples B's partially delaminated.

(b) PEEK, carbon fiber reinforced threaded shear
pins. Sample D is good when Sample I is porous.

Fig. 27. 10 MHz LPAV inspection of composite samples, demonstrating
aspects of on-line inspection of components using LPAV.

(a)

(b)

Fig. 28. NDE of delamination around the fastener hole on composites.
(a) 10 MHz LPAV image, 3.5 cm by 2.6 cm, and (b) 30 MHz LPAV
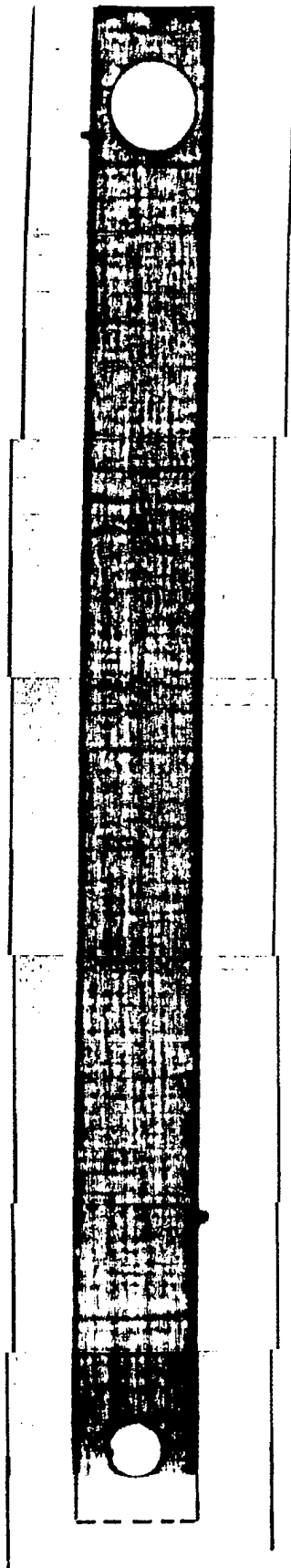image, 14 mm by 10 mm.

61

Fig. 29. 10 MHz LPAV images showing defects of a Gr/Epoxy composite coupon as manufactured, demonstrating the concept of using LPAV as a QC tool.
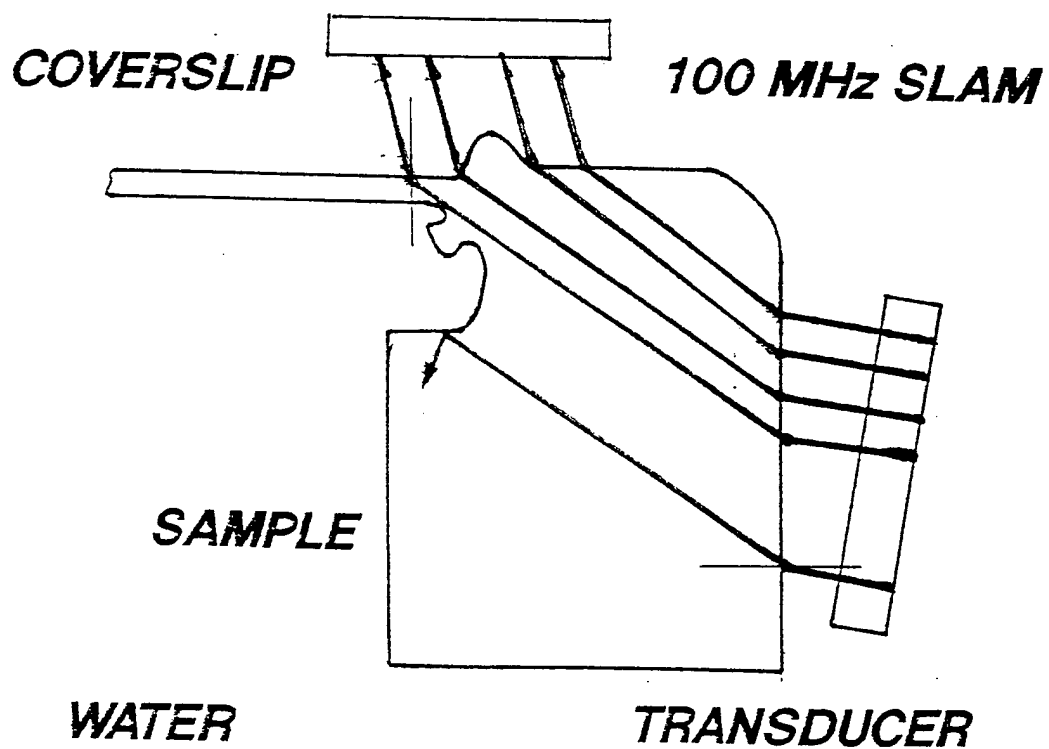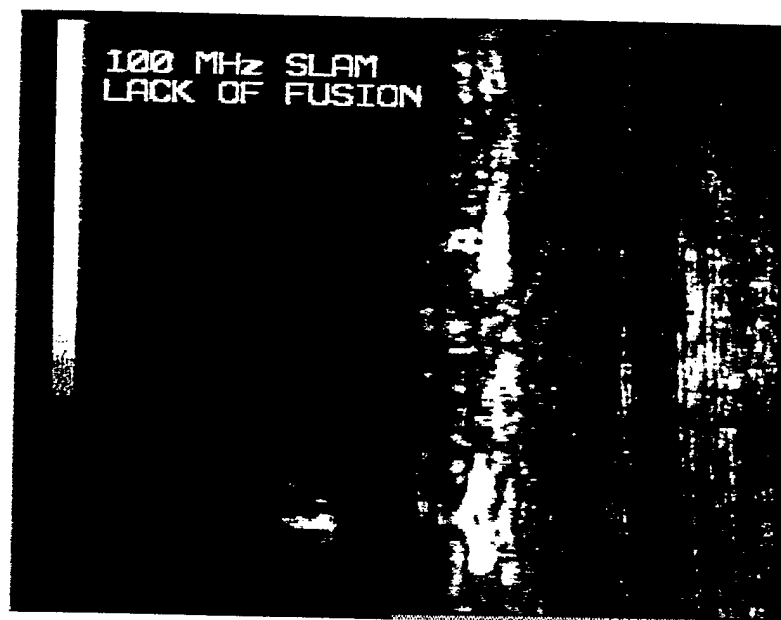
GOOD WELD

Fig. 30. LPAV 100 MHz image displaying a good weld case.
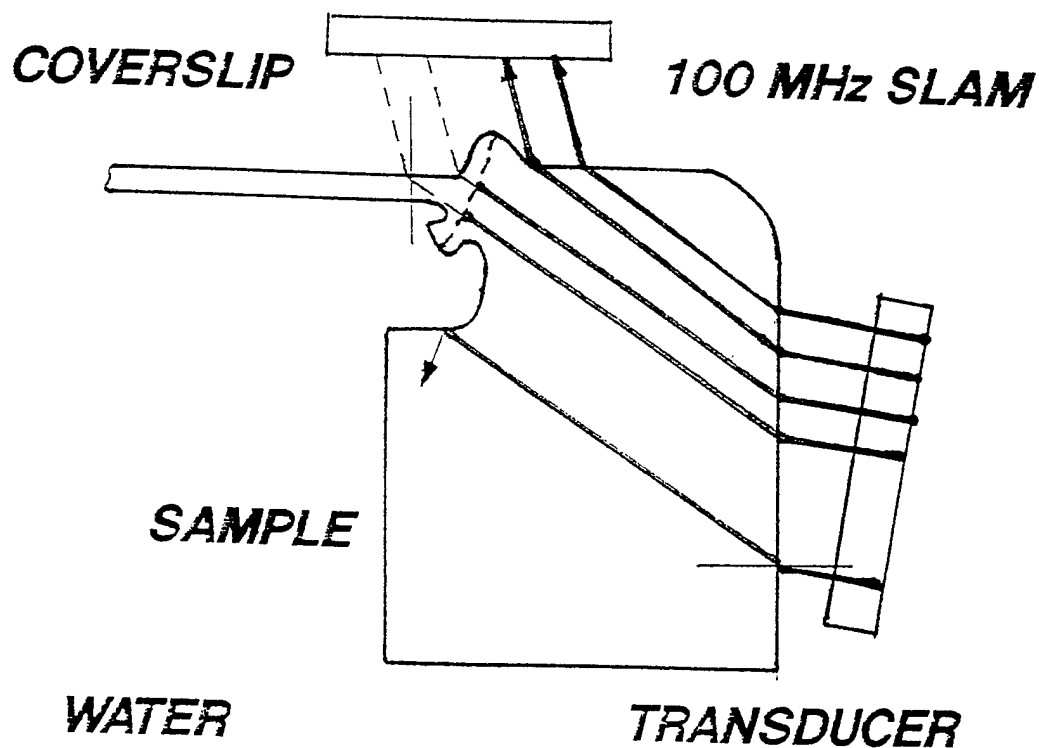
LACK OF FUSION

Fig. 31.   100 MHz LPAV image dhowing a lack of fusion case.

3. DESIGN AND OPERATION OF MFRS

The objective of this Phase II project is to develop a working prototype Multi-Function Robotic Sonoscope (MFRS) which is capable of real-time detection, imaging and characterization of flaws or integrity-reducing anomalies in structural materials and components.

Modules which will be developed with MFRS include the Scanning Laser Microscope (SLM), Laser Probing Acoustic Vision (LPAV), C-mode Scanning Acoustic Microscope (CSAM), and Scanning Acoustic Pulse Spectroscope (SAPS). All functions can be incorporated into MFRS simultaneously or separately, primarily depending on applications. Although modular in design for ease of repair and upgrading, the MFRS' many subcomponents will work in harmony under the guidance of a computer control system.

This chapter outlines the design concepts for MFRS and describes detailed design parameters and guidelines for modules to be developed and implemented in Phase II. These modules are designed in such a way that they can be incorporated into MFRS at any time as required without major change of the host MFRS system.

To demonstrate the usefulness and the ease of upgrading of MFRS, but without loss of generality, we shall develop three NDE methods and the associated computer algorithms for applications suggested by the aerospace industry. The specific computer algorithms to be developed in the Phase II are 3DIMPACT, CYLJOIN and RTSTRESS.

3DIMPACT quantitatively measures impact damage and predicts the CAI strength of the impacted specimens, which is critically important in application of the materials in structural design. CYLJOIN quantifies porosity content in cylinder-in-cylinder joining, which may be applied to the ongoing Air Force and SDIO Joining Project at Boing or the Two Phase Survival Thermal Management (TSTM) project at Lockheed. RTSTRESS evaluates the stress state of the test specimen and can be applied to stress assessment of materials such as are used in Lockheed's Space Station Solar Array Components Project. The theories and analytical models underlying these NDE methods are detailed in next chapter.

3.1 MFRS System Design Guidelines

A prototype Multi-Function Robotic Sonoscope (MFRS), incorporating modules of Scanning Laser Microscope (SLM), Laser Probing Acoustic Vision (LPAV), C-mode Scanning Acoustic Microscope (CSAM), and Scanning Acoustic Pulse Spectroscope (SAPS) in a six-axis robotic arm will be developed in Phase II.

The innovation of MFRS system over the counterparts of conventional NDE instruments include the development of a dexterous robot host system and various NDE modules, regardless of the associated new NDE methods. The six-axis robotic arm, as shown in Fig. 1, provides the freedom to track the contours of complex shape components and to reach into confined spaces, and also provide housing for SLM, LPAV, CSAM and SAPS hardware.

Having researched robotics technology available for this project in Phase I, we think a six-axis robotic arm will be more than sufficient in providing necessary freedom for most of applications (see Fig. 1). To demonstrate the flexibility of MFRS, we will, however, develop a simpler MFRS system with 3-axis of translation and 3-axis of rotation, without loss of generality (see Fig. 2).

The six-axis robotic arm can be easily customized to incorporate all or some of SLM, LPAV, CSAM and SAPS modules simultaneously or separately, depending upon requirements of applications. Each module will be designed, developed and tested before being incorporated into the final MFRS. The basic modular designs include the following:

3.2 Six-Axis Robotic Arm

As MFRS is designed to be a general purpose NDE tool, it can be configured in many ways, primarily depending on applications. The basis of MFRS is a multi-axis robotic arm which provides the freedom to track the contours of complex shape components. Having investigated the available technology, we think the robot that has been developed through a NASA sponsored SBIR contract with Scientific Research Associates can be modified and used in this project (see Fig. 3). Another alternative will be to team up with other company such as Prime Robots, Inc. to develop our own model. The robotic arm should provide an internal passage for cables, optics and hoses. Water jets are used here to provide water coupling of ultrasound to test specimens.

A pair of robotic arms are required by LPAV and through transmission mode CSAM and SAPS functions. One arm accommodates all optics, cables and hoses, while the other accommodates only cables and hoses for acoustic transducer. The implementation of latter could be either the same as or a much simpler design (less degree of freedom) than that of the former. Each of the two arms can be operated separately and independently for CSAM and SAPS functions. However, when operated in LPAV or through-transmission CSAM mode, the coordination of those two arms is important and will be included in System Control program.

3.3 SLM (Scanning Laser Microscope)

An SLM module which has been incorporated in the robot arm is shown in Fig. 4. SLM consists with Scanning Laser Module and Optical Module. The Scanning Laser module is composed of a diode laser, scanning mechanism and optics needed to manipulate laser beam, as shown in Fig. 5. There are two schemes considered for the scanning mechanism. One includes a combination of multi-facet mirrors and galvo mirror to produce a 2-D scan. The other uses an acousto-optical deflector instead of multi-facet rotating mirror.

The optical module as shown in Figure 4 is composed of several pairs of lenses which will be selected according to various resolution and field-of-view requirements. It is very important to note that SLM shares optics with LPAV. To design a proper optical system for both SLM and LPAV we need to consider the interaction efficiency between optical and ultrasonic waves. More detail will be discuss in the section of LPAV. The selection on lens pair is controlled by computer.

Optical paths at the joints of robotic arm are connected by optical fibers or pairs of mobile mirrors. A photodiode is used to receive the reflected laser beam and convert optical signals to electrical signals which will be digitized and displayed on the screen. The digitization should be at least 256 x 256 pixels, 8 bits deep. The image is created at a rate of 30 frames per second, which is truly in real-time.

Diode Laser

A GaAlAs Laser system, manufactured by D.O. Industries, Inc. was chosen as an optical source for the optical module. The GALA Laser System has been designed to replace HeNe lasers, at a substantially reduced cost and size. This stand alone system uses GaAlAs laser with output power level 15 mw and wavelength 780 nm. The size is only 50 x 50 x 107 mm which meets the requirement for compact size. This laser system has single longitudinal and transverse mode, TEMoo, output in the small collimated beam (1.5 x 0.7 mm) with a beam divergence less than 1.2 milliradians.

The use of longer wavelength may result in poorer resolution. For example, the spot waist of GaAlAs Laser (780 nm wavelength) at the focal plane is 1.2 time larger than that of HeNe laser (633 nm wavelength), in the same optical system. This drawback can be overcome by optics design. In addition, the diffraction efficiency of a light deflector may be wavelength dependent, however the effect may be negligible.

Laser Beam Deflector

A acousto-optic deflector developed by Zenith Radio Corp. operates at a center frequency 70 MHz. Although the optimum optical wavelength is designed to be 633 nm, a less than 10% drop in diffraction efficiency is found when we use a 780 nm laser. The deflected angle is approximated by the following formula:

$$\theta = 0.26 \times \lambda \times f \qquad\qquad (3.1)$$

where θ is the deflected angle in milliradians, λ wavelength in um and f frequency in MHz. For example, in the case that $\lambda = 780$ nm and f = 70 MHz, the θ is calculated to be

$$\theta = 0.26 \times 0.780 \times 70 = 14.2 \text{ mrad}$$

For the sweep scan in the frequency range from 50 MHz to 90 MHz, the laser beam is deflected by an angle between

$$\theta_{50} = 0.26 \times 0.780 \times 50 = 10.2 \text{ mrad}$$

and

$$\theta_{90} = 0.26 \times 0.780 \times 90 = 18.3 \text{ mrad}$$

The acoustic transit time is proportional to the optical aperture and can be approximated by

$$t \text{ (usec)} = 2.56 \text{ (usec/cm)} \times D \text{ (cm)} \qquad\qquad (3.2)$$

where D is the optical aperture in cm. For example, when D = 3.9 cm, t is equal to 10 usec.

Scanning Mechanism

The optical schematic of a scanning laser module is shown in Fig. 5. The laser is scanned in a raster fashion. The laser beam is horizontally deflected by an acousto-optic deflector and vertically scanned by a Galvo mirror. A pair of cylindrical lenses are used to horizontally expand the beam at the A-O deflector and then collimate the beam again. Beam expansion at the deflector is desired because the bigger the aperture is the higher the diffraction resolution.

The vertical scan size is directly controlled by the voltage applied to the Galvo mirror, while the horizontal scan size is controlled by the A-O deflector according to the following formula:

$$\Delta X = (F'_3 / F'_4) \times 0.26 \times \lambda \times \Delta f \qquad\qquad (3.3)$$

where the F'_3 and F'_4 are the focal length for lenses L'_3 and L'_4, respectively. Δf is the frequency sweep range. For example, the laser module in SLAM has a system $F'_3 = 400$ mm and $F'_4 = 50$ mm so that the horizontal scan range is 0.82 mrad for 633 nm wavelength and 1.01 for 780 nm. The spot size of HeNe laser is 1.25 mm x 1.25 mm which results in a collimated spot at the Galvo Mirror with a size 3.2 mm x 2.5 mm after passing through all the Lenses (L'_1, L'_2, L'_3 and L'_4). The GALA Laser has a beam spot 1.5 mm x 0.7 mm and the output of Laser Module, if same optics are used, will be 3.9 mm x 1.4 mm. Change of L'_2 and L'_3 is required to obtain a circular output beam.

Optical System

The optics employed to deliver the scanning laser beam in a SLM has been reviewed and an example design is schematically illustrated in Figure 6. The laser beam output from the Laser Module is focused by a lens L_9, in the 100 MHz case, to the coverslip (or the surface of test sample). The scan field of view is governed by equation (3.4)

$$\Delta X_{100} = F_9 \times (F'_3 / F'_4) \times 0.26 \times \lambda \times \Delta f \qquad\qquad (3.4)$$

and the focused laser beam has a waist of

$$W_{100} = 1.22 \times \lambda \times F_9 / W_1 \qquad\qquad (3.5)$$

where W_1 is the output beam spot of the Laser Module. In the HeNe case, $W_1 = 3.9$ mm so that W_{100} is calculated to be 24 um.

For the case of 30 MHz Optics, a telescope consisting with lenses L5 and L6 is used, and the field of view and the focused spot become, respectively

$$\Delta X_{30} = (F_5 / F_6) \times \Delta X_{100} \qquad\qquad (3.6)$$

and

$$W_{30} = (F_5 / F_6) \times W_{100} \qquad\qquad (3.7)$$

The spot size is calculated for F5 = 100 mm and F6 = 25.4 mm, to be 99.8 um. In the 10 MHz case, a telescope of L3 and L4 is used. The scanning field and the focused spot can be obtained by a similar calculation.

3.4 LPAV (Laser Probing Acoustic Vision)

LPAV module is composed of a transmitter (an acoustic transducer) and a receiver (SLM and knife-edge detector) which will be incorporated in MFRS as shown in Figure 7. LPAV shares exactly the same optics as those used in SLM. Several frequencies are selected for various resolution and penetration requirements. Frequencies of interest include 10, 24, 30, 50, and 100 MHz. The selection of operating frequency and the corresponding SLM optics is achieved by computer control.

To design the module of LPAV we have comprehensively reviewed the optical system currently implemented in a commercially available SLAM. The Laser Module and Optical Module to be implemented for SLM and LPAV are basically the same and they were described in previous section. The only difference is the detection techniques. The detection unit employed by SLM is simply a photodiode, while a more complicated Knife-Edge detector is needed by LPAV.

The factors affecting the performance of Knife-Edge detection include laser spot size, ultrasound wavelength, incident angle, knife-edge and imaging optics. In this report, we briefly describe the design guidelines which must be followed for the design of LPAV.

A brief design guideline for the optical system and the knife-edge detection to be implemented in Acoustic Microscopy has been established. The use of optical fiber will be investigated. The system design will be finalized in the Phase II.

Design Guidelines

Knife-Edge Detection

The knife-edge detector must be placed at the F.T. (Fourier Transform) plane of the detection plane (e.g. coverslip of SLAM). The detection plane must be the F.T. plane of the laser scanner (the output plane of the Laser Module), which is illustrated in Fig. 8. There are always some technical difficulties associated with the knife-edge technique. To replace knife-edge, innovation such as development of optical superheterodyne systems as shown in Fig. 9 may be needed. During the Phase I, a preliminary study on the superheterodyne has confirmed the applicability of such system. In the Phase II, an optical heterodyne system as shown in Fig. 9 (b) will be investigated and implemented in LPAV, whenever applicable.

Laser Spot Size Requirement

The focused laser spot size at the detection plane must be in the neighborhood of 1/2 acoustic wavelength to achieve the best sound-light interaction efficiency.

Incident Angle of Ultrasound Wave

The incident angle must be in the neighborhood of 10 degrees with respect to the detection plane (coverslip) for the best knife-edge detection sensibility.

Field-of-View

The field of view has to be maximized without sacrificing resolution. The field of view for each SLAM image frame can be figured out by the following:

$$F.O.V = N \times 1/4 \times \lambda a$$

where N is the number of pixels per line scan. λa is the effective wavelength at the coverslip.

Optical Path Length

Telescope lenses will be designed to meet the requirements of optical path length, laser spot size and field of view for various ultrasound frequencies. Therefore the lenses to be used in Figure 7 must meet all the following specifications:

$$\text{Field of View} = F_3 \times (F_2 / F_1) \times A$$

$$\text{Spot size} = F_3 \times (F_2 / F_1) \times Wo$$

$$\text{Optical path} = 2 (F_3 + F_2 + F_1)$$

where F_1, F_2 and F_3 are the focal lengths for Lenses L_1, L_2 and L_3, respectively. A and Wo are the scan size and spot size of laser beam coming out from the Scanning Laser Module. For example, in the case of 100 MHZ as shown in Figure 6, a telescope with a magnification of 1 is used to match the required spot size, scanning size and optical path length.

Compact System Design

The required number of parts must be minimized to make the whole system compact enough to fit in with a robotic arm. Fiber optics or a pair of mobile mirrors may be required at the joint for the flexibility of the arm motion.

LPAV Operation

The LPAV uses high frequency ultrasound in combination with a scanning laser beam detector to create real-time images of elastic characteristics of materials at microscopic level. A SLAM system diagram is illustrated schematically in Figure 10. A sample is placed between an insonifying transducer and detector. The transducer is a piezoelectric element and the detector is a scanning focused laser beam.

The transducer transmits a continuous plane wave of ultrasound through the entire thickness of the sample. As the ultrasound travels through the material, defects within the sample spatially alter its transmission. The ultrasound is reflected, refracted or absorbed by internal discontinuities such as cracks, delaminations, voids or inclusions. This results in a nonuniform wave pattern at the other side of the sample, which can be detected by a low power scanning laser. The laser acts as a point-by-point detector of the ultrasound wave motion and can translate information on internal features of the sample into video signals through the use of a photodiode and knife-edge detection technique. In order to provide a specularly reflecting surface for the scanning laser beam, the specimen is placed in close proximity to a plastic mirror which serves as the detector plane.

The variations in ultrasound transmission are displayed on a TV monitor where the bright regions correspond to defect-free areas of high transmission through the sample, whereas, the darker areas correspond to regions of higher ultrasonic attenuation attributed to defects or changes in elastic properties because of scattering, reflection or absorption of ultrasound. LPAV is highly sensitive to any cracks or disbonds within a sample and can be used for on-line inspection of structural components, searching for defects such as delaminations, disbonds, porosity and so on.

3.5 CSAM (C-mode Scanning Acoustic microscopy)

In a previous SBIR Phase II contract granted by DOE, a new C-SAM was developed to perform cylindrical scanning over superconducting rods. A rotator which accommodates samples with diameters ranging from about 0.1" to 1.5" has been designed and constructed. The superconducting rod is mechanically rotated while the transducer itself is moved back and forth very rapidly along the length of the rod. A raster scan over a cylindrical surface is thus created.

However, in this Phase II project the CSAM module is developed to be incorporated in a robotic arm so that it can track surface contour of test specimen. A mechanism which keeps the transducer normal to sample surface will be developed in the Phase II.

Other features of CSAM that will be developed in Phase II include AIPD (Acoustic Impedance Polarity Detection), QBAM (Quantitative B-scan Analysis Module) and 3D-TOF (Time of Flight) imaging. Transducers are selected with respect to operating frequency, focal length, and F-number. System parameters include focus, gains, gate position, gate width, scan size and scan speed. CSAM can be operated in either reflection mode or transmission mode. When the latter is elected, the second robotic arm is required.

Operation Principle

In a conventional C-SAM, the pulse-echo technique was utilized to produce images. The return time for each echo depends upon the distance between transducer and the interface where the echo occurs. The echo amplitude and polarity may depend upon the differences in acoustic impedances of the materials encountered. To image a plane at a desired depth below the sample surface, an electronic gate automatically opens and closes at selected times to excerpt the desired signal from the train of echoes. The echo amplitude determines the brightness on the CRT display, which is synchronized to the transducer position. The transducer is mechanically scanned over the sample by computer-controlled stepping motors to create a raster scan. This type of imaging is then called C-Scan.

System Parameters

The CSAM module is developed in such a way that the inspection operation is fully computer controlled. Computer programs implemented in the system provides operator with the following controls:

a). Scan Size: 0.1" to 3" in length and 12° to 360° in rotation.
                   The image is presented by 256 x 240 pixels.

b). Scan Speed: Ranging from 0.5" per second to 4" per second.

c). Cursor: Select the center of scanning area.

d). Focus: Move transducer up and down to focus at interested
                   depth, e.g. cylinder-in-cylinder interface.

e). Color Maps: 30 maps for selection to highlights defects.

f). Front Gain: Adjust the incident ultrasound energy (0-61.5 dB).

g). Echo Gain: Adjust the gated echo amplitude (0-27 dB).

h). Trigger: Trigger to Front Interface Echo or Main Bang.

i). Gate pos.:   Move electronic gate position to extract echoes at
                   interested depth.

j). Gate width: Adjust the inspection depth coverage.

The computer programs also allow operator to store and retrieve files
for future use as well as print a hard copies for documentation.

CSAM Operation

In order to secure the best result, the operator first has to focus
the ultrasound on the object and then adjust the proper gains. It is
followed by the selections of desired scan size and speed. The electronic
gate can be positioned to extract the echoes of interest, with a desirable
gate width. Once these parameters are set, the system can automatically
acquire and record the amplitude of the gated echo (in time domain now, and
will be in frequency domain later in SAPS) pixel by pixel and display the
result in a 256 by 240 pixel image. At each data point, or each pixel, the
amplitude of return echo is linearly digitized in a scale of 256 levels.
An area in which the amplitude of return echo is higher than a
predetermined threshold can be highlighted by the selection of an
appropriate color map. A 2-D distribution map of defects can be obtained
in about 10 to 30 seconds depending upon the scan size and speed.

3.6 SAPS (Scanning Acoustic Pulse Spectroscope)

SAPS is based on CSAM technology and differs from CSAM in the signal processing. CSAM acquires and displays amplitude data while SAPS performs spectral analysis. A PC-based plug-in circuit board will be built to digitize and analyze frequency components of the spectrum. Computer programs will be developed to distinguish two closely spaced echoes, based on the fact that the closer two pulses are in time domain the farther apart two nodes are in frequency domain, and to improve detection resolution, based on the frequency-dependent attenuation data. SAPS and CSAM share the same transducer selections and system parameters.

Operation Principle

Consider an ultrasonic longitudinal wave propagating through a plate which is immersed in water, as shown in Figure 11. In the propagation from medium 1 (water) to Medium 2 (plate), the amplitude transmission coefficient is defined as

$$T_{1,2} = 2 Z_1 / (Z_1 + Z_2) \tag{3.8}$$

and the reflection coefficient is

$$R_{1,2} = (Z_2 - Z_1) / (Z_1 + Z_2) \tag{3.9}$$

and

$$R_{1,2} = - R_{2,1} = R \tag{3.10}$$

where Z_1 and Z_2 are acoustic impedances of medium 1 and 2. The subscript i,j denotes the case that the wave propagates from medium i into j. If the attenuation in the medium is neglected, the amplitude of the n_{th} echo, or the echo after n times reflection from the back surface of the plate, is

$$A_n = - T_{1,2} T_{2,1} R^{2(n-1)} \tag{3.11}$$

The minus is included in equation because the multiple reflection echoes are always in the opposite polarity of the first front surface echo. We make the term R itself a positive quantity. Eq. (3.11) can be rewritten in the form

$$A_n = - (1 - R^2) R^{2(n-1)} \tag{3.12}$$

Let s(t) be the incident wave and assume that the attenuation and structural perturbations (e.g. texture, grain size, ..) are negligible, the total detected signal r(t) can be written as

$$r(t) = s(t) + \sum_{n=1} A_n \, s(t-nT) \qquad (3.13)$$

with $\qquad\qquad T = 2D \, / \, V$

where T is the round-trip time of flight between the front and back surfaces, and D and V are thickness and ultrasound velocity of the plate, respectively. By taking Fourier transform of Eq. (3.13), it becomes functions of frequency, f,

$$R(f) = S(f) + \sum_{n=1} A_n \, S(f) \, e^{-j(2\pi fnT)} \qquad (3.14)$$

where S(f) and R(f) are Fourier transforms of s(t) and r(t), respectively. The transfer function of the plate can be derived from Eq. (3.14) as

$$H(f) = 1 + \sum_{n=1} A_n \, e^{-j(2\pi fnT)} \qquad (3.15)$$

or

$$= 1 + \frac{(1-R^2) \, e^{-jx} \, (R^{2N} e^{-jNx} - 1)}{1 - R^2 e^{-jx}}$$

Where N is the number of echoes from the back surface being taken into consideration, and $x = 2\pi fT$. This transfer function exhibits a periodic function of $f_o=1/T$. The resonant frequencies for which the thickness of the plate is a multiple of the half-wavelength of the ultrasound wave are expressed as $f_n=nf_o$, n=0, 1, 2, 3, ... The thickness of the plate can then be calculated from the resonant frequency f_o by

$$D = V \, / \, 2f_o \qquad (3.16)$$

This theory is applicable to the detection of defects within close proximity and D is now the depth of defects below the surface.

System Design

SAPS and CSAM shares the same transducer selections and system parameters. SAPS differs from CSAM only in signal processing. A PC-based plug-in circuit board will be built to digitize and analyze frequency components of the spectrum (see Figure 12).

3.7 MFRS System Operation

The MFRS system control can be categorized into two major functions: Robot control and Inspection manipulation (see Figure 13). Robot control can be either manual or automatic. Inspection technique may be selected among the installed modules SLM, LPAV, CSAM and SAPS.

The prime controls of the robot are translation, rotation and angulation, depending on the required degree of freedom. The robot arm design being selected to be implemented in the Phase II (see Figure 2) involves 3-axis translation and another 3-axis rotation, which is deemed enough for most of NDE applications. The robot motion can be controlled manually or automatically when routine inspections are being performed.

Robot vision which is provided by a camera is optional and will not be included in this Phase II project.

Inspection can be categorized in two groups: Optical Inspection and Acoustical Inspection. Optical inspection is good for searching surfaces for defects such as machining damage, fatigue cracks or any surface anomalies. Optical inspection can be performed by SLM or a camera (same camera as used for robot vision) whichever available. The advantages of using SLM include polarization manipulation of laser beam to highlight surface cracks and selectable laser spot sizes to minimize background noises. In addition, the SLM produces higher contrast images than a camera due to the point source illumination.

In contrast to optical inspection, acoustical inspection provides NDE of subsurface defects. Acoustical NDE techniques allow us to actually "see" inside an optically opaque material. Acoustical inspection techniques provided by the proposed MFRS, as shown in Figure 14, include reflection-mode CSAM (R-CSAM), transmission-mode CSAM (T-CSAM), reflection-mode SAPS (R-SAPS), transmission-mode SAPS (T-SAPS), and LPAV, among which LPAV, T-CSAM and T-SAPS require two robotic arms.

CSAM, either R-mode or T-mode, share hardwares with SAPS. Transducer is selected with respect to operating frequency, F-number and focal length. System parameters can be controlled for gains, focus (time of return surface echo), trigger level, gate position and width, and scan size and speed. In addition, SAPS can also choose the center frequency and sweep range of spectrum.

LPAV shares optics with SLM and can choose different fields of view and laser spot sizes, depending the operating acoustic frequency selected for various resolution and penetration requirements.

Several electronic circuits will be needed to process the signals and images, including a real-time video digitizer, a digital integrator, a mass storage device and a PC-computer based image analysis system. Computer software will be developed in Phase II to automatically recognize the defects detected by the above mentioned methods. Several computer algorithms including 3DIMPACT, RTSTRESS and CYLJOIN will be also developed in the Phase II to expand the applications of MFRS to those specified by the aerospace industry.

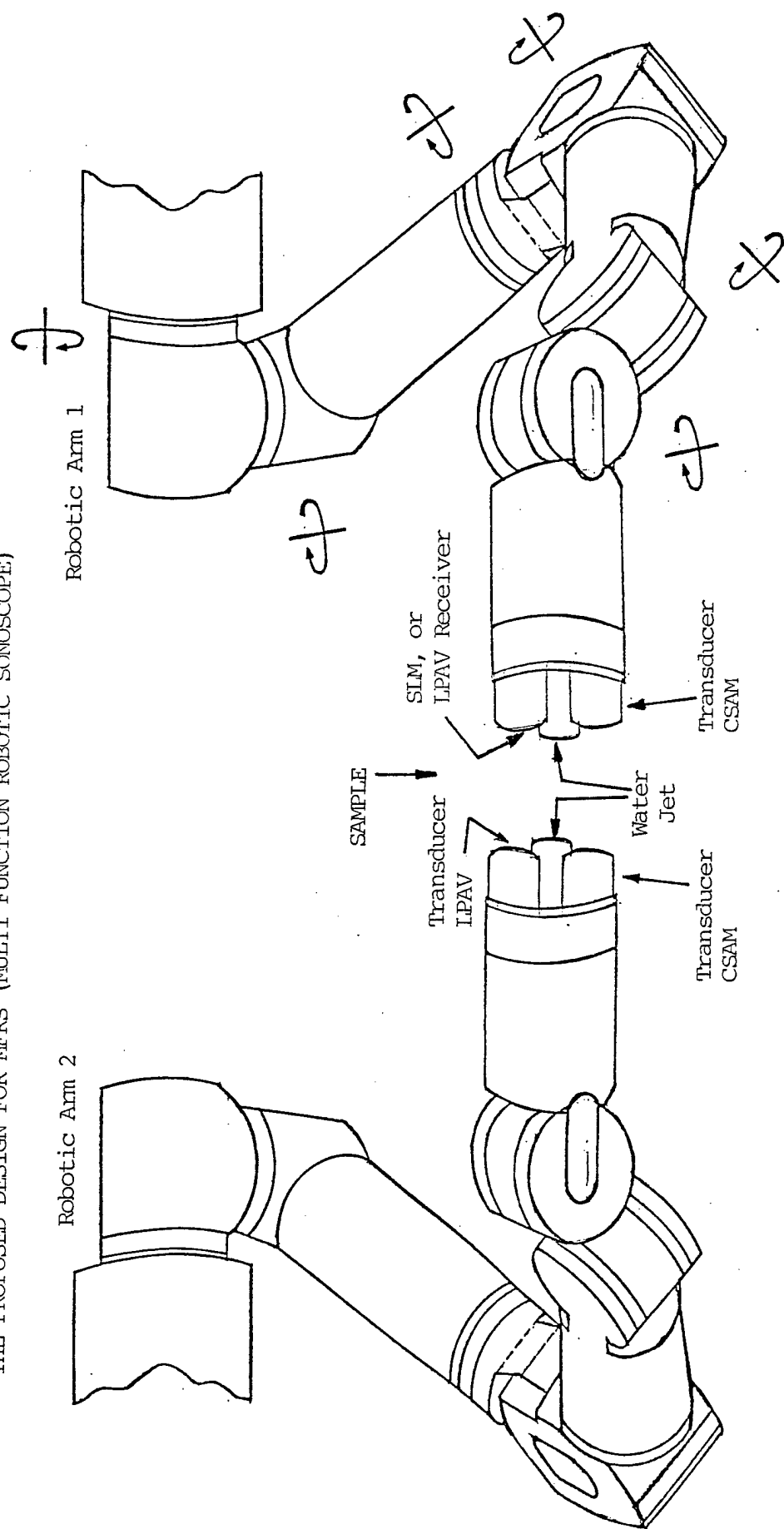THE PROPOSED DESIGN FOR MFRS (MULTI-FUNCTION ROBOTIC SONOSCOPE)

Figure 1. Full implementation of MFRS, including modules for SLM, LPAV, CSAM (reflection and transmission modes) and SAPS. Water jets are used to provide coupling of ultrasound to the sample. Actual implementation may be much simpler, depending on the applications.

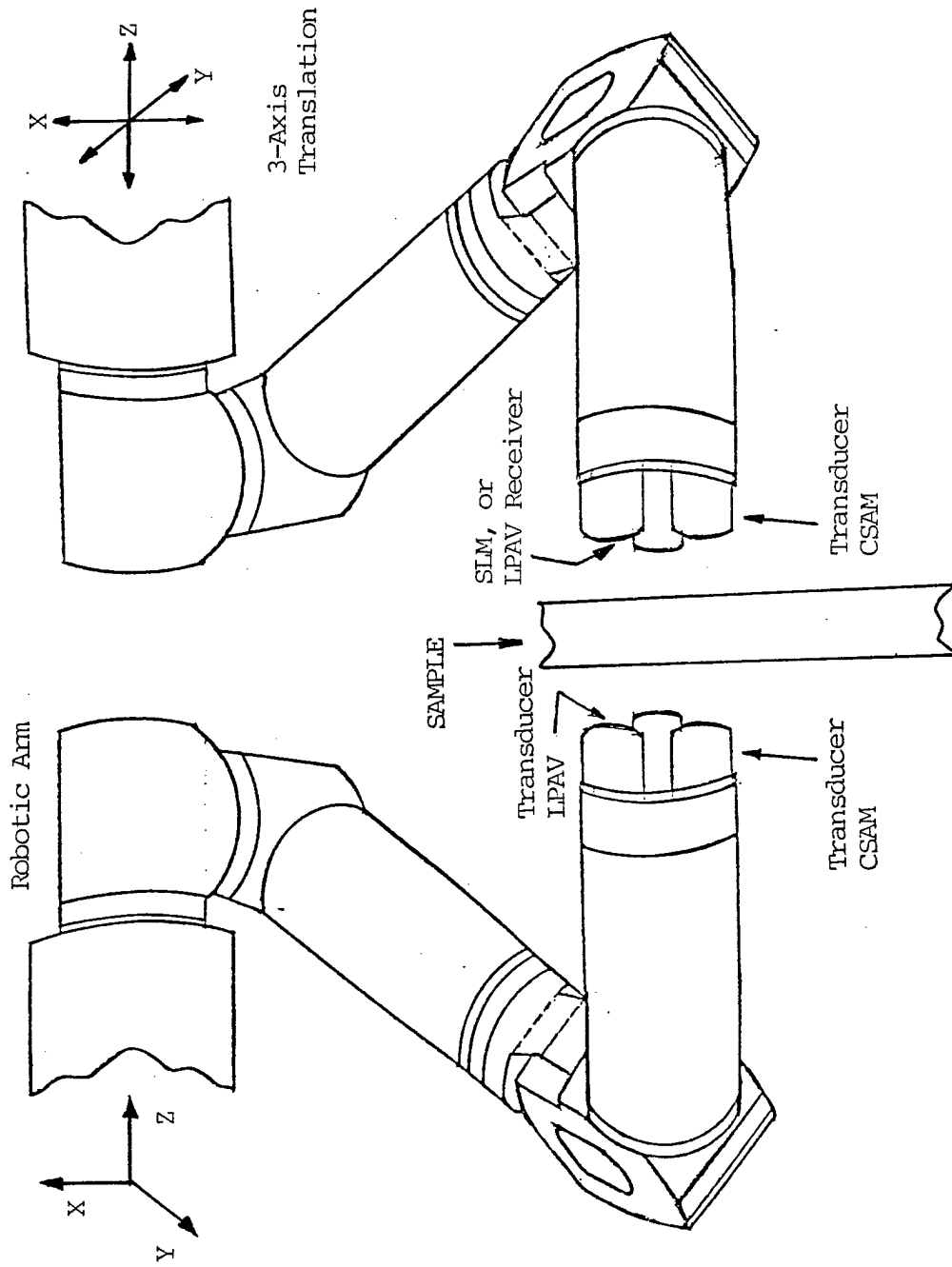THE MFRS SYSTEM TO BE IMPLEMENTED IN THE PHASE II PROJECT --

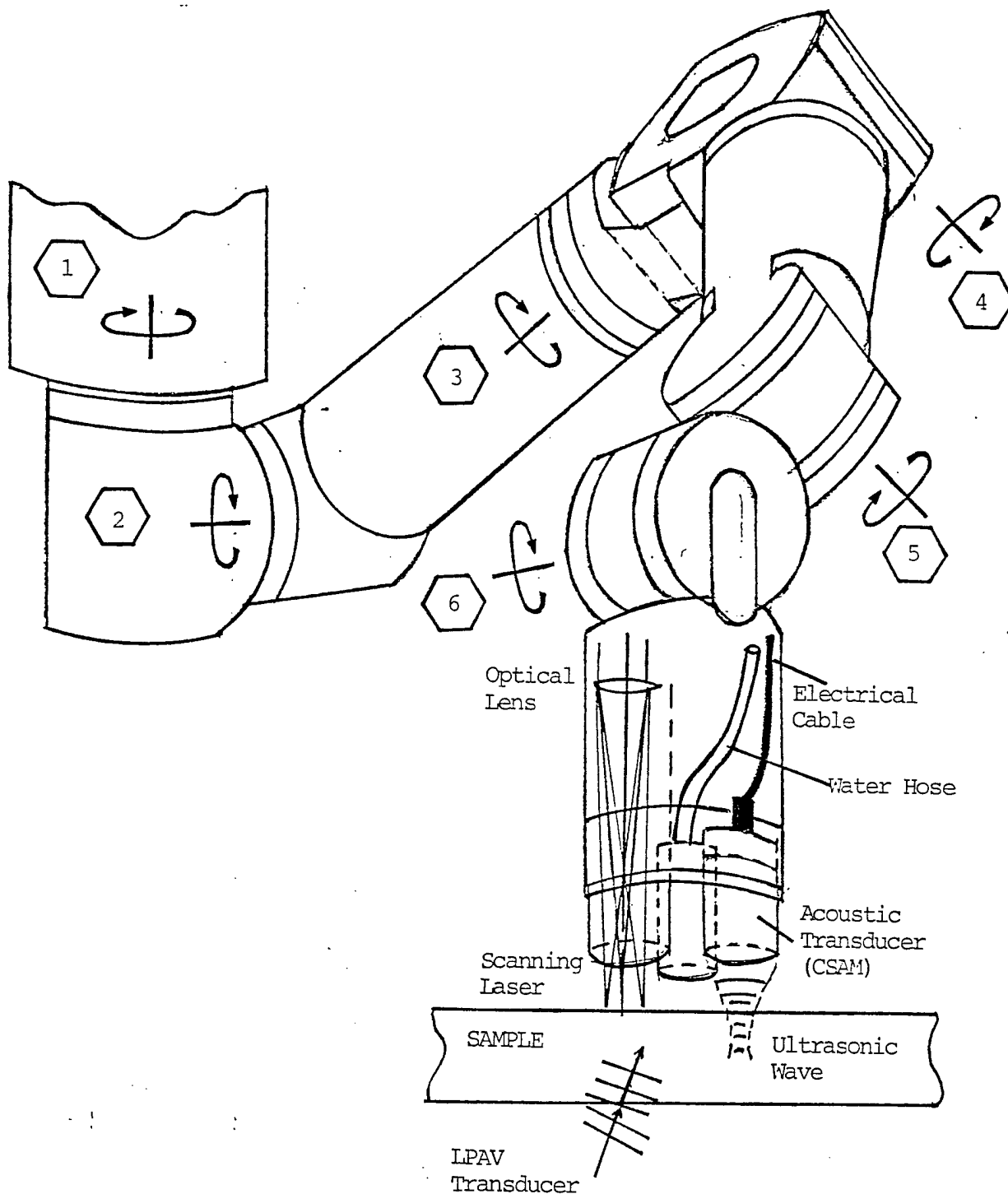Figure 2. Simplified implementation of MFRS for on-line inspection.

Figure 3.   Design of Robotic Arm, incorporating all components
needed for SLM, LPAV and CSAM functions. There are
six-axis of freedom, although it may require less in
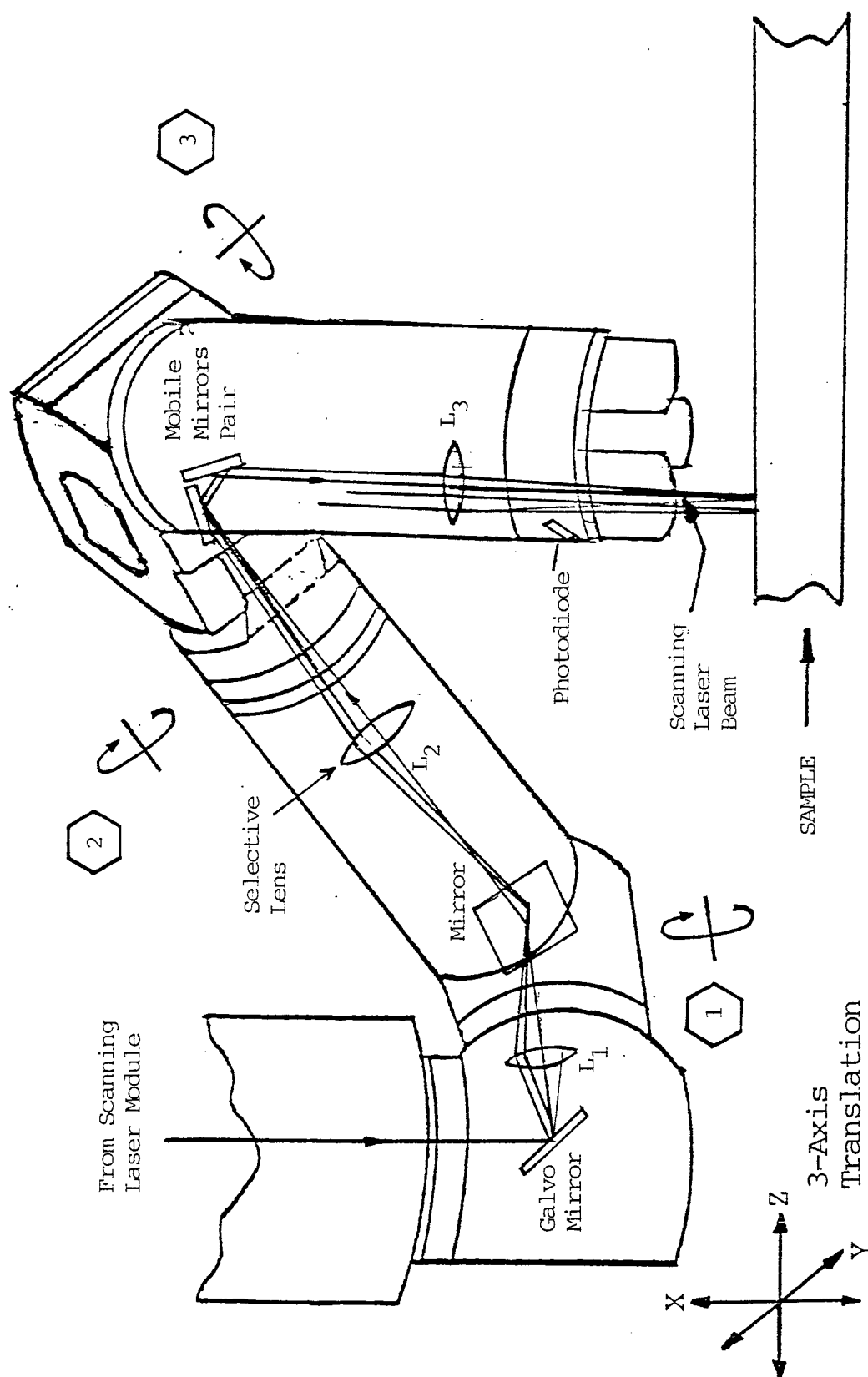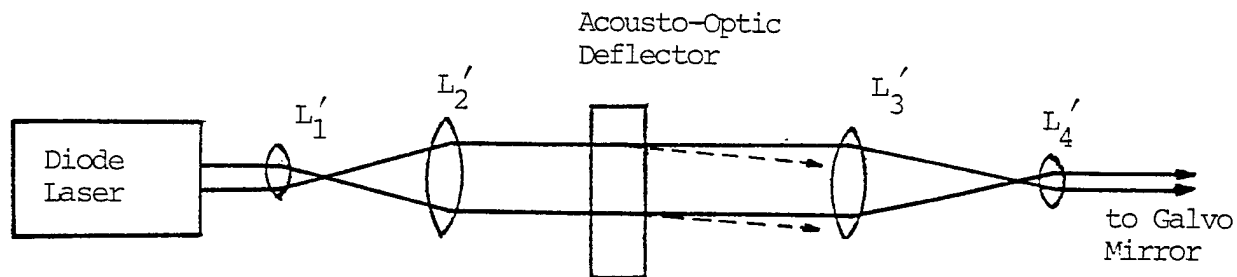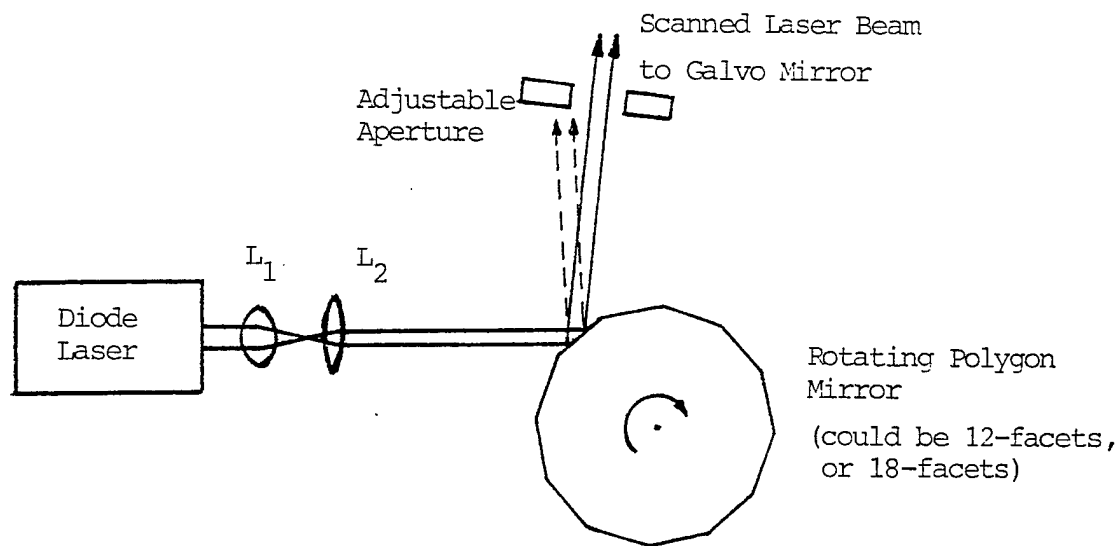actual implementation.

Figure 4. Implementation of Scanning Laser Microscope (SLM) in a 3-axis Robotic arm. The lenses L_1, L_2, and L_3 can be selected for various field-of-view and resolution requirements.

L_1', L_4' spherical lenses

L_2, L_3 cylindrical lenses

(a) Horizontal scanning using A-O deflector.

(b) Horizontal scanning usin rotating polygon mirror.

Figure 5. Horizontal scanning mechanism using (a) A-O deflector, and (b)
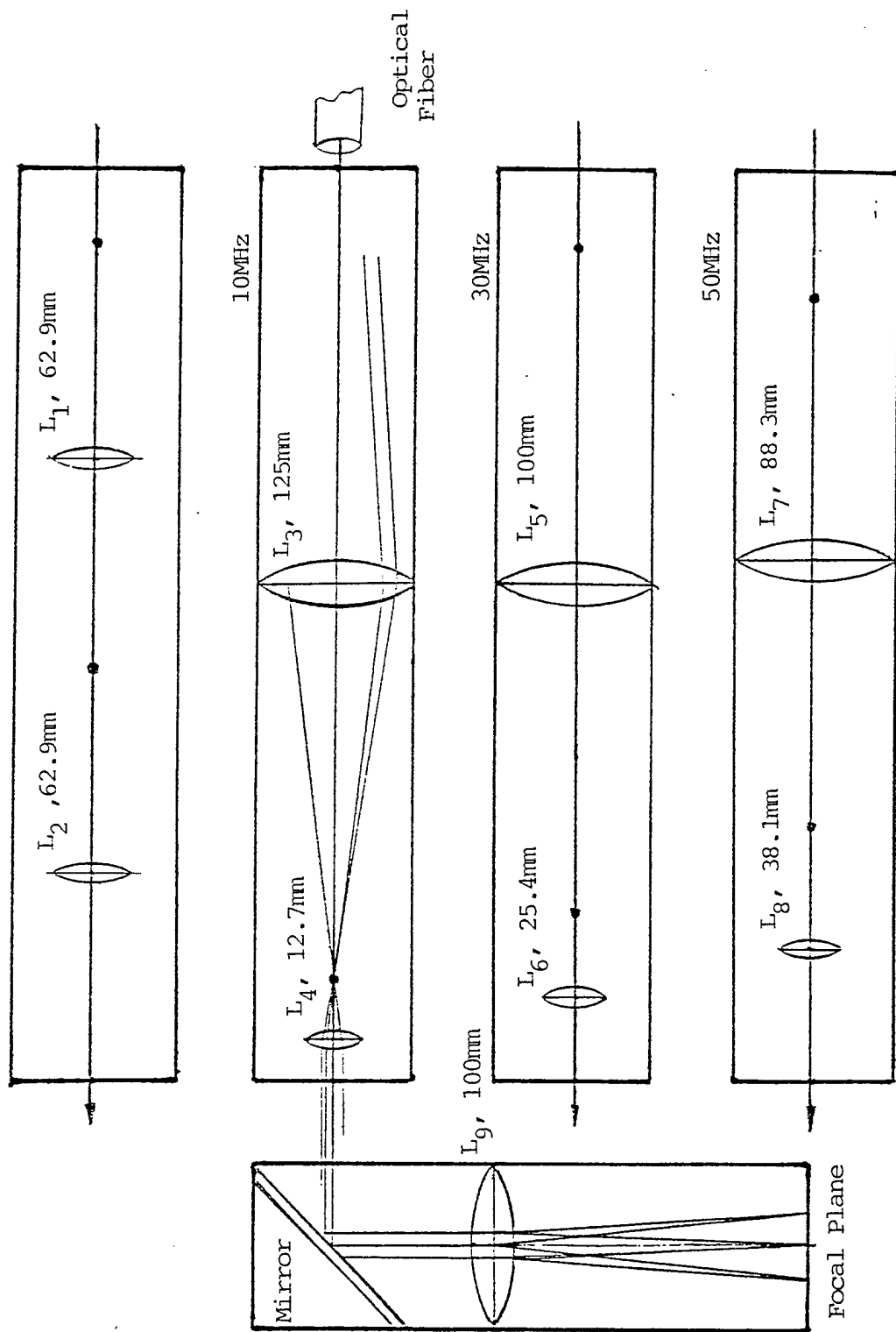a rotating polygon mirror.

Figure 6 . Selective Optical Module for 10, 30, 50 and 100 MHz frequencies of ultrasound.
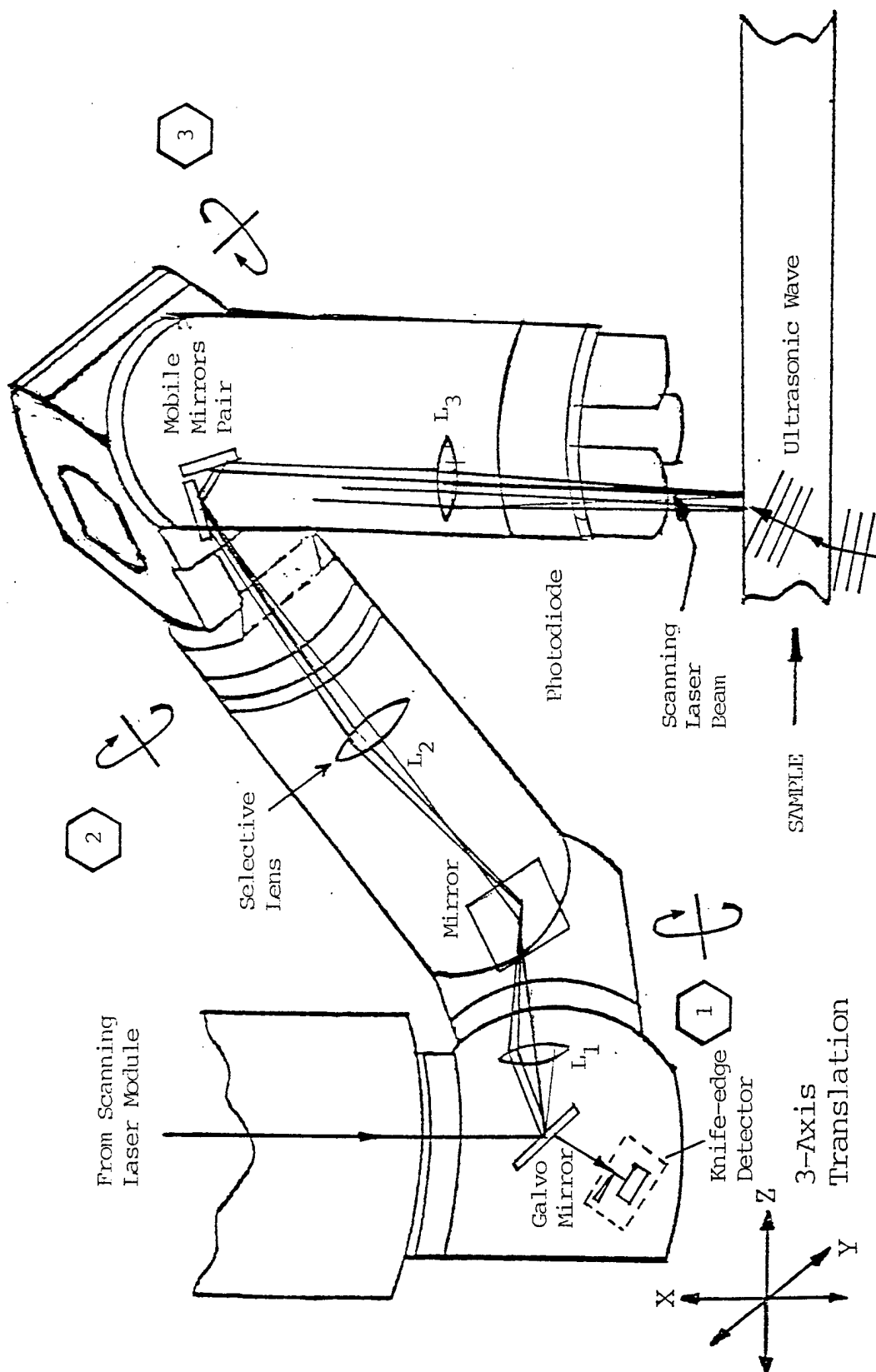
Figure 7. Implementation of Laser Probing Acoustic Vision (LPAV). The lenses L_1, L_2, and L_3 will be selective for various resolution and field-of-view needs.
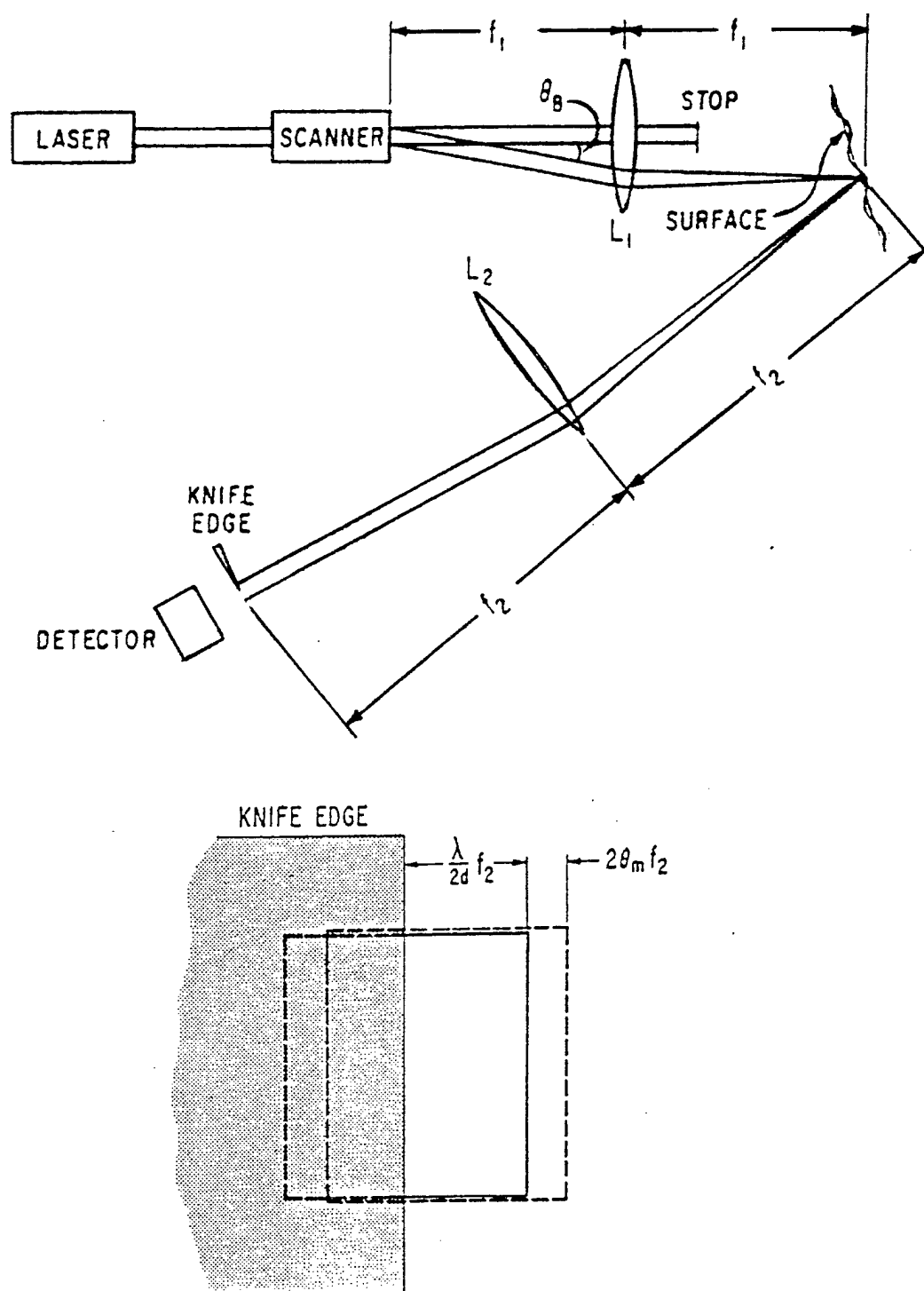
84

Figure 8. An optical set up for knife-edge detection technique.

ALUMINIZED
GLASS
DISK

ROTATING GLASS CUBE

RCA
7265
PHOTOTUBE

QUARTER
WAVEPLATE

OPAQUE
OBJECT

CALCITE
PRISM

LONG-
FOCUS
LENS

WATER

TRANSDUCER

$f_1 = 2.6$ MHz

BEAMSPLITTER
MIRROR

BRAGG CELL

LASER

OPTICAL LOCAL OSCILLATOR
BEAM AT $f_o + 25$ MHz

VOLTAGE FROM POTENTIOMETER
ROTATING WITH GLASS CUBE

MIXER

BAND
PASS
FILTER

f_3

25 MHz

f_2

OSCILLOSCOPE

ELECTRONIC
LOCAL OSCILLATOR
($f_2 = 22.5$ MHz $- f_3$)

VERTICAL
DEFLECTION

HORIZONTAL
DEFLECTION

(a) Configuration for ultrasound image conversion.

LENS
L

SIG. GEN.

PHOTO
DIODE

$f_o - f_s$
$f_o + f_s$

WATER FILLED
BRAGG CELL

ℓ

f_m

LASER

f_o

f_o

WEDGE

D

f_s

M₁

$f_o - f_s$

X AXIS
DRIVE
MECH.

SIG. GEN.

M₂

VHF
RECEIVER

HP415E

XY
RECORDER

Y   X
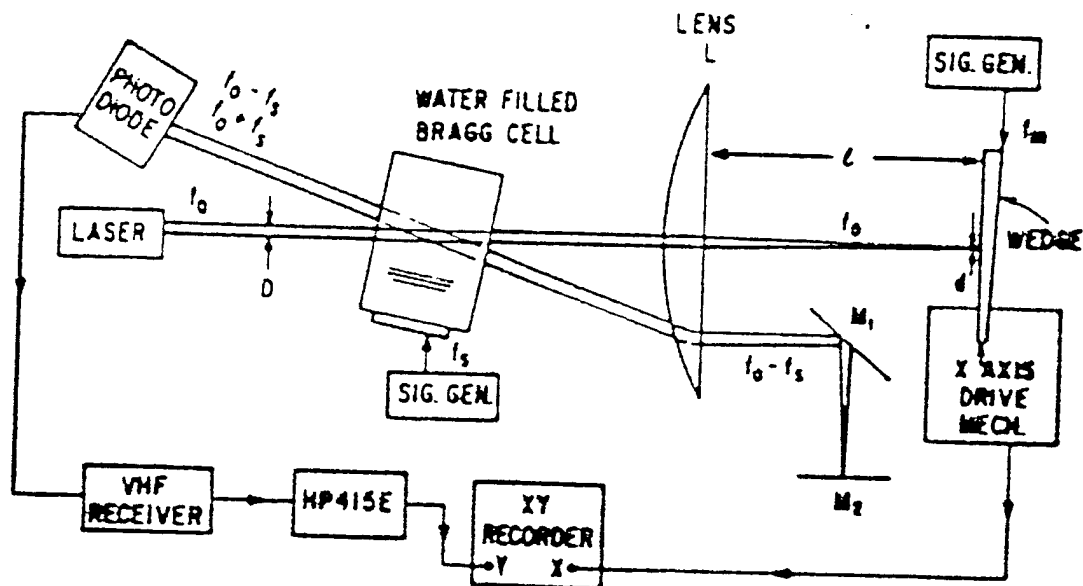
(b) Optical heterodyne system.

Figure 9. Two alternative heterodyne techniques to be developed in
the Phase II to replace knife-edge technique.
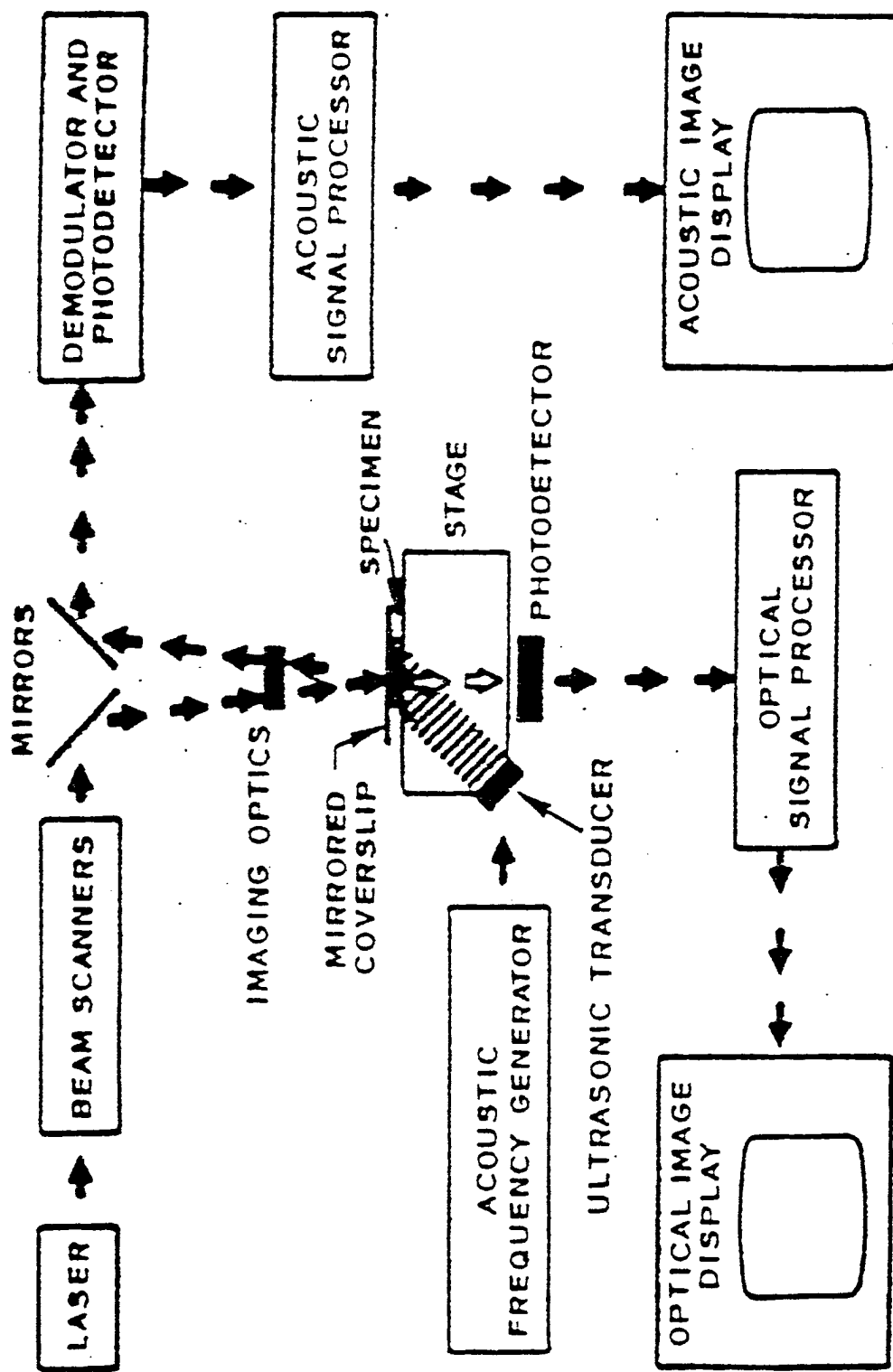
Figure 10. Schematic diagram for Laser Probing Acoustic Vision (LPAV system).

Figure with labels:

Incident Wave — R — $-T^2R$ — $-T^2R^3$

Medium 1

Z_1, V_1

$-TR$ — $-TR^3$ — Medium 2

T — TR^2 — Z_2, V_2
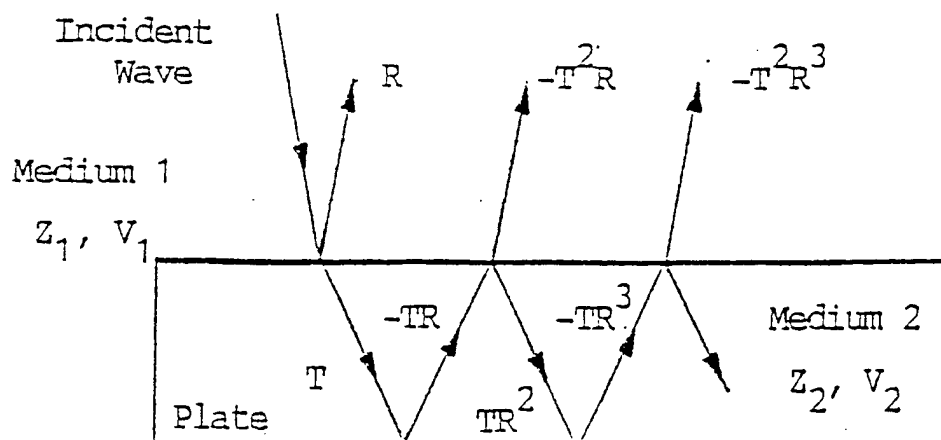
Plate

transmission coefficient

$$T_{1,2} = 2 \ Z_1 \ / \ (Z_1 + Z_2)$$

reflection coefficient

$$R_{1,2} = (Z_2 - Z_1) \ / \ (Z_1 + Z_2)$$

$$R_{1,2} = - R_{2,1} = R$$

Figure 11. Multiple reflections in a plate and their transmission and reflection coefficients.

Robotic Arm

Translation Control

T/R

Pulser/ Receiver

CSAM/SAPS Transducer

Acoustic Lens

Rotation Control

Spectrum Analysis

Oscilloscope

Test Specimen

A/D Converter

NDE of bond quality in a cylinder-in-cylinder bonding

COMPUTER
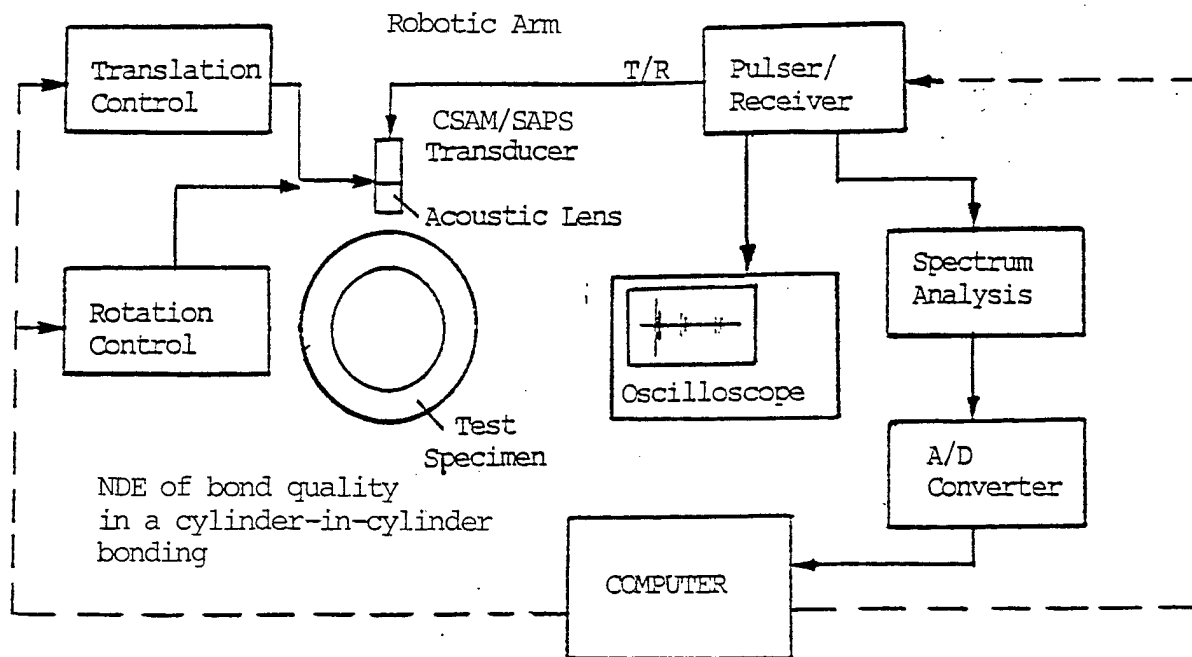
Oscilloscope Trace
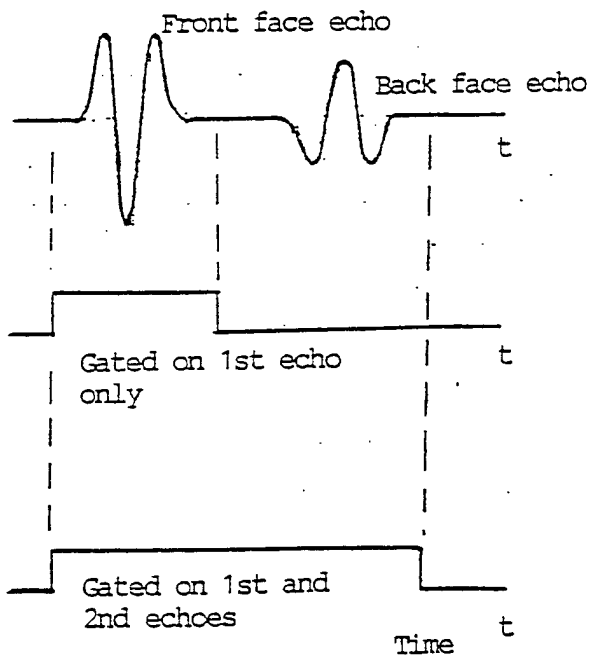
Spectrum Analyzer Trace

Front face echo

Back face echo

t

Gated on 1st echo only

t

f

Resonant Frequencies

f_2 f_3

f_1 f_4

Gated on 1st and 2nd echoes

Time

t

Frequency

f

Figure 12. System diagram and operation principle of Scanning Acoustic Pulse Spectroscope (SAPS).

89

Acoustical Inspection

```
                    ┌─────────────────┐
                    │   Acoustical    │
                    │   Inspection    │
                    └────────┬────────┘
         ┌───────────────────┼───────────────────┐
┌────────┴────────┐ ┌────────┴────────┐  ┌────────┴────────┐
│ C-Scan Imaging  │ │Spectral Analysis│  │      LPAV        │
│  R-Mode/T-Mode  │ │  R-Mode/T-Mode  │  └──────────────────┘
└─────────────────┘ └─────────────────┘
```
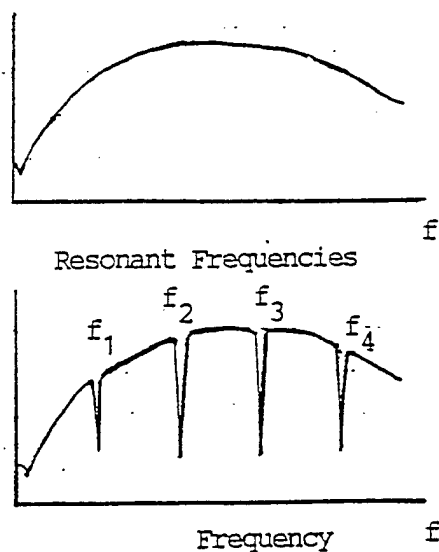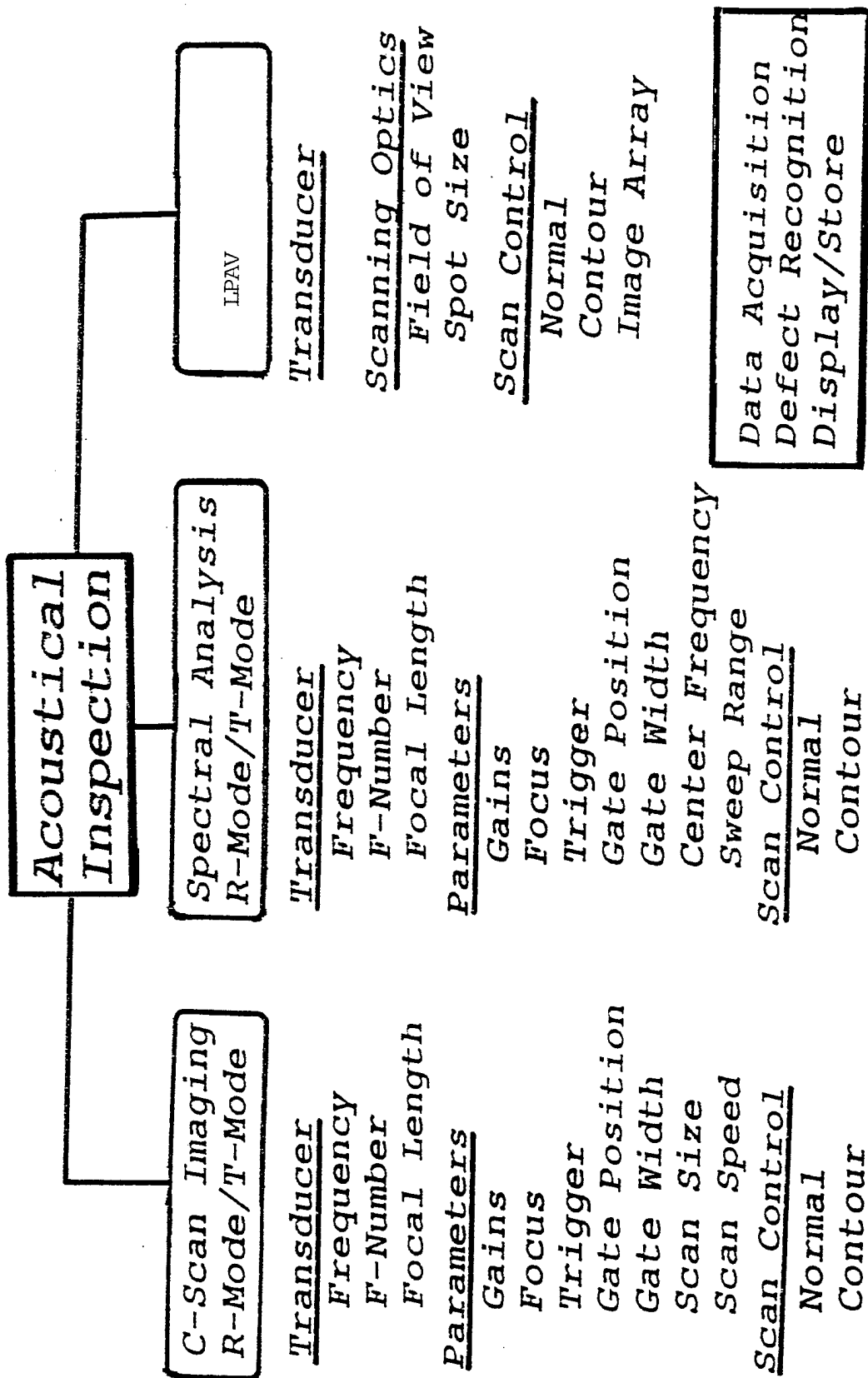
C-Scan Imaging
R-Mode/T-Mode

Transducer
  Frequency
  F-Number
  Focal Length
Parameters
  Gains
  Focus
  Trigger
  Gate Position
  Gate Width
  Scan Size
  Scan Speed
Scan Control
  Normal
  Contour

Spectral Analysis
R-Mode/T-Mode

Transducer
  Frequency
  F-Number
  Focal Length
Parameters
  Gains
  Focus
  Trigger
  Gate Position
  Gate Width
  Center Frequency
  Sweep Range
Scan Control
  Normal
  Contour

LPAV

Transducer

Scanning Optics
  Field of View
  Spot Size
Scan Control
  Normal
  Contour
  Image Array

Data Acquisition
Defect Recognition
Display/Store

SONO
SCAN ®

Figure 14.   LPAV, CSAM and SAPS functional diagram.

MFRS BLOCK DIAGRAM

MFRS

Robot

Motion Control

Manned
- 3-D Motion
- Rotation
- Angulation

Automated
- Contour

Vision (Camera)
(optional)

- Zoom
- Focus

Inspection

Optical Inspection

Visual/Camera
- Zoom

Scanning Laser
- Field of View
- Resolution
- Polarization

Acoustical Inspection

- C-Scan, R-mode
- C-Scan, T-mode
- Spectral Analyzer, R
- Spectral Analyzer, T
- LPAV

SONO SCAN®
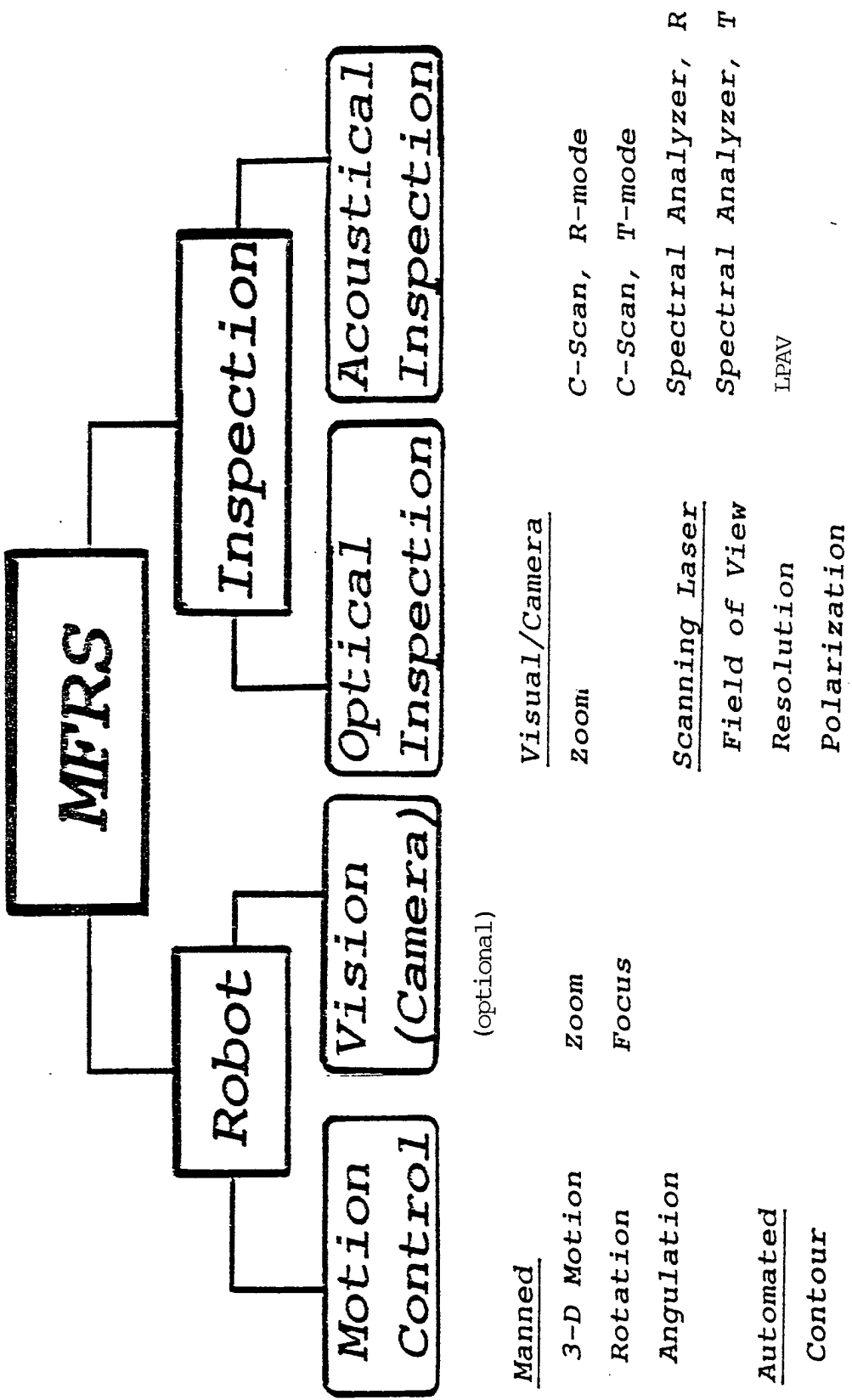
Figure 13. System block diagram for MFRS.

QUANTITATIVE EVALUATION OF IMPACT DAMAGE IN COMPOSITES USING ACOUSTIC MICROSCOPY

A. C. Wey, L. W. Kessler, and B. Ho[*]

Sonoscan, Inc., Bensenville, IL 60106

[*] Department of Electrical Engineering
Michigan State University, E. Lansing, MI 48824

ABSTRACT

A C-Scan mode acoustic microscope (C-SAM) and a through-transmission scanning laser acoustic microscope (SLAM) were used to nondestructively evaluate damage in graphite/epoxy composite laminates which had been subjected to low-velocity impact. Total delamination area was quantitatively measured for all laminated interfaces through the entire thickness. The results from C-SAM and SLAM inspection agree with those from X-radiographs and analytical prediction. Because the measurement is nondestructive, the results can be used to correlate with compression-after-impact strength of the impacted specimens, which is critically important for application of the materials in structural design.

INTRODUCTION

Although fiber-reinforced organic matrix composite laminates have high stiffness-to-weight and strength-to-weight ratios, they are susceptible to transverse low-velocity impact. Depending on the extent of the impact damage, the strength and stiffness of the materials can be significantly reduced.[1-3] Progress has been made in understanding impact damage [4-6]. However, because the damage is mostly embedded inside the materials, it is very difficult to detect. Conventional techniques for detecting impact damage include edge-replication [7], x-ray and ultrasonic imaging. Among the techniques only ultrasonic method is nondestructive.

A C-Scan mode acoustic microscope (C-SAM) [8] and a through-transmission type scanning laser acoustic microscope (SLAM) [9] were employed to nondestructively and quantitatively measure total damage area in graphite/epoxy composite plates which had been subjected to low-velocity impact test. SLAM provides an instant projection view of all delaminations at laminated interfaces, while C-SAM delineates delamination profile layer by layer in the laminated composite.

All conventional ultrasonic imaging techniques, including SLAM and C-SAM, have limitations that because of overlapping, some part of the damage pattern may be shadowed by the delaminations occurred at prior interfaces. An analytical model [10] was needed to synthesize the damage pattern, based on the information gathered by SLAM and C-SAM. The shadowed regions were reconstructed and total delamination area was quantitatively measured. Because the measurement is nondestructive, the quantitative results can be used to correlate with compression-after-impact (CAI) strength of the impacted specimens.

FUNDAMENTALS OF ACOUSTIC MICROSCOPY METHODS

As a general comparison between the methods, the SLAM is primarily a transmission mode instrument that creates true real-time images of a sample throughout its entire thickness. In operation, ultrasound is introduced to the bottom surface of the sample by a piezoelectric transducer and the transmitted wave is detected on the top side by a rapidly scanning laser beam. C-SAM is primarily reflection mode instrument that uses a transducer with an acoustic lens to focus the wave at or below the sample surface. The transducer is mechanically translated (scanned) across the sample in a raster fashion to create the image. C-SAM employs a pulse-echo transducer and the specific depth of view can be electronically gated. C-SAM can image several millimeters or more into most samples and is ideal for analyzing at a specific depth.

QUANTITATIVE MEASUREMENT OF IMPACT DAMAGE

The damage in Graphite/Epoxy composite laminates resulting from transverse low-velocity impact was studied. Interlaminar delaminations were the primary concern of the study. A spherical-nosed impactor with 0.16 Kg mass was used to create impact damage in the test specimens. The radius of the spherical nose head made of steel was 0.635 cm. The specimens were firmly clamped along two parallel edges. T300/976 composites with ply orientation $[0_3/90_3/0_3/90_3/0_3]$ were selected for the study. The dimensions of each specimen were 10 cm long and 6.6 cm wide. Each specimen was impacted at a selected impact velocity. Specimens were then inspected by SLAM, C-SAM and X-ray, respectively.

Fig. 1 A 10 MHz SLAM image projecting all delaminations in a T300/976 composite with a ply orientation $[0_3/90_3/0_3/90_3/0_3]$. The damage was caused by a 0.16 Kg impactor at a speed of 6.7 m/s. The field of view is 45 mm x 26 mm.

A 10 MHz SLAM image is shown in Figure 1, projecting all laminated interfaces in the impacted specimen. The damage was caused by an impact velocity of 6.70 m/s. The field of view of the SLAM image is 45 mm by 26 mm, in which black region shows delaminations, while white region indicates free of damage. The damage pattern shown in SLAM image is a projection view of delaminations occurred at all laminated interfaces throughout the entire sample thickness. SLAM images were produced at a video rate, or 1/30 second.

The same specimen was also inspected by a 10 MHz C-SAM system, with a transducer having a 0.25" element and 0.5" focal length. The scan size is 52.0 mm by 48.8 mm. During inspection the transducer was physically lowered in order to focus the ultrasound beam at a specified depth (or interface). An electronic gate was activated at corresponding time to extract the return echoes at the specific level. The delaminations as a result of low velocity impact were expected to take place at the interfaces where the fiber orientation of the top layer was different from that of the bottom layer. Four C-SAM images are shown in Figure 2, displaying delamination patterns at the first, second, third and forth interface, respectively.

In these C-SAM images, the gray color bar on the left of each image represents amplitudes of return echoes. The white at the center of the bar represents low reflection at the interface which usually indicates a good bonding condition. The gray colors, varying from white toward dark, represent increasing amplitudes. The delamination areas are displayed in dark colors. It is clear that each delamination oriented itself along the fiber direction of the bottom ply of the laminated interface. Please note that part of the delamination pattern was shadowed by prior laminated layers.

The overlapped part of delamination shown in C-SAM images for each laminated interface could be synthesized from the computed shapes by an analytical model described in literature [10]. The results are shown in Figure 3. As a result, the delamination area at each interface is calculated to be, 43, 172, 184 and 326 mm^2, respectively, and the total delamination area is summed up to be 725 mm^2, which is tabulated in Table 1.

To verify the accuracy of the results, the same specimen was X-rayed using enhanced dye-penetrant. A small hole was drilled at the impacted location and dye-penetrant was applied through the hole. The X-Radiograph is shown in Figure 4. The delamination areas for each delaminated interface on X-radiograph are calculated to be 35, 171, 180 and 338 mm^2, which results in a total delamination of 724 mm^2. It agrees very well with the results from C-SAM images.
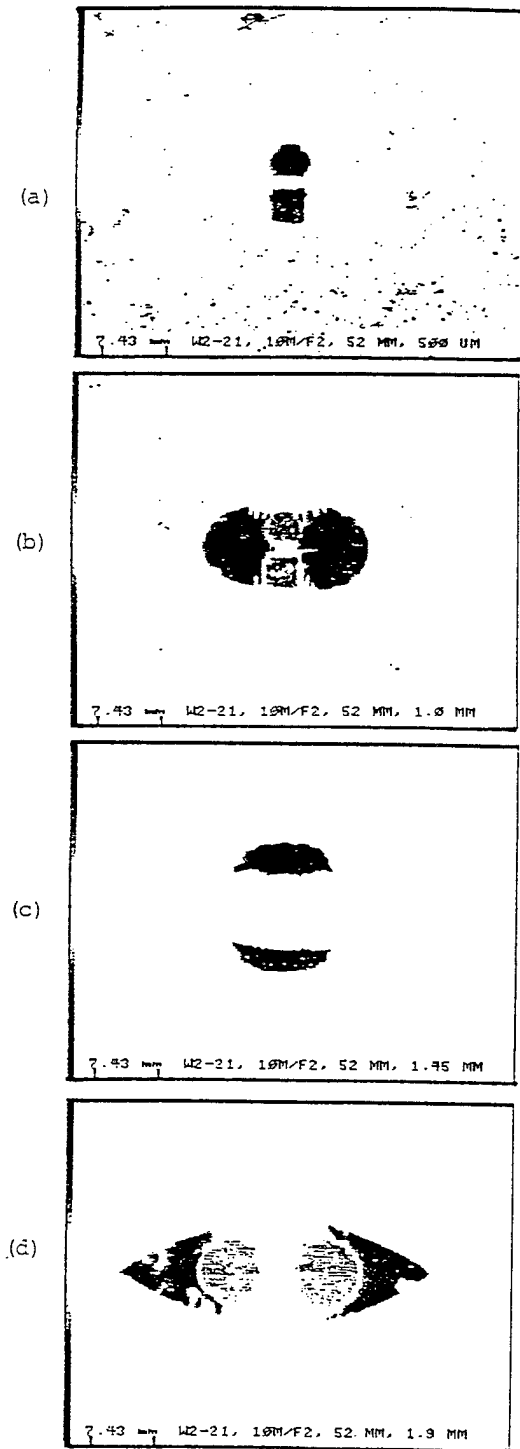
Fig. 2 Four 10 MHz C-SAM images which show the delaminations for each laminated interface at (a) at 0.45 mm, (b) 0.9 mm, (c) 1.35 mm, and (d) 1.8 mm below the top surface. The scan size is 50 mm x 48.8 mm.
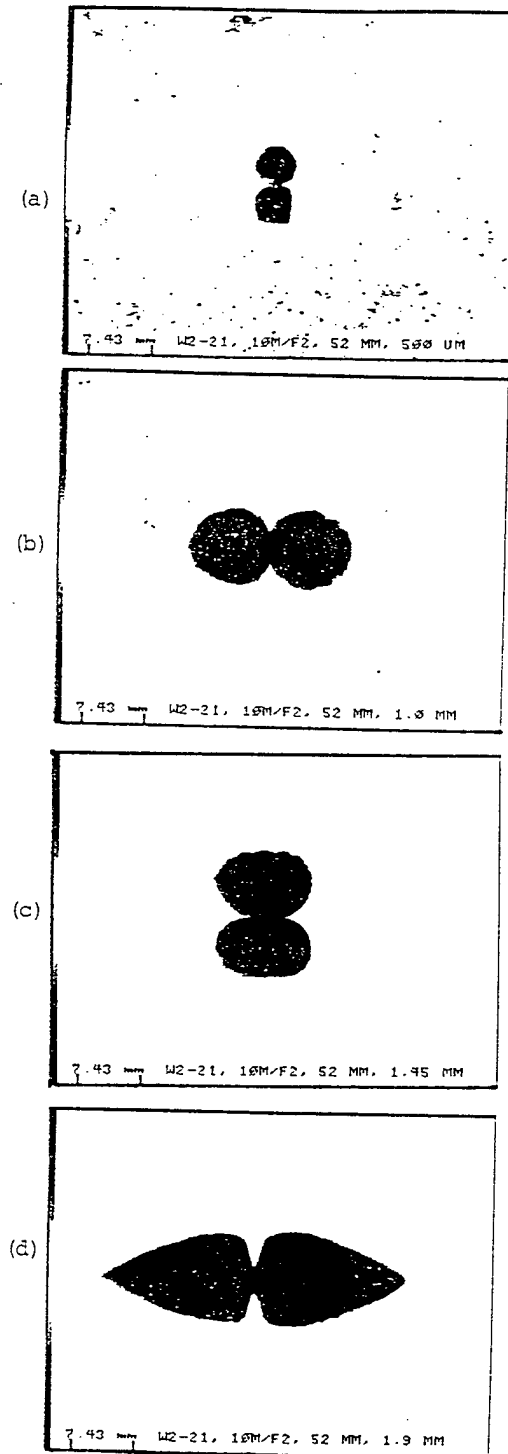
Fig. 3 Reconstructed delamination areas at corresponding interfaces as shown in Fig. 2. Delamination areas were measured to be 43, 72, 184 and 326 mm^2, respectively.
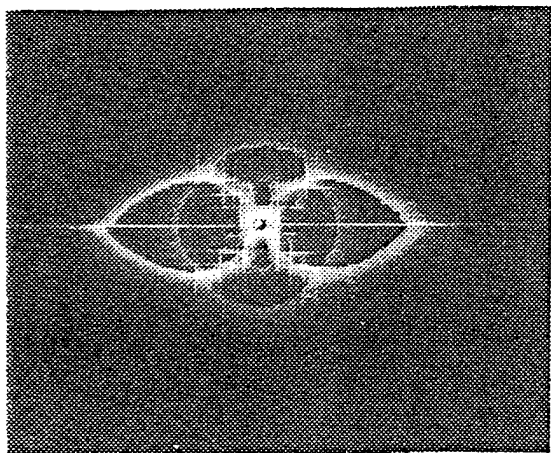
Fig. 4 X-Radiograph of the same impacted composite specimen whose SLAM image was shown in Fig. 1.

TABLE 1 Comparison of measured delamination areas from C-SAM and X-Radiograph.

Method Delamination	C-SAM (mm^2)	(%)	X-Radiograph (mm^2)	(%)
1st Interface	43	5.9	35	4.8
2nd Interface	72	23.7	171	23.5
3rd Interface	184	25.4	182	25.1
4th Interface	326	45.0	338	46.6
total	725	100.0	726	100.0

TABLE 2 Quantitative area measurements of delaminations for Specimens B3 and B4.

Specimen ID Interface	B3 (cm^2)	B4 (cm^2)	B4/B3 ratio
1st	0.68	0.61	0.90
2nd	2.15	2.89	1.35
3rd	2.70	4.21	1.56
4th	4.83	7.51	1.55
Total Delam.	10.36	15.22	1.47
Impact Energy	8.36	13.25	1.58

STUDY OF DELAMINATION VS. IMPACT VELOCITY

Four glass/epoxy composite specimens were fabricated with different lay-ups to study the effect of ply orientations on impact damage. They were Specimens B3 & B4 with a ply orientation $[0_3/90_3/0_3/90_3/0_3]_{15}$ and Specimen C3 & C4 with a ply orientation $[0_2/90_2/0_2/90_2/0_2/90_2/0_2]_{14}$. The measured delamination areas at each laminated interface are tabulated in Table 2 for Specimens B3 and B4 and in Table 3 for Specimens C3 and C4, respectively. As being expected, delaminations took place at the interfaces locating at below the 3rd, 6th, 9th and 12th ply, respectively where the fiber orientation differs. In the case of Specimens C3 and C4, delaminations occurred at interfaces below the 2nd, 4th, 6th, 8th, 10th, and 12th ply.

It is found that total delamination area is increasing proportionally to the increase of impact energy, despite of fiber orientation. The total delamination area in B4 increases by 1.47 times when the total impact energy increases by 1.58 times, compared to the case of B3. In the case of C3 and C4, the total delaminations increases by 1.53 when the energy increases by 1.54. Reviewing the data one can find that most of the increase in delamination area comes from the last two interfaces, the 3rd and 4th in B3 and B4 and the 5th and 6th in C3 and C4.

TABLE 3 Quantitative area measurements of delaminations for Specimens C3 and C4.

Specimen ID Interface	C3 (cm^2)	C4 (cm^2)	C4/C3 ratio
1st	0.16	0.20	1.26
2nd	1.38	1.77	1.28
3rd	1.39	1.92	1.39
4th	1.45	1.87	1.29
5th	1.77	2.89	1.64
6th	2.95	5.29	1.79
Total Delam.	9.10	13.94	1.53
Impact Energy	8.81	13.58	1.54

To investigate the effect of fiber orientation on delaminations, one can compare the quantitative data of Specimen B4 to that of C4. Remember that Specimen B4 has four laminated interfaces in $[0_3/90_3/0_3/90_3/0_3]_{15}$, while C4 has six in a $[0_2/90_2/0_2/90_2/0_2/90_2/0_2]_{14}$ lay-up. The delaminations occurred at a depth of 3, 6, 9 and 12 ply thickness in Specimen B4 and at a depth of 2, 4, 6, 8, 10, and 12 ply thickness in Specimen C4. Both specimens were impacted with a nearly same energy. The Specimen B4 was impacted with an energy 13.25 ft-lb. The impact energy for Specimen C4 was 13.58 ft-lb. However, total delamination area in C4 is less than that in B4. The total delamination area in C4 is 13.94 cm^2, compared to 15.22 cm^2 in B4. Of course, we have to bear in mind that B4 is thicker than C4 by one layer. B4 has 15 layers in total and C4 has 14 layers. This may account for the decrease in delamination area as a result of decreasing thickness.

SUMMARY

Several composite laminates having different ply orientations were selected for impact study. The impact damage was caused by a 0.16 Kg impactor at various velocities. Specimens were then inspected by SLAM, C-SAM and X-ray. SLAM provides an instant view of the projection of all delaminations, while C-SAM delineates the delamination profile layer by layer at each laminated interface. The sizes and shapes of the delaminations shown on SLAM and C-SAM images agreed with those detected by X-radiograph method. The overlapped regions of impact damage pattern on acoustic images were synthesized by analytical computation, and the total delamination areas were quantitatively measured for various impact conditions. The results confirmed a linear relationship of total delamination area to impact energy, for given ply orientation. The quantitative data can then be used to correlate with compression-after-impact strength of the impacted specimens.

ACKNOWLEDGMENTS

REFERENCES

[1] F. K. Chang and Z. Kutlu, "Collapse Analysis of Composite Panels with Multiple Delaminations," Proceedings of the AIAA/ASME/SAE 30th Conference, Mobile, AL, (1989), pp. 989-1011.

[2] D. H. Allen, C. E. Harris, S. E. Groves, and R. G. Norvell, "Characterization of Stiffness Loss in Crossply Laminates," J. of Material Science, Vol. 22, (1988), pp. 71-80.

[3] S. S. Wang, "An Analysis of Delamination in Angle-ply Fiber Reinforced Composites," J. of Applied Mechanics, Vol. 17, (1980), pp. 64-70.

[4] H. T. Wu and G. S. Springer, "Impact Induced Stresses, Strains and Delaminations in Composite Plates," J. of Composite Materials, Vol. 22, (1988), pp. 533-560.

[5] G. Clark, "Modeling of Impact Damage in Composite Laminate," Composites, Vol. 20, (1988), pp. 209-214.

[6] H. Aggour and C. T. Sun, "Finite Element Analysis of a Laminated Composite Plate Subjected to Circularly Distributed Central Impact Loading," J. of Computers and Structures, V. 28, (1988), pp. 729-736.

[7] D. Liu, L. S. Lillycrop, L. E. Malvern and C. T. Sun, "The Evaluation of Delamination - An Edge Replication Study," Experimental Techniques, Vol. 11 (5), (1987), pp. 20-25.

[8] A. Korpel, L. W. Kessler, and P. R. Palermo, "Acoustic Microscope at 100 MHz", Nature, Vol. 232, No. 5306, pp. 110-111. (1970)

[9] R. A. Lemons, and C. F. Quate, "Acoustic Microscope - Scanning Version", Appl. Phys. Letters, Vol 24, No. 4, pp. 163-165 (1974).

[10] F. K. Chang and K. Y. Chang, "A Progress Damage Model for Laminated Composites Containing Stress Concentrations," J. of Composite Materials, Vol. 21, (1987), pp. 834-855.